THE TIDAL DISRUPTION OF STARS BY A MASSIVE BLACK HOLE AT THE CENTER OF A GALAXY

by

Michael Scott Fulbright

A Dissertation Submitted to the Faculty of the

DEPARTMENT OF ASTRONOMY

In Partial Fulfillment of the Requirements
For the Degree of

DOCTOR OF PHILOSOPHY

In the Graduate College

THE UNIVERSITY OF ARIZONA

1 9 9 5

REPLACE THIS PAGE WITHFINAL EXAMINING COMMITTEE APPROVAL FORM

STATEMENT BY AUTHOR

This dissertation has been submitted in partial fulfillment of requirements for an advanced degree at The University of Arizona and is deposited in the University Library to be made available to borrowers under rules of the Library.

Brief quotations from this dissertation are allowable without special permission, provided that accurate acknowledgment of source is made. Requests for permission for extended quotation from or reproduction of this manuscript in whole or in part may be granted by the head of the major department or the Dean of the Graduate College when in his or her judgment the proposed use of the material is in the interests of scholarship. In all other instances, however, permission must be obtained from the author.

SIGNED: _____

ACKNOWLEDGMENTS

The end which sometimes never seemed to be soon enough is now all too close. Six years of all kinds of experiences. Early during my time here at Steward, a number of students helped make Tucson seem like a new home. In particular, Hans, Scott, Dante, and the group who played soccer and basketball were wonderful to spend time with. I remember many enjoyable hikes with Bob and Sylvanie, as well as Doug, who went on several death hikes with me. More lately, the "DOOM/DOME crew" has made life interesting. Craig, Tim, and Eric have tolerated my afternoon appearances in which we talk about DOOM and computers. Oh, and that Babylon 5 show. And finally, spending two summers with Chris in Los Alamos was very rewarding.

By far the most important influences on me professionally have been my advisors. Stephen Reynolds, my undergraduate advisor, was instrumental in my decision to pursue graduate work in astronomy. My opportunity to work with Steve on real research was very rewarding. My second–year project advisor, Jim Liebert, gave me the best support any one could expect, and without him I don't know if I could have gotten past my prelim. Then when Willy Benz arrived, I knew he was someone I wanted to work with. Like Jim, he has supported me beyond reasonable expectations, and has proved invaluable during the period over which I produced the work you now hold. Additionally, I would like to thank Joe Shields for his input regarding my dissertation, which really helped the work come together coherently. Likewise I thank Adam Burrows for reading and commenting on my disseration, as well as for sharing his own ideas about the world as a whole. And especially for caring enough to disagree with me!

But none of this could have happened without my parents, who have always tried to provide for my needs. My father introduced me to science and technology at an early age. He opened up limitless worlds to me by providing me with a computer while I was in junior high. His giving my brother Jon and I binoculars one Christmas led to both of us in graduate school studying astronomy. My mother I thank for working so hard to make the lives of myself and my siblings as normal as possible after a divorce. More recently she has helped me understand myself in many ways. I look forward to spending more time with both of them soon.

Lastly, I have the most heartfelt thanks to my wife Lysa. I don't think she fully realized what being married to a graduate student would be like. Throughout she has been both understanding and supportive. And thanks for teaching me how to use commas! Between her and our two brats, I mean cats, Bahktar and Leroy, I am surrounded by strong feelings of family and love. Thanks to them, I've never been happier in my life.

DEDICATION

To Lysa

Table of Contents

LIST OF ILLUSTRATIONS 8

LIST OF TABLES 10

ABSTRACT 11

1 INTRODUCTION **12**

2 A METHOD OF SMOOTHED PARTICLE HYDRODYNAMICS USING SPHEROIDAL KERNELS **16**

2.1 Implementing Spheroidal Kernels 21

2.1.1 Introduction 21

2.1.2 Calculating the Value of the Kernel and its Derivative 23

2.1.3 Evaluating Particle Forces 24

2.1.4 Time Evolution of the Tensor H 26

2.2 Benchmarking Spheroidal and Spherical Kernels 28

2.2.1 Homologous Collapse of a Zero–Temperature Cloud in 1D . . 29

2.2.2 Tidal Disruption of a Star by a Massive Black Hole 35

2.3 Conclusions 43

3 SMOOTHED PARTICLE HYDRODYNAMICS SIMULATIONS OF THE DISRUPTION PROCESS **44**

3.1 Numerical Method 48

3.2 General Notes Concerning the Simulations 52

3.3 Results for $n = 3/2$ 57

3.3.1 Stripped Material 58
3.3.2 The Pancake Phase 65
3.3.3 Tidal Energy Transfer 74
3.4 Results for $n = 3$ 77
3.5 Conclusions 82

4 THE TIDAL DISRUPTION OF STARS IN GALACTIC NUCLEI 84
4.1 Tidal Disruption of Stars in a Truncated Isothermal Sphere 88
4.1.1 The Stellar Cluster Model 88
4.1.2 Loss–Cone Theory 91
4.1.3 Including the Hydrodynamic Details of Tidal Disruption . . . 95
4.2 Overall Role of Tidally–Disrupted Stars as a Fuel Source 102
4.3 Observational Consequences of a Tidal Disruption Event 105
4.4 Current Observational Evidence for Tidally–Disrupted Stars 109
4.4.1 The X–ray Outburst of IC 3599 109
4.4.2 Balmer Line Variability in NGC 1097 115
4.5 Conclusions 117

5 CONCLUSIONS AND FUTURE WORK 120

REFERENCES 125

List of Illustrations

2.1 Central density of a homologously collapsing cold cloud versus time . 31

2.2 Innermost row of particles at $t = 0.3$, spherical run 33

2.3 All particles at $t = 0.3$ in the plane $y = 0$, spherical run 33

2.4 All particles at $t = 0.3$ in the plane $y = 0$, spheroidal run 34

2.5 Central density as a function of time for a $\beta = 5$ encounter 38

2.6 Z velocity profile vs. z along the z–axis at the time of closest approach 39

2.7 Projection of particle positions onto the x–y plane 41

2.8 Projection of particle positions onto the x–z plane 41

2.9 Density profile vs. z along the z–axis 42

3.1 A graphical interpretation of the spheroidal smoothing tensor H . . . 50

3.2 The stripped mass fractions for an $n = 3/2$ polytrope 59

3.3 Density of the star in the orbital plane for several $n = 3/2$ encounters 60

3.4 Energy and period distribution of debris for several $M_{bh} = 10^6$ $M_\odot$ encounters 62

3.5 Energy and period distributions of debris for several $M_{bh} = 10^4$ $M_\odot$ encounters 63

3.6 Time series showing the collapse of a star for a $\beta = 5$ encounter . . . 67

3.7 Central density enhancement as a function of β for $n = 3/2$ 70

3.8 Entropy distribution in the collapsing stellar atmosphere for $\beta = 5$ . . 71

3.9 Density distribution in the collapsing stellar atmosphere for $\beta = 5$ . . 72

3.10 Ram pressure distribution in the collapsing stellar atmosphere for $\beta = 5$ 73

3.11 Like Figure 3.8, except using 14591 particles 74
3.12 Like Figure 3.9, except using 14591 particles 75
3.13 Energy transfer to the star for $n = 3/2$ models 76
3.14 Density profiles of the $n = 3/2$ and $n = 3$ models 78
3.15 Cumulative mass profiles of the $n = 3/2$ and $n = 3$ models 78
3.16 The stripped mass fractions for both the $n = 3/2$ and $n = 3$ polytropes 80
3.17 Energy and period distribution of debris for a $\beta = 3$, $n = 3$ encounter 81

4.1 Stripped mass function $S(b)$ for an $n = 3/2$ polytrope 96
4.2 Total mass inside of a given radius r 98
4.3 Density profile $\rho(r)$ 98
4.4 Differential mass stripping rate $\zeta(b)$. 100
4.5 Cumulative mass stripping rate 101
4.6 Proposed scenario for the IC 3599 outburst 113

List of Tables

3.1 Units used in these calculations 54

3.2 Mass fractions for $n = 3/2$ and $M_{bh} = 10^6$ $M_\odot$ as a function of β . . . 58

3.3 Mass fractions for $n = 3/2$ and $M_{bh} = 10^4$ $M_\odot$ as a function of β . . . 61

3.4 Magnitude of density enhancement for $n = 3/2$ calculations 69

3.5 Mass fractions for $n = 3$ and $M_{bh} = 10^6$ $M_\odot$ as a function of β 79

ABSTRACT

Studies of the luminosity evolution of optical Quasi–Stellar Objects (QSOs) suggest that a large number of normal–looking galaxies today have a central massive black hole. These galaxies once contained Active Galactic Nuclei (AGN), but a dwindling fuel supply forced the central engine to fade. If one of these galaxies happens to be close enough, it might be possible to detect the central black hole by the effects it has on the kinematics and surface density of stars in the galactic nucleus. But, for the majority of galaxies, it is not feasible to observe these effects due to their great distance.

Not feasible, that is, until the black hole disrupts a passing star. The debris of the star will form an accretion disk around the black hole. The galactic nucleus will then become a reborn AGN. It is then possible to detect the black hole by the sudden appearance of a compact source of extreme UV and X–ray photons at the center of a galaxy. Broad, double–peaked emission lines may also appear, giving conclusive evidence that an accretion disk has formed around a massive black hole. A survey to detect flares from galactic nuclei resulting from tidally–disrupted stars could possibly answer whether or not most galaxies go through an AGN phase.

In this work, we will use Smoothed Particle Hydrodynamics (SPH) simulations to remove much of the uncertainty that existed in previous work on the tidal disruption of stars. These works were forced to assume that stars which passed inside the Roche limit of a black hole were completely accreted by the black hole. We will replace this assumption with the results of our SPH simulations, and find that previous works overestimated the rate at which gas is stripped from stars by a factor of two. We will then review the observational consequences of a disruption event, and consider two cases in which such an event may have been witnessed.

Chapter 1

INTRODUCTION

Within the inner parsecs of an Active Galactic Nucleus (AGN), power comparable to that radiated by the entire host galaxy is released. An exotic process is required in the central region of an AGN that is capable of such efficient conversion of mass to energy. The leading candidate for this process is an accretion disk around a massive black hole. It is expected that $\sim 10\%$ of the rest mass energy of accreted material will be radiated. At this efficiency, about 1 $M_\odot$ of material must be accreted per year to achieve a total luminosity of 10^{45} ergs/s. The tidal disruption of stars by the massive black hole at the center of the AGN was proposed by Hills (1975) as a source of the required material. Subsequent research found that although tidal debris is a source for fuel, such debris cannot provide material at the rate required for the more luminous AGNs. For these objects, the central density is so great that stars are more likely to be destroyed by colliding with other stars than to be disrupted by the black hole. It appeared that tidal disruption was only of importance in the less massive of Seyfert galaxies, and work on this subject was minimal after the early 1980s.

In the later 1980s, detailed studies of the optical luminosity evolution of AGN (e.g., Boyle *et al.* 1987) confirmed the already held belief that although the space density of AGN in the past was comparable to that in the present day, the luminosity function had evolved with time. One way to explain the differences between the past and present luminosity function is to assume that AGNs become fainter with time. In this model, all AGN were formed before a redshift of $z = 2.2$ and have lived on into the present in the form of Seyferts. Due to the long lifetime of these AGN, the central black hole is able to grow to a present day mass of order 10^9 $M_\odot$ or greater. With a black hole mass this large, the tidal disruption of stars does not contribute mass to be accreted by the black hole, as the radius at which stars are disrupted is actually *inside* the event horizon of the black hole. Stars simply fall into the black hole without disrupting. Again stellar collisions appear to be the dominant source of the material which is accreted by the central black hole. A problem with this scenario, however, is that modern AGN do not to appear, on average, to have the large black hole mass (10^9 $M_\odot$) predicted.

However, there is an alternative interpretation of the results of Boyle *et al.* Instead of a single population of long–lived AGN, it is possible to explain the observations by hypothesizing generation after generation of short–lived AGN, with the characteristic luminosity decreasing in later generations. The AGN seen today are just the latest generation of this progression. The proposed lifetime of a given AGN is $\sim 10^7$ years, during which time the central black hole grows to a mass $\sim 10^7$ $M_\odot$. A consequence of this model is that many galaxies today should have a massive central black hole. Since the majority of these galaxies are not observed to have an active nucleus, detecting the presence of the central black hole would appear to be a problem. A solution to this problem was suggested by Rees (1988). He noted that an inactive AGN will become active when the central

black hole disrupts a star and accretes the debris. He estimated that the accretion time scale for the debris was of order years, while the interval between disruption events ranges from 10^2–10^4 years, depending on the mass of the black hole and the density and velocity dispersion of the stellar nucleus. This means that these "dead quasars" spend less than 1% of the time in an active state. But this also means it is possible to detect the massive black holes around us by searching for galactic nuclei which suddenly become active. If black holes could be detected this way in many galaxies, it would lend considerable support to the short–lived AGN hypothesis.

Rees was able to give a rough idea of what a reborn AGN would look like. But uncertainties about the physics of the disruption of the star and the accretion of the resulting debris needed to be addressed. For example, in the majority of previous work on the tidal disruption of stars, it was assumed that the star was disrupted if it passed within a threshold distance from the black hole. All of the debris would then be accreted by the black hole. This assumption, which we will call the hard–sphere assumption, was a simplification that was necessary at the time because it was not yet possible to numerically simulate the disruption of a star. Now, with modern high–speed computers and a numerical technique known as Smoothed Particle Hydrodynamics (SPH), it is possible to model the disruption process in sufficient detail. The particular SPH method which we will employ is described in Chapter 2. The disruption of a star is an extremely dynamic event, and our SPH method uses several original modifications in order to handle the extreme conditions which arise. With the results from our SPH simulations we will then replace the hard–sphere assumption with numerically derived cross sections, which will be presented in Chapter 3. This achievement will remove one degree of uncertainty which existed in previous work on the tidal disruption of stars.

We will then proceed in Chapter 4 to re–examine the problem of the disruption of stars in a stellar cluster surrounding a massive black hole, with an emphasis on the impact of using our numerical results in place of the hard–sphere assumption used previously. Briefly, we find that previous work overestimated the rate at which gas is stripped from stars by a factor of two.

Next we consider some of the observable consequences of a tidally disrupted star. The actual disruption of the star is unlikely to be observed, as the duration of this event is only hours, and in the majority of cases the star will be quickly pulled apart and cool. So one must wait until the debris is accreted by the black hole in order to tell that a star has been disrupted. Using the results from our SPH calculations, it is possible to estimate the time scale for the debris to be accreted. We find our results confirm earlier estimates by other workers in that there will be a flare which lasts for approximately one year after the star is disrupted.

We next review two papers that both claim to have observed an outburst from a galactic nucleus which was triggered by the tidal disruption of a star. Finally, in Chapter 5, we review the major findings of this work and comment on what future work could be done to improve our understanding of the role of the tidal disruption of stars in the formation and evolution of active galactic nuclei.

Chapter 2

A METHOD OF SMOOTHED PARTICLE HYDRODYNAMICS USING SPHEROIDAL KERNELS

The development of smoothed particle hydrodynamics (SPH) in the late 70's (Lucy 1977; Gingold & Monaghan 1977) was in response to the need for a numerical method which could efficiently model three–dimensional systems which lack symmetry and possess large voids. Traditional finite–difference techniques require a grid to encompass the system under study. In three dimensions, the number of grid elements can quickly make a problem intractable, so symmetry arguments are necessary to reduce the problem to a two dimensional calculation. In addition, memory is wasted on grid elements representing empty regions. SPH overcomes these problems by representing the fluid with a finite number of particles which

act as interpolating points for quantities such as density and internal energy. Each particle moves in response to particle–particle forces like gravity and gas pressure. As the particles move, so does the interpolation mesh. No memory is used to represent empty spaces, and since the interpolation mesh moves with the fluid, SPH is able to effectively model systems which deform from a simple symmetry. With the advent of efficient neighbor–finding schemes, SPH simulations routinely use 10^4–10^5 particles on desktop workstations. For a recent review of SPH, consult Monaghan (1992) and the references therein.

All SPH codes employ a smoothing kernel in order to interpolate physical quantities using the particles as the interpolating points. In almost all previous codes, the smoothing kernel was a spherically symmetric function W. One requires that W can be normalized and that it is of finite extent. The smoothing length h serves as a measure of the extent over which W is nonzero. The density at a point in space, for example, can then be defined as

$$\rho(\vec{r}) = \sum_{j=1}^{N} m_j W(\vec{r} - \vec{r_j}, h_j) \ , \tag{2.1}$$

where N is the total number of particles. This expression, however, is useless computationally because the majority of the particles will not contribute to the sum, as W is zero for distances greater than a few times h. By using neighbor–finding routines the number of particles included in the above sum is reduced to just the contributing particles. Common practice is to initially position the particles on a regular lattice. The smoothing length h of each particle is then set as to enclose the desired number of neighbors, typically 40–80. This number of neighbors is necessary to insure the accuracy of the interpolation, and results in h being approximately equal to the spacing of the particles in the grid.

Now consider the following example – a constant density, self-gravitating

spherical cloud of gas which begins to contract. Let the initial radius of the cloud be R and let all particles have an initial smoothing length of h_0. As the cloud contracts, the particles are brought closer together, increasing the number of neighbors for each particle and slowing the simulation down. And at some point, the size of the cloud will begin to approach h_0, meaning there is effectively one resolution element across the entire cloud! In order to address this problem, almost all SPH codes dynamically adjust the size of the kernel in order to maintain a constant number of neighbors. This has the benefits of improving spatial resolution as well as speeding up the simulation.

Now imagine that instead of collapsing in a spherically–symmetric manner, the gas cloud collapses along a preferential axis, perhaps due to net angular momentum. Eventually the sphere will deform into a flattened disk shape. In order to maintain a constant number of neighbors, the kernel will have to shrink to a fraction of the height of the disk. If the disk is sufficiently flattened, however, this may result in a kernel that is not large enough to extend to any other particles within the plane of the disk, meaning there is no pressure force between these particles. The only pressure forces will be along the axis on collapse, which is clearly wrong. To address this problem, one could constrain the kernel to always be large enough to include these lateral particles. Consequently, however, the smoothing length would become comparable to the thickness of the disk, and spatial resolution would be sacrificed. Therefore, with a kernel that can only deform in a spherically–symmetric manner, it is impossible to model the evolution of the system once it reaches the disk state.

In order to quantitatively demonstrate the point raised above, consider the following example. Let a zero–temperature, constant–density cloud collapse along

the z–axis with a homologous velocity profile given by

$$\begin{aligned} v_z(z,t) &= -v_0\left(\frac{z}{z_m(t)}\right) , \\ z_m(t) &= z_0 - v_0 t \ . \end{aligned} \tag{2.2}$$

Here, z_0 is the initial height of the cloud, and $z_m(t)$ is the maximum extent of the cloud in the z–direction as a function of time. Let the initial separation of the particles be h_0, which will also be the initial smoothing length for each particle. In addition, give each particle a mass of m. We now want to determine how to change h in order to maintain a constant number of neighbors N_{neigh} for each particle. A crude measure of the density at a given particle can be written

$$\rho \simeq \frac{mN_{neigh}}{h^3} \ . \tag{2.3}$$

In order to keep N_{neigh} constant we require that $h \propto \rho^{-1/3}$. For a given particle we can then write

$$h(t) = h_0 \left(\frac{\rho_0}{\rho(t)}\right)^{1/3} , \tag{2.4}$$

where h_0 and ρ_0 are the initial smoothing length and density of the particle. Taking the time derivative of this expression and applying some algebra gives

$$\frac{dh(t)}{dt} = \frac{-h(t)}{3}\left(\frac{1}{\rho(t)}\frac{d\rho(t)}{dt}\right) \ . \tag{2.5}$$

By the use of the continuity equation, we end up with the following expression for the time evolution of h

$$\frac{dh(t)}{dt} = \frac{h(t)}{3}\nabla \cdot \vec{v} \ . \tag{2.6}$$

In the example under consideration, the only particle motion is along the z–axis (since the cloud is zero temperature), and equation (2.6) reduces to

$$\frac{dh(t)}{dt} = h(t)\left(\frac{1}{3}\right)\left(\frac{\partial v_z(z,t)}{\partial z}\right) ,$$

$$= \quad h(t)\left(\frac{-v_0}{z_0 - v_0 t}\right) \ . \tag{2.7}$$

Integrating this equation gives the time evolution of h

$$\frac{h(t)}{h_0} = \left[\frac{z_m(t)}{z_0}\right]^{1/3} \ . \tag{2.8}$$

Because we require the smoothing kernel W to be of finite extent, it will have a value of zero for distances greater than αh, where α is typically two. When the cloud has shrunk by a factor of α^3 in the z–direction (i.e., $(z_m(t)/z_0) = \alpha^3$), one finds $h = h_0/\alpha$. Since the particles are not moving in the x–y plane, the separation of the particles in the x–y plane will be h_0. Therefore, the particles are no longer in contact in the x–y plane. Adding particles will not help the situation, since the right hand side of equation (2.8) does not depend on h_0. For the typical value of $\alpha = 2$, the greatest density ratio which can be modeled is a factor of eight. This means that one can still model adiabatic shocks, where the maximum density enhancement is given by

$$\frac{\rho}{\rho_0} = \frac{\gamma + 1}{\gamma - 1} \ , \tag{2.9}$$

where γ is the ratio of specific heats. Typical values for γ are 5/3 and 4/3, leading to a maximum density enhancement of 4 and 7, respectively. In summary, a code using spherical kernels encounters severe problems when attempting to model a system that becomes substantially compressed in one direction.

To address this problem, we have developed an SPH code which allows the initially spherical kernels to deform into a spheroid shape. In the above example, the size of the kernel in the direction of collapse would evolve independently of the size of the kernel parallel to the x–y plane. This allows the relative spatial resolution in the z–direction to be maintained without particles losing lateral contact, as in the case of spherical kernels. Our method is directly applicable to a

number of astrophysical problems involving nonspherically symmetric events, such as head–on stellar collisions or tidal disruptions.

2.1 Implementing Spheroidal Kernels

2.1.1 Introduction

The method described in this paper is a special case of a more general method of SPH we are developing. In this more general case, the smoothing kernel is a triaxial ellipsoid which can be oriented arbitrarily in three space. The information describing this kernel can be conveniently contained within a second–order, real, symmetric tensor H

$$H = \begin{pmatrix} h_{xx} & h_{xy} & h_{xz} \\ h_{xy} & h_{yy} & h_{yz} \\ h_{xz} & h_{yz} & h_{zz} \end{pmatrix} . \tag{2.10}$$

The eigenvectors of this tensor are the directions of the three axes of the ellipsoid, and the corresponding eigenvalues are the extent of the ellipsoid along each axis. To use this smoothing kernel in a simulation, one would initially set the tensor H of each particle according to the geometry of the problem. If spherical kernels were desired initially, then one would set $h_{xx} = h_{yy} = h_{zz} = h_0$, where h_0 is the initial smoothing length, and $h_{xy} = h_{xz} = h_{yz} = 0$. However, with ellipsoidal kernels, one has more freedom in setting up the initial conditions than one has with spherical kernels. If the initial configuration was a disk, then one could pack ellipsoids together instead of spheres, reducing the number of particles necessary to achieve a given spatial resolution across the thickness of the disk. During the simulation, one would modify H for a given particle according to the local flow of neighboring

particles in order to maintain a relatively constant number of neighbors. Given the number of degrees of freedom for the smoothing kernel, a code using ellipsoidal kernels would provide excellent spatial resolution even if the system underwent extreme deformation. We are currently working on a version of the code which implements ellipsoidal kernels.

Meanwhile, we have found that a less complex version of the code is sufficient for the class of problems we are interested in. Because the tensor H is a real, symmetric tensor, there exists a reference frame in which it is a diagonal matrix. Let us choose the frame in which we will compute the problem to be the frame which diagonalizes H. Now let us assume that the frame which diagonalizes H remains constant throughout the simulation. This reduces the complexity of the problem because H is always a diagonal matrix. In addition, impose the constraint that $h_{xx} = h_{yy}$ at all times. The resulting shape of the kernel is a spheroid, and it is well suited for modeling systems that deform in predominately one direction. In the case of the tidal disruption of a star, for example, the star is modestly deformed in the orbital plane as it passes the black hole. Simultaneously, the star is savagely compressed in the direction perpendicular to the orbital plane, forming a thin disk. By choosing the x–y plane to be the orbital plane, we cause the major compression of the star to be along the z–axis. The spheroidal kernel can change its size along the z–axis (h_{zz}) independent of its size in the x–y plane (h_{xx}=h_{yy}). This allows one to maintain a constant number of neighbors while also ensuring contact with other particles in the plane of the disk, overcoming the problems inherent to spherical kernels.

2.1.2 Calculating the Value of the Kernel and its Derivative

The modifications required to an existing SPH code in order to implement spheroid kernels are minimal. The code must first be modified to take into account the fact that the kernel function and its derivative now depend on $\vec{r}$ and not just r. A spheroid is produced by rotating an ellipse about either its major or minor axis. Let this axis of rotation be along the z–axis. The extent of the spheroid along the x–, y–, and z–axes will be represented by h_{xx}, h_{yy}, and h_{zz}, respectively. In this case, the second–order tensor H introduced in the previous section has the form

$$H = \begin{pmatrix} h_{xx} & 0 & 0 \\ 0 & h_{yy} & 0 \\ 0 & 0 & h_{zz} \end{pmatrix} . \tag{2.11}$$

Due to the fact that we have constrained the kernel to be a spheroid, $h_{xx} = h_{yy}$ at all times, and also note that for the case of a spherical kernel, $h_{xx} = h_{yy} = h_{zz}$.

Define the smoothing kernel to be $W(\vec{r}, H)$. Furthermore, choose a function $W'(v)$ which satisfies the normal criteria for a spherical smoothing kernel, i.e., of finite extent and normalizable. We want to construct our smoothing kernel W so that surfaces of constant W lie on spheroids. This can be achieved by defining

$$v^2 = \left(\frac{x}{h_{xx}}\right)^2 + \left(\frac{y}{h_{yy}}\right)^2 + \left(\frac{z}{h_{zz}}\right)^2 , \tag{2.12}$$

$$W(\vec{r}, H) = \frac{W'(v)}{h_{xx} h_{yy} h_{zz}} . \tag{2.13}$$

It is assumed in equation (2.13) that W' has been properly normalized, so that

$$\frac{1}{h_{xx} h_{yy} h_{zz}} \int_0^\infty W'(v)\, v^2 dv = 1 . \tag{2.14}$$

To compute the gradient of W, we must compute its components along the x–, y–, and z–axes. For example, the component along the x–axis can be computed by

using the fact that

$$\frac{\partial W}{\partial x} = \frac{\partial W}{\partial v}\frac{\partial v}{\partial x} \ , \tag{2.15}$$

from which one obtains

$$\frac{\partial W}{\partial x} = \frac{x}{v\ {h_{xx}}^2}\frac{\partial W}{\partial v} = \frac{x}{v\ {h_{xx}}^2}\Big(\frac{1}{h_{xx}h_{yy}h_{zz}}\frac{\partial W'}{\partial v}\Big) \ . \tag{2.16}$$

Similarly one can obtain equations for $\frac{\partial W}{\partial y}$ and $\frac{\partial W}{\partial z}$.

2.1.3 Evaluating Particle Forces

In order for any SPH code to run efficiently, it must use a fast method of identifying the neighbors of a given particle. In a code which uses spherical kernels, the test to find a neighbor is to see if the distance between the two particles is less than the radial extent r_{cut} of the kernel. For spheroidal kernels, the situation is slightly more complicated. A first pass is made to find potential neighbors, using the largest of h_{xx} and h_{zz} to compute r_{cut}, where $r_{cut}(h) = \alpha h$, with α typically having a value of two. This value of r_{cut} is then supplied as the cutoff radius for the same neighbor–finding routine that was used in a spherical code. This produces a list of particles which must be further filtered to find the true neighbors. To do this, one computes the variables v_i and v_j for particles i and j using equation (2.12). If either $W(v_i)$ or $W(v_j)$ is nonzero, then the interaction between the two particles is calculated; otherwise, the pair is ignored.

In order conserve linear momentum locally, the forces computed between two particles must obey Newton's third law. To symmeterize the forces between particles, we use the following expressions when computing the interaction between two particles i and j (Hernquist & Katz 1989)

$$W_{ij} \ = \ \frac{1}{2}\left\{W_i(\vec{r}, H_i) + W_j(\vec{r}, H_j)\right\} \ , \tag{2.17}$$

$$\nabla W_{ij} = \frac{1}{2}\Big\{\nabla_i W_i(\vec{r}, H_i) + \nabla_j W_j(\vec{r}, H_j)\Big\} , \tag{2.18}$$

$$\vec{r} = \vec{r}_i - \vec{r}_j . \tag{2.19}$$

It should be noted that angular momentum is conserved when using spherical kernels. This is because the force on one particle due to the other is parallel to the vector joining the two particles, yielding a torque $\vec{T} \propto \vec{r} \times \vec{F} = 0$. In a code using spheroidal kernels this is not necessarily the case. If $h_{xx} \neq h_{zz}$, then from the expressions for $\frac{\partial W}{\partial x}$ and $\frac{\partial W}{\partial z}$ given by equation (2.16), one finds that the force between two particles is no longer parallel to the vector joining the two particles, leading to a net torque about the x– and y–axes. Since $h_{xx} = h_{yy}$, however, there will be no net torque about the z–axis.

Now consider a particle which is surrounded by a sea of copies of itself, with $h_{xx} \neq h_{zz}$. The torque on the particle is a vector quantity depending on the vector between the particle and its neighbor. If one sums over all neighbors, then the net torque will be zero. Can one expect the same to be true in a real computational problem, where the particle will be surrounded by particles which have different parameters than itself? As long as physical quantities do not vary excessively over a smoothing length in the x– or y–directions, then cancelation should occur to some degree. This requirement will be met in most situations, since the smoothing length of the kernel should be small compared to interesting physical scales in the problem. The particles near the boundary of the simulation will not be completely surrounded by neighbors, and the least cancelation will most likely occur for these particles. Whenever possible, one should arrange for the total angular momentum vector to be along the z–axis, since no component of the net torque between particles is along the z–axis. In many problems, the direction of predominant collapse is parallel to the axis of rotation, so it works out that spheroidal kernels

allow one to have improved spatial resolution along the direction of collapse and simultaneously conserve angular momentum exactly.

There is a further complication to consider when calculating the self–gravity of the gas particles. In the case of spherical kernels, the gravitational force is always along the vector between the centers of the two particles, leading to no net torque. With spheroidal kernels, the mass distribution *within the kernel* may no longer be spherically symmetric, leading to a net torque between the two particles. Fortunately, this torque should largely cancel out, for reasons discussed in the preceding paragraph. The best approach we have found for calculating the gravitational force between two overlapping particles is to use a gravitational softening parameter τ, as used in traditional N–body codes. In the case of the tidal disruption of a star by massive black hole, we also find that the total angular momentum for the system is conserved to better than 1%, so it is possible to produce quality results using this assumption. Nevertheless, one should closely monitor the total angular momentum vector in case this assumption is not warranted in a particular problem.

2.1.4 Time Evolution of the Tensor H

In a code using a spherical kernel, it is usually desirable to vary the smoothing length h for each particle in order to maintain a constant number of neighbors and to improve spatial resolution. When using spheroidal kernels, both h_{xx} and h_{zz} can be independently modified in order to preserve spatial resolution in two perpendicular directions. Remember that for spheroidal kernels, h_{xx}=h_{yy}. By using the strain–rate tensor S, one can measure the deformation of the positions of particles relative to a given particle. This is the information necessary to properly

deform the kernel to maintain spatial resolution and a relatively constant number of neighbors.

The definition of S is

$$s_{ij} = \frac{1}{2}\left(\frac{\partial v_i}{\partial x_j} + \frac{\partial v_j}{\partial x_i}\right) \ . \tag{2.20}$$

The diagonal elements of S are the magnitude of the relative change of the proximity of neighboring particles in the x–, y–, and z–directions. The off–diagonal elements supply information necessary to determine the actual directions of deformation, which may be along a direction other than the coordinate axes. We have assumed that the frame which diagonalizes H does not change during the simulation, so we set the off–diagonal terms of S to be zero. Writing S for particle i gives

$$S_i = \frac{1}{\rho_i}\begin{pmatrix} s_{xx,i} & 0 & 0 \\ 0 & s_{yy,i} & 0 \\ 0 & 0 & s_{zz,i} \end{pmatrix}, \tag{2.21}$$

where

$$s_{kk,i} = \sum_{j=1}^{N_{neigh}} m_j (v_{k,i} - v_{k,j})(\nabla W_{ij})_k \ . \tag{2.22}$$

The elements of S_i have the units of [time^{-1}], so multiplying S_i by a length gives the proper units for $\dot{H}_i$. In order to maintain a spheroidal shape for the kernel, we require that $h_{xx} = h_{yy}$, which can be accomplished by requiring $\dot{h}_{xx} = \dot{h}_{yy}$. The final expression for $\dot{H}_i$ is

$$\dot{H}_i = \frac{1}{\rho_i}\begin{pmatrix} s_{R,i} \times h_{xx,i} & 0 & 0 \\ 0 & s_{R,i} \times h_{yy,i} & 0 \\ 0 & 0 & s_{zz,i} \times h_{zz,i} \end{pmatrix} , \tag{2.23}$$

where

$$s_{R,i} = \frac{1}{2}(s_{xx,i} + s_{yy,i}) \ . \tag{2.24}$$

This gives three linear, first–order differential equations to solve to find H for the next time step, but the equations for h_{xx} and h_{yy} are identical. So, in practice, one integrates the equations for h_{xx} and h_{zz} and then sets $h_{yy} = h_{xx}$. Note that we have found it useful to set a lower limit for h_{zz} when an object undergoes extreme compression. This is because as h_{zz} shrinks, the typical time step also becomes smaller. By setting a lower limit on h_{zz}, one can sacrifice some spatial resolution in order to reduce the running time of the simulation.

Note that there is nothing fundamentally wrong with ignoring the off–diagonal terms of S. To see this, a form of $\dot{h}_i$ used by a spherical kernel code can be written

$$\dot{h}_i = \frac{1}{3\rho_i}\left(s_{xx,i} + s_{yy,i} + s_{zz,i}\right) \ . \tag{2.25}$$

In the case of a spherical kernel, one not only ignores the off–diagonal terms of S, but one also averages all three diagonal terms when determining $\dot{h}$. The advantage provided by spheroidal kernels is that one only averages two of the diagonal elements of S, allowing another degree of freedom in which the kernel can deform.

2.2 Benchmarking Spheroidal and Spherical Kernels

It has been shown that converting an existing code to use spheroidal kernels is not a monumental task. This section will examine the enhanced capabilities gained by using spheroidal kernels. The applications that have the most to gain are those which involve mass motion in a preferred direction, such as the head–on collision of two stars. After the stars contact one another, they will form a thin, disk–like structure with material shooting out in the plane of contact. This causes two conflicting requirements for a spherical kernel code, as in one direction material is being pressed together while in a perpendicular direction material is expanding. As

a consequence, spatial resolution is sacrificed in one direction, and physical contact is lost in the other. Spheroidal kernels handle this case beautifully, compressing in one direction and expanding in the other.

2.2.1 Homologous Collapse of a Zero–Temperature Cloud in 1D

A test case which will demonstrate some of the problems a spherical kernel code has with the head on collision of two stars is the homologous collapse of a zero–temperature cloud in 1D. Initially a cylindrical cloud of constant density is given a homologous velocity profile

$$v_z(z) = -v_{z0}\left(\frac{z}{z_0}\right) , \tag{2.26}$$

where z_0 is the initial height of the cylinder. This problem has a trivial analytic solution

$$\rho(t) \quad = \quad \rho_0\left(\frac{z_0}{z_0 - v_{z0}t}\right) , \tag{2.27}$$

where ρ_0 is the initial density. At a given time t, the density is constant through the cloud.

There is a complication when trying to simulate this particular problem with an SPH code. A commonly used form of the energy equation for particle i is

$$\frac{du_i}{dt} = \frac{P_i}{\rho_i^2}\sum_{j=1}^{N} m_j(\vec{v}_i - \vec{v}_j)\cdot\nabla_i W_{ij} + \frac{1}{2}\sum_{j=1}^{N} m_j \Pi_{ij}(\vec{v}_i - \vec{v}_j)\cdot\nabla_i W_{ij} , \tag{2.28}$$

where

$$\Pi_{ij} = \begin{cases} \frac{-\alpha_1 c_{ij}\mu_{ij} + \alpha_2\mu_{ij}^2}{\rho_{ij}}, & \text{if } (\vec{v}_i - \vec{v}_j)\cdot(\vec{r}_i - \vec{r}_j) \leq 0 , \\ 0, & \text{otherwise} , \end{cases} \tag{2.29}$$

and

$$\mu_{ij} = \frac{h_{ij}(\vec{v}_i - \vec{v}_j)\cdot(\vec{r}_i - \vec{r}_j)}{|\vec{r}_i - \vec{r}_j|^2 + \epsilon h_{ij}^2} , \tag{2.30}$$

and $h_{ij} = \frac{1}{2}(h_i + h_j)$, $c_{ij} = \frac{1}{2}(c_i + c_j)$, and $\rho_{ij} = \frac{1}{2}(\rho_i + \rho_j)$, where c_i is the speed of sound at the position of particle i. The constants α_1 and α_2 are of order unity, and for our test case, the values $\alpha_1 = 1$ and $\alpha_2 = 2$ were used. The constant ϵ is usually of order 10^{-4}, and is included to soften the effect of having particles in close proximity. Note that the first sum of equation (2.28) represents the heating due to PdV work while the second sum is the heating from shocks.

For now let's ignore the x– and y–components of velocity, and assume constant h for all particles. Take two neighboring particles i and j with $(z_i - z_j) \gg \epsilon^{1/2}h$. Substituting the homologous velocity profile from equation (2.26) into equation (2.30) gives, after some algebra,

$$\mu_{ij} = -h\left(\frac{v_{z0}}{z_0}\right) \ . \tag{2.31}$$

It follows from equation (2.28) that each particle will receive shock heating, despite the fact that no physical discontinuities exist in the original problem! As a consequence, the cloud will no longer be at zero temperature and the solution for the central density of the cloud will depart from equation (2.27).

To compensate for this undesired heating, one can modify equation (2.30) to be

$$\mu_{ij} = \frac{h_{ij}\Delta\vec{v}\cdot(\vec{r_i} - \vec{r_j})}{|\vec{r_i} - \vec{r_j}|^2 + \epsilon h_{ij}^2} \ , \tag{2.32}$$

where

$$\Delta\vec{v} = \begin{cases} 0, & \text{if } (z_i - z_j)(v_{zi} - v_{zj}) > 0 \ , \\ \text{otherwise,} & \\ (v_{xi} - v_{xj}, v_{yi} - v_{yj} \ , z_j\left(\frac{v_{zi}}{z_i}\right) - v_{zj}), & \text{if } |z_i| > |z_j| \ , \\ (v_{xi} - v_{xj}, v_{yi} - v_{yj} \ , v_{zi} - z_i\left(\frac{v_{zj}}{z_j}\right)), & \text{if } |z_j| > |z_i| \ . \end{cases} \tag{2.33}$$

The first condition is necessary because we only want to apply this correction to collapsing material, not expanding. The other two expressions are used in order to

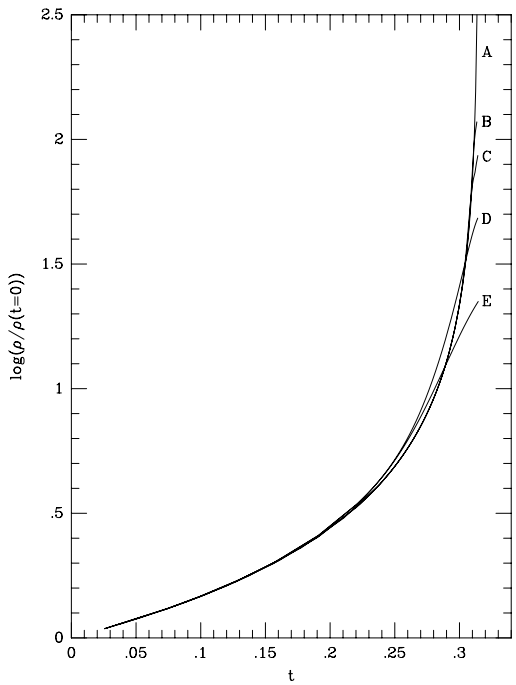

Fig. 2.1.— Central density of a homologously collapsing cold cloud versus time. The curves are A – Analytic solution, B – Spheroidal kernels, homologous contraction removed from viscosity expression, C – Spheroidal kernels, standard viscosity expression , D – Spherical kernels, modified viscosity expression (like B), and E – Spherical kernels, standard viscosity expression.

avoid dividing by a number near zero. This form of μ_{ij} will be zero if the material is undergoing homologous collapse in the z–direction, leading to no shock heating and the behavior of the central density following the analytic result.

In Figure 2.1, the results of several different SPH runs are given. The density at the center of the cylinder is plotted against time. In cases B and C, spheroidal kernels were used, while in cases D and E, a traditional spherical kernel was used. The case labeled A is the analytic result given by equation (2.27). Cases C and E used the standard expression for artificial viscosity forces, while cases B and D used the alternate expression which takes into account homologous motion. The first point demonstrated by Figure 2.1 is that the spheroidal code follows the analytic

solution to much higher density than the spherical kernel runs. The spherical models begin to overestimate the density around $t = 0.2$, due to the fact that the kernel size does not shrink as fast as the height of the cylinder. As a result, more and more particles contribute to the computation of the density at the center of the cylinder. At $t = 0.3$ and later, the spherical models yield a density which is lower than the analytic result. The innermost row of the cloud at this time is shown in Figure 2.2, which is a slice through $y = 0$ and is approximately h_{yy} thick. Here the particle kernels are shown as circles with a radius $r = h_{xx} = h_{zz}$. The circles appear as ellipses in this figure because of the differing plotting scales used for the x– and y–axes. It is clear that immediately adjacent particles in x are more than $2h_{xx}$ apart, meaning they are no longer interacting and there is no pressure force acting in the x–direction. In Figure 2.3, the entire slice through $y = 0$ is shown with the same plotting scales as Figure 2.2. The typical h_{zz} is now over one quarter the thickness of the disk, making it impossible for the code to adequately model the physics of the collapse any farther.

In contrast, examine an identical slice from the spheroidal run at the same code time ($t = 0.3$), shown in Figure 2.4. Notice that the particles are in communication in both the x– and z–directions. The ratios of h_{zz}/z_{max} and h_{xx}/x_{max} are almost equal, where z_{max} and x_{max} are the maximum extent of the disk in the z– and x–directions. This means that the spatial resolution in the x– and z–directions has been preserved even though the cylinder has shrunk by a factor of 16 in the z–direction. The spheroidal kernel runs deviate from the analytic result for $t > 0.312$, due to the fact that the initial configuration was at a small but nonzero temperature. The internal energy has grown sufficiently by $t = 0.312$ that the collapse is no longer homologous. Note that case C, which deviates from the analytic result first, uses the standard expression for artificial viscosity. Case B is

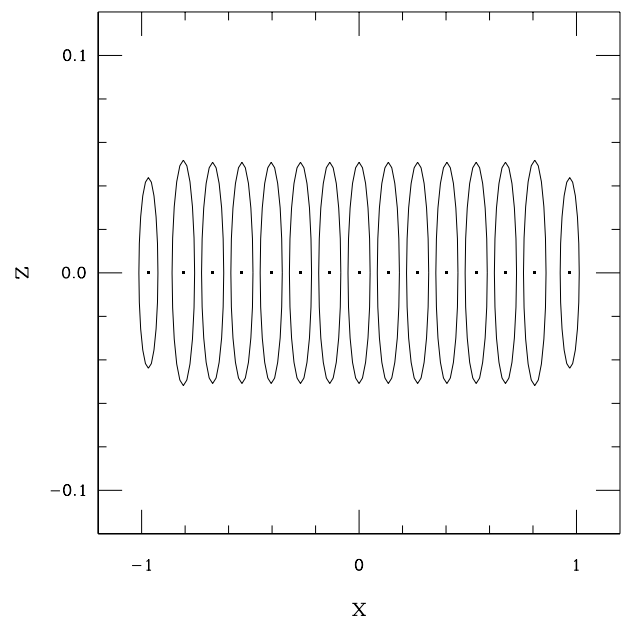

Fig. 2.2.— Innermost row of particles at $t = 0.3$ for a run using spherical kernels. The collapse is along the z–direction. Due to the different plotting scales used for the x– and z–axes, the ellipses around each particle are actually circles with radius $r = h_{xx} = h_{zz}$.

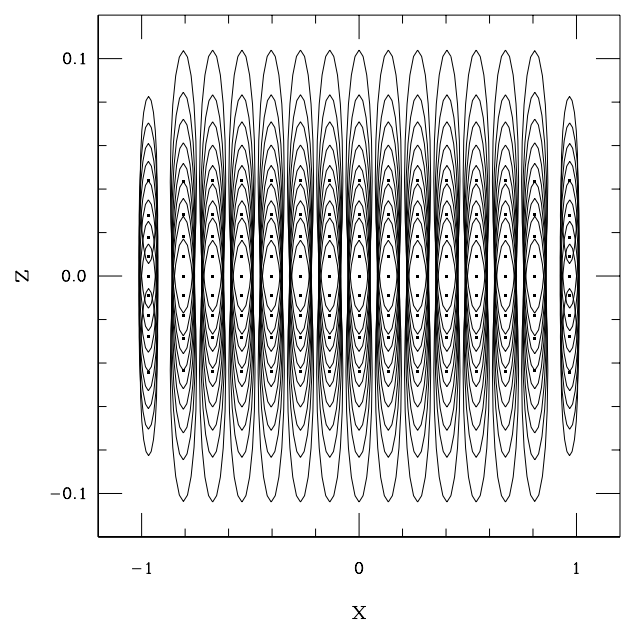

Fig. 2.3.— Same as Figure 2.2 except all particles in a slice through $y = 0$ are shown.

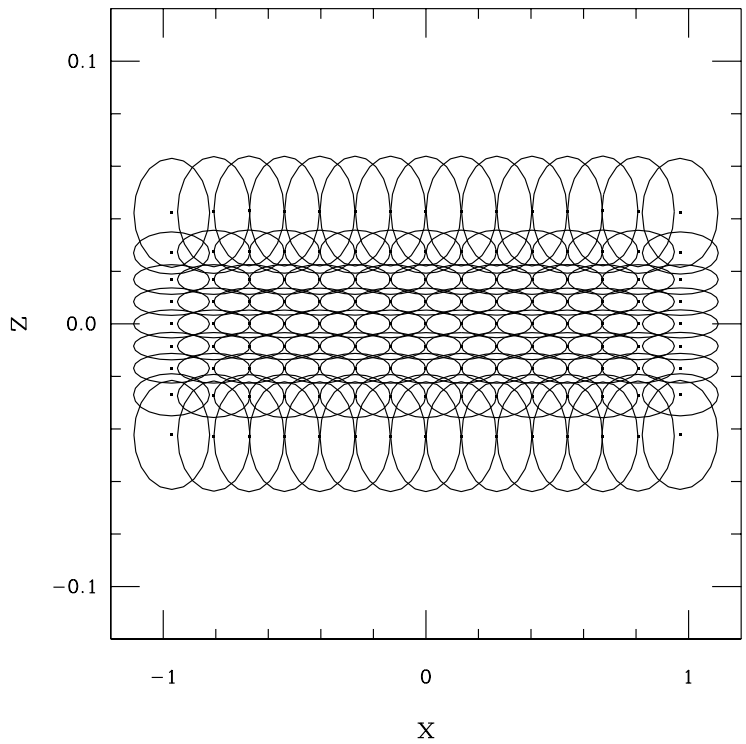

Fig. 2.4.— Particle configuration in the $y = 0$ plane at $t = 0.3$ for a run using spheroidal kernels. The collapse is along the z–direction. The ellipses around each point has a height of h_{zz} and a width of h_{xx}.

able to follow the analytic result to a later time due to the use of the modified expression for artificial viscosity. The runs were terminated at $t = 0.316$ because, by this time, the analytic result predicts an infinite central density.

The test case presented here clearly brings out the disadvantages of using spherical kernels on problems where a system undergoes substantial collapse in one direction. The underlying assumption built into any code which uses spherical kernels is that the system will deform in an essentially spherical manner. When the system strays too far from this assumption then, the simulation is no longer reliable. By allowing an extra degree of freedom for the deformation of the kernel, spheroidal kernels are able to extend the utility of smoothed particle hydrodynamics.

2.2.2 Tidal Disruption of a Star by a Massive Black Hole

The initial motivation to develop a code using spheroidal kernels came from our frustration using spherical kernels to model stellar disruptions by a massive black hole. In this problem, a star passes a massive black hole (typically 10^6 $M_\odot$) on a parabolic orbit which passes within the Roche radius r_t. We will define r_t as

$$r_t = \left(\frac{M_{bh}}{M_\star}\right)^{1/3} R_\star \ . \tag{2.34}$$

The strength of the encounter can be parameterized by $\beta = r_t/r_p$, where r_p is the closest approach of the star to the black hole. Qualitatively, one finds for $\beta > 1$ that the star will be disrupted and lose approximately one–half its material to the black hole. This process is interesting, as it may provide a way to free gas from stars to power an active galactic nucleus (Hills 1975). One finds that starting around $\beta = 5$ that general relativistic effects begin to become important. As our code currently uses the Newtonian approximation to treat gravity, the following discussion will be for $\beta \leq 5$.

The problem was examined by Carter & Luminet (1983) using an affine star model, which assumes that surfaces of constant density maintain an ellipsoidal shape. Their primary result was to bring attention to the fact that during extreme encounters (β greater than a few), there is a short period over which the central density of the star increases by a factor of order β^3. The atmosphere of the star above and below the orbital plane is set into free fall motion by the gravitational field of the black hole. The star flattens into a thin pancake–like shape before the falling material is halted by the buildup of pressure. It is at this point that the central density reaches its maximum value. Afterwards, the atmosphere bounces, and the central density monotonically drops.

Smoothed particle hydrodynamic calculations by Bicknell & Gingold (1983) confirmed the findings of Carter & Luminet qualitatively, but also found that the central density increased by a factor of only $\beta^{3/2}$, significantly lower than that predicted by Carter & Luminet. The reason for the smaller density buildup was due to the inclusion of artificial viscosity in the SPH calculation, which was not present in the affine models of Carter & Luminet. Shock heating halted the collapse of the star at a lower central density than predicted by Carter & Luminet (1983). Carter & Luminet (1986) presented new affine star models in which they included viscous effects and found that they could reproduce Bicknell & Gingold's results. They argue, however, that their results do not mean that the affine model and SPH results are correct, but rather that the agreement is due to the lack of adequate spatial resolution in the SPH runs. The Bicknell & Gingold runs did only use 500 particles. However, there is cause to believe that there is more wrong with the Bicknell & Gingold calculation than a lack of particles. A more recent SPH calculation (Laguna *et al.* 1993) with 7000 particles yielded a similar conclusion that for a $\beta = 5$ encounter, the central density increases by a factor of slightly over 10. So it appears that adding particles does not significantly change the density enhancement predicted by codes using spherical kernels.

Our efforts to duplicate the results given in the previous paragraph with a spherical kernel code met in utter failure for several reasons. Most SPH codes use a form of the Lax–Wendroff viscosity term as given in equation (2.29). The coefficients α_1 and α_2 govern the behavior of this equation. If one uses values for α_1 and α_2 which give good results in a shock tube problem, one finds that for a $\beta = 5$ encounter, the central density only increases by a factor of approximately 3, not 10. In fact, we were only able to achieve a large increase in central density by effectively turning off shock heating. As a consequence, however, the majority

of the particles involved in the simulation streamed through $z = 0$, making the results useless. The only way to prevent the mass streaming of particles is to use an anti–penetration term in the equation of motion, as suggested by Monaghan (1989). A side effect of using this term, however, is that in the presence of an external potential, the conservation of energy is compromised. A second, more significant problem is that these calculations used spherical kernels, which, as shown in the previous section, are unable to follow the one–dimensional collapse of a system beyond a compression factor of 8. As the star collapses, the spatial resolution given by the use of spherical kernels erodes to the point that one is unable to resolve the pressure gradient which causes the star to bounce. These strong encounters just cannot be modeled using spherical kernels if the central density increase is as high as previous authors have suggested.

Our new calculations of a $\beta = 5$ encounter have been designed to address the problems mentioned in the previous paragraph. As demonstrated in the previous section, the use of spheroidal kernels preserves spatial resolution in the direction of collapse while maintaining contact between particles in the plane perpendicular to collapse. In addition, we have implemented a viscosity term which is sensitive to homologous collapse. It can be shown analytically (Bicknell & Gingold 1983) that the velocity profile of the free falling material is homologous up until the time when this material bounces. As mentioned in the previous section, the standard viscosity term used in SPH calculations will produce shock heating in a homologous collapse, contrary to what *should* happen. This is why it was necessary in previous SPH simulations to use unrealistically small values for the viscous parameters in order to achieve a increase in central density of order 10 for a $\beta = 5$ encounter.

We have calculated the $\beta = 5$ encounter of an $n = 3/2$ polytrope of mass

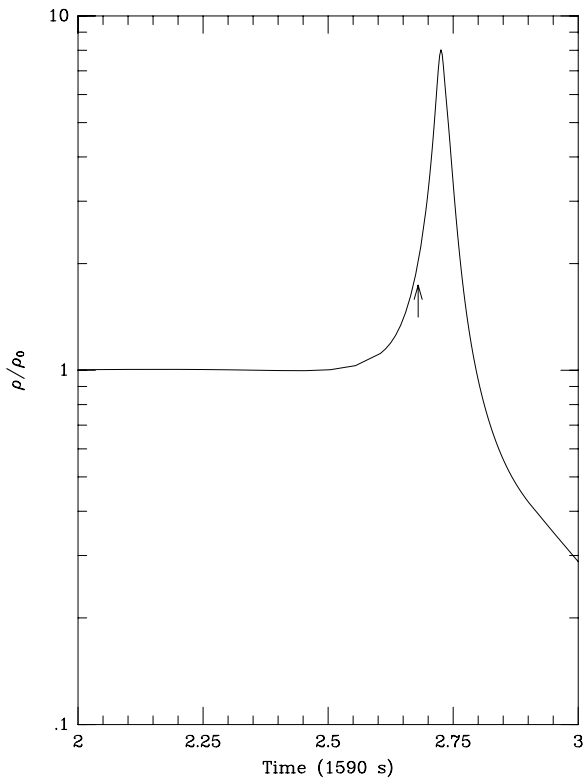

Fig. 2.5.— Central density as a function of time for a $\beta = 5$ encounter of an $n = 3/2$ polytrope. The density is scaled by the initial central density. The time of closest approach is indicated by the arrow.

1 $M_\odot$ and radius 1 $R_\odot$ with a black hole of mass 10^6 $M_\odot$. The calculation assumed an ratio of specific heats of 5/3 and used 5093 particles. The coefficients in the Lax–Wendroff viscosity term were chosen to be $\alpha_1 = 1$ and $\alpha_2 = 2$. The x–y plane was chosen as the orbital plane, which means the star will collapse parallel to the z–axis. The units used in the code are $G = R_\odot = M_\odot = 1$. In Figure 2.5, the quantity ρ/ρ_0 is shown as a function of time, where ρ_0 and ρ are the initial and current central densities, respectively. The maximum central density is 8 times the initial central density, smaller than that reported in other works. The velocity profile along the z–axis at the time of closest approach is shown in Figure 2.6. As mentioned earlier, the velocity profile is essentially homologous. The modified

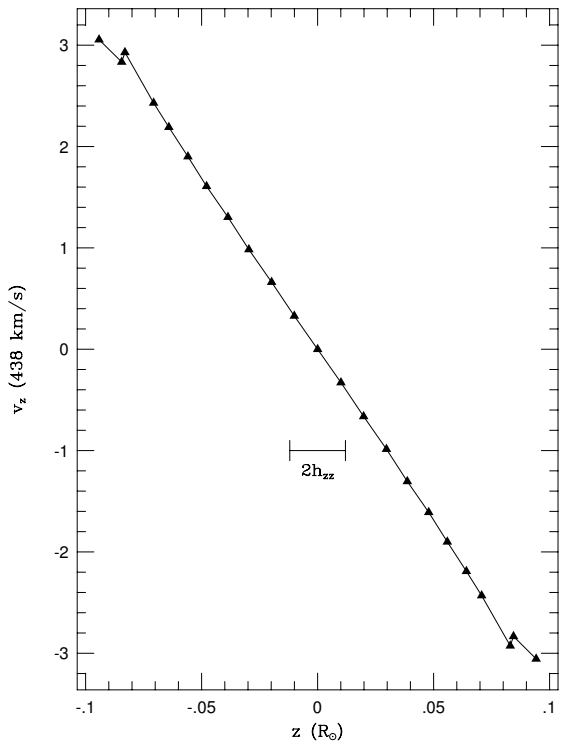

Fig. 2.6.— Z velocity profile vs. z along the z–axis at the time of closest approach for the $\beta = 5$ calculation. The bar indicates a length of $2h_{zz}$.

viscosity term used for this calculation takes into account the homologous flow, drastically reducing the erroneous heating of the gas by artificial viscosity. An indication of the enhanced spatial resolution provided by spheroidal kernels is that only 3% of the particles streamed through the orbital plane. The majority of the streaming particles were around the periphery of the star in the $z = 0$ plane. These particles have less than the average number of neighbors and therefore penetrate more easily. In addition, the average density for these particles is low, so that the streaming particles account for only 0.5% of the total mass of the star. In comparison, a similar run using spherical kernels (and no Monaghan stopping term) resulted in the majority of the particles streaming. The reason for the reduced number of streamers is that the spheroidal kernels allow our code to represent a

steeper pressure gradient than possible by a spherical kernel code. This means our code can make the collapsing material bounce without having to add the Monaghan stopping term required by a spherical kernel code.

The particle configuration at the time of maximum central density is shown in Figures 2.7 and 2.8. These are the x–y and x–z projections of the particle positions, respectively. Note the cross present in each figure which indicates a length equal to twice the typical smoothing length in each direction. The height of the star is now approximately 0.05 $R_\odot$, 20 times smaller than its initial height, while the star has extended to a length along the x–axis of 4 times its initial length. The spheroidal kernels have deformed in order to keep the relative spatial resolution along each axis roughly constant. An astute reader will notice that the star is also modestly elongated in the x–y plane. This is the plane in which the kernels must retain a circular shape, causing the smoothing length in the y–direction to approach a good fraction of the thickness of the star in that direction. Fortunately, the pressure forces in the x–y plane are small compared to the gravitational tidal forces due to the black hole. Therefore, spatial resolution in the x–y plane is not as critical as it is in the x–z plane, where one must resolve the pressure gradient which forces the star to bounce. An indication that the current code is able to resolve this pressure gradient is shown in Figure 2.9, which plots the density profile along the z–axis at the time of maximum central density. The relative spatial density, defined by the ratio z_{max}/h_{zz}, should remain constant in a homologous flow. At the time of maximum central density $z_{max}/h_{zz} \simeq 10$, comparing nicely to the initial value 8.9.

It is instructive to calculate the number of particles required by a code using spherical kernels in order to achieve a relative spatial resolution of 10 at the time of maximum compression. The smoothing length obeys equation (2.8), which can

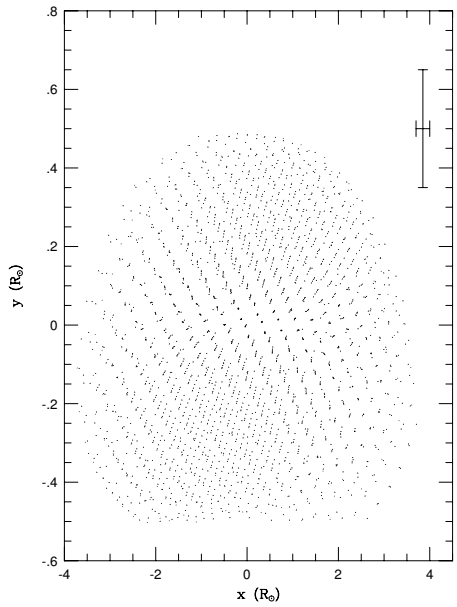

Fig. 2.7.— Projection of particle positions onto the x–y plane at the time of maximum central density for the $\beta = 5$ calculation. The cross has a length of $2h_{xx}$ in x and $2h_{yy}$ in y.

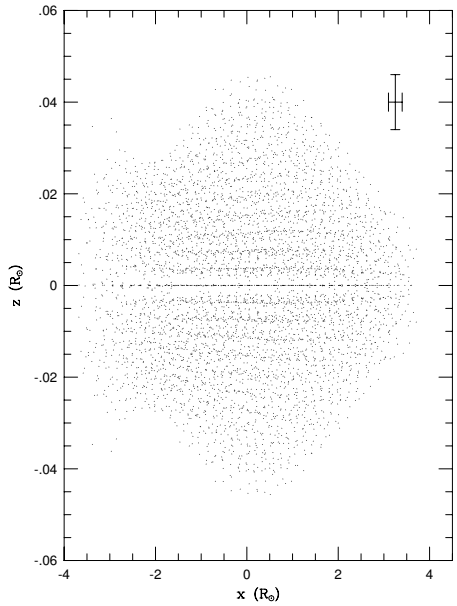

Fig. 2.8.— Projection of particle positions onto the x–z plane at the time of maximum central density for the $\beta = 5$ calculation. The cross has a length of $2h_{xx}$ in x and $2h_{zz}$ in z.

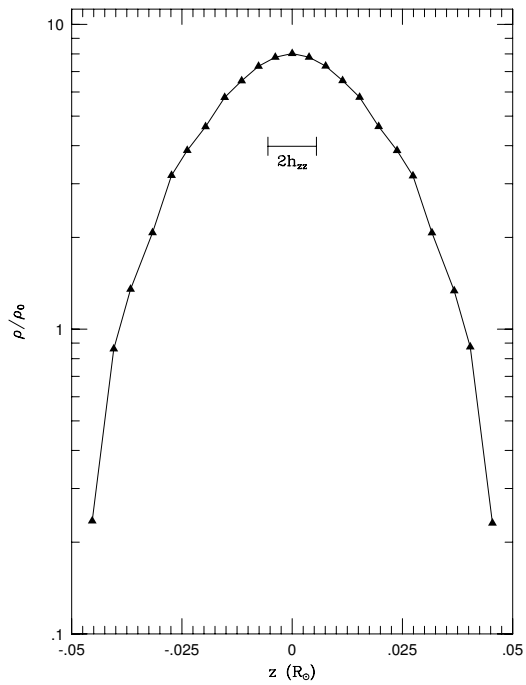

Fig. 2.9.— Density profile vs. z along the z–axis at the time of maximum density for the $\beta = 5$ calculation. The bar indicates a length of $2h_{zz}$.

be solved for h_0, the initial smoothing length

$$h_0 = h\Big(\frac{z_0}{z_{max}}\Big)^{1/3} \ , \tag{2.35}$$

where h is the smoothing length at the time of maximum compression, z_{max} is the height of the star at maximum compression, and z_0 is the initial height of the star. The values of h, z_{max}, and z_0 are approximately 0.0055, 0.055, and 1, respectively. Solving for h_0 gives $h_0 = 0.014$. The initial smoothing length for particles in a packed lattice filling a sphere of unit radius is given by

$$h_0 \simeq N^{-1/3} \ , \tag{2.36}$$

where N is the number of particles. So a spherical kernel code would require $N \simeq 3.5 \times 10^5$ particles to achieve the same relative spatial resolution at the time of maximum density as the spheroidal kernel code. But even with this number of

particles, the spherical kernel code will have another problem. The compression factor at maximum density is of order 20. As shown in the introduction to this chapter, a code using spherical kernels (independent of the total number of particles) will produce no pressure in the directions perpendicular to compression if the compression ratio is larger than 8. This means there is no way to model strong encounters between a star and a black hole using spherical kernels. One must use kernels which can deform nonspherically.

2.3 Conclusions

We have shown that systems with deformation in predominately one direction can cause major problems for an SPH code using spherical kernels. A method of SPH using spheroidal kernels was introduced which overcomes these problems by allowing the kernel to deform both along the direction of deformation as well as perpendicular to it. Initial results on the tidal disruption of a star by a massive black hole indicate that previous studies are qualitatively correct, but most likely for the wrong reasons. It is clear that for extreme encounters, in particular where general relativistic effects become important, that spherical kernels are not adequate. The nature of the problem is such that increasing the number of particles used by a spherical kernel code does not help. Instead, it is necessary to modify the smoothing kernel, as it contains a set of constraints on the deformations to an initially spherical system which can be accurately modeled. Spherical kernels imply a system that maintains spherical symmetry; likewise, spheroidal kernels imply a flattened system with axial symmetry. The ultimate realization of this concept will be ellipsoidal kernels, which, when implemented, should allow a code to produce accurate results independent of the final geometry of the system.

Chapter 3

SMOOTHED PARTICLE HYDRODYNAMICS SIMULATIONS OF THE DISRUPTION PROCESS

Hills (1975) first suggested that tidal disruption of stars by massive black holes in the center of galaxies could serve as a fuel source to power Active Galactic Nuclei (AGN). This suggestion has been examined several times since then. The stellar dynamics problem of how often stars will come close enough to a black hole to be disrupted has been discussed by Lightman & Shapiro (1977) and Cohn & Kulsrud (1978). At the time of these calculations, however, it was not computationally feasible to actually compute the hydrodynamic details of the disruption process. In order to estimate the mass accretion rate onto the black hole, these calculations assumed that there was a threshold impact parameter inside of which the star was

tidally disrupted. Once disrupted, its entire mass would be accreted by the black hole. Clearly, this is an oversimplification. Stars will encounter the black hole with a wide range of impact parameters, and the amount of mass lost by the star and the subsequent fraction accreted by the black hole may span an equally large range. Furthermore, since large impact parameters are statistically more probable, weaker encounters during which only a small amount of mass is lost could account for a significant fraction of all mass tidally stripped from stars. It is the goal of this paper to provide a more reliable estimate of the amount of mass lost by a star and accreted by the black hole.

The tidal radius r_t is the radius at which the tidal field of the black hole becomes comparable to the star's own gravitational potential. It can be defined by the relationship

$$r_t = \left\{ \frac{M_{bh}}{M_\star} \right\}^{1/3} R_\star \ . \tag{3.1}$$

Thus, the strength of a given encounter can be parameterized by $\beta = r_t/r_p$, where r_p is the closest approach of the star to the black hole. A larger value of β indicates a stronger encounter. We note that the strength of an encounter has also been defined (Press & Teukolsky 1977) by

$$\eta = \left\{ \frac{M_\star}{M_{bh}} \right\}^{1/2} \left\{ \frac{r_p}{R_\star} \right\}^{3/2} \ . \tag{3.2}$$

In this chapter, we shall use β to characterize a given encounter unless otherwise noted. To convert, one would use the relationship $\eta = \beta^{-3/2}$.

The problem of determining the fate of a star entering the tidal radius is a complicated problem that requires either a relatively sophisticated analytical model or three–dimensional numerical calculations. While distant encounters are relatively easy to model, close encounters present a number of challenges essentially

associated with the large change of scales taking place. The star is compressed significantly in the direction perpendicular to the orbital plane while it is being stretched enormously in the orbital plane. Furthermore, for encounters approaching the Schwarzschild radius, relativistic effects become important. As the mass of the black hole M_{bh} increases, the Schwarzschild radius grows as M_{bh}; however, the tidal radius r_t only grows as $M_{bh}^{1/3}$. Therefore, these relativistic effects become important for milder and milder encounters with increasing black hole mass.

The analytical model by Carter & Luminet (1983) was the first examination of the behavior of a star during strong encounters with a black hole. The main assumption of their affine model was that contours of equal density remained concentric ellipsoids. In addition, the stellar material was treated as an ideal gas that only underwent adiabatic transformations. General relativistic effects were also included in a later paper (Luminet & Marck 1985). It was found that for encounters stronger than $\beta \sim 5$, there is a period during which the center density of the star grows by a factor of β^3, and the central temperature grows by a factor of β^2. They coined the phrase "pancake phase" to describe this period, due to the appearance of the star. Given the large increase in the central temperature and density, it was suggested that the resulting enhanced nuclear burning rates could blow the star apart. However, because in these same extreme encounters the star departs from a mass distribution consistent with the main assumption of the affine method, the findings of Carter & Luminet remain on uncertain ground. Only three–dimensional hydrodynamic calculations seem able to answer the questions surrounding a strongly disruptive encounter of a star with a black hole.

Numerical calculations of mild encounters ($\beta < 1$) have been carried out recently by Khokhlov *et al.* (1993). Using a three–dimensional finite–difference

code, they simulated encounters in which stars were modeled as polytropes of index $n = 3/2$ and $n = 3$. However, because of the finite extent of the computational volume imposed by the grid, they were unable to follow the material stripped from the star during stronger encounters ($\beta > 1$).

Three–dimensional numerical simulations of deeper encounters ($\beta \geq 1$) have been been performed using exclusively the Smoothed Particle Hydrodynamics (SPH) method (Bicknell & Gingold 1983; Evans & Kochanek 1989; Laguna *et al.* 1993). These simulations have explored the regime in which the star, modeled as polytrope of index $n = 3/2$, is completely disrupted ($\beta \geq 1$). Carter & Luminet, as mentioned above, have shown that during the early phases of encounters with $\beta > 1$ that there is a period during which the central density of the star increases dramatically. While Carter & Luminet found that this density increase scales as β^3, the numerical simulations of both Bicknell & Gingold and Laguna *et al.* obtain an increase scaling as $\beta^{3/2}$. While the importance of this effect on the overall problem of the feeding of the black hole is probably negligible, it has become a point of contention between numerical models and analytical solutions.

As demonstrated in Chapter 2, the SPH method suffers from the fact that the kernel used to compute the spatial derivatives has a spherical geometry whose extension, given by the smoothing length h, scales with the cube root of density. Thus, the scaling is perfect for a spherical collapse or expansion, but not when the compression (or expansion) is unidirectional. In this case, the scaling of the kernel results in a smoothing length too large along the direction of compression and too small in the other directions. As shown in Chapter 2, this produces serious problems in unidirectional compressions resulting in a density increase beyond a factor of 8. When translated to tidal encounters, this implies that the standard

SPH technique is unable to follow realistically encounters deeper than $\beta \simeq 5$.

While the general case in which kernels are triaxial ellipsoids leads to severe angular momentum conservation problems, this is not the case for the more restrictive case in which spheroids are used, as shown in Chapter 2. The use of such kernels which scale differently in the direction perpendicular to the orbital plane than in the plane allows the simulation of very deep encounters ($\beta \geq 5$). In addition, it is now possible to follow the evolution through the pancake phase with adequate spatial resolution to model the bounce of the atmosphere of the star and the subsequent re–expansion (see Section 3.3). We note that the work of Bicknell & Gingold already made use of nonspherical kernels but in a more rudimentary fashion.

3.1 Numerical Method

In these simulations, we have employed an SPH code that uses spheroidal kernels, in contrast to prior simulations which have almost exclusively used spherical kernels (with the exception of Bicknell & Gingold). The innovations present in our SPH code and the resulting improvements over a spherical kernel code were discussed in Chapter 2. In an SPH code, the smoothing kernel W provides the means to interpolate physical quantities such as density using an expression like

$$\rho(\vec{r}) = \sum_j m_j W(\vec{r} - \vec{r}_j, h_j) \ . \tag{3.3}$$

Here, m_j and h_j are the mass and smoothing length of particle j, respectively. The smoothing function $W(\Delta\vec{r}, h_j)$ in a code using spherical kernels becomes $W(\Delta r, h_j)$, and the above sum is performed over all particles for which $W(\Delta r, h_j)$

is nonzero. Typically, a kernel W is chosen so that it becomes zero at the distance of a few h.

As mentioned above, during the pancake phase of the star's disruption, a code using spherical kernels proves to be inadequate. The only way to correct this problem is to change the smoothing kernel W so that it is no longer spherically symmetric, allowing it to follow the flow. We have chosen to use a kernel with two degrees of freedom, with contours of equal W having the shape of concentric spheroids. Instead of specifying a smoothing length h for each particle, one must specify the smoothing tensor H,

$$H = \begin{pmatrix} h_R & 0 & 0 \\ 0 & h_R & 0 \\ 0 & 0 & h_{zz} \end{pmatrix} . \tag{3.4}$$

An illustration of the kernel corresponding to the smoothing tensor H is given in Figure 3.1. In the simple case of a spherical kernel, $h_R = h_{zz}$. The primary feature of spheroidal kernels is that the kernel can change its size along the direction of h_{zz} independently of its size in the plane orthogonal to h_{zz}. During the pancake phase the kernels of the particles can also flatten into pancake–like shapes, providing the required spatial resolution.

A few modifications to the method presented in Chapter 2 should be noted. As previously mentioned in Chapter 2, it became clear that when using spheroidal kernels, it is necessary to limit how small h_{zz} can become. If this is not done, then h_{zz} can take on a very small value, leading to excessively short time steps. In some cases, h_{zz} takes on small values because the problem demands it (such as in the case of a $\beta \geq 5$ encounter between a star and a massive black hole), and therefore limiting how small h_{zz} can become basically trades spatial resolution for faster computation time. In our calculations we have set the lower limit for h_{zz} so that

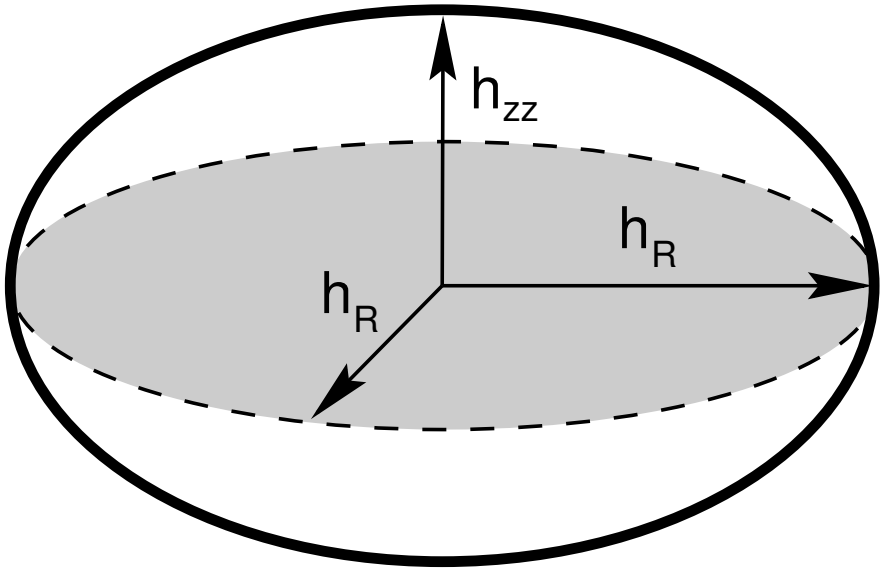

Fig. 3.1.— A graphical interpretation of the spheroidal smoothing tensor H.

we favor resolution over speed, since we are interested in resolving the density spike at the center of the star during the pancake phase.

In other cases, h_{zz} appears to take on unreasonable values due to the fact that the particles near the periphery of the star have considerably fewer neighbors than a typical particle. This effect is a consequence of the fact that the velocity derivatives entering the calculation of the smoothing tensor (see Chapter 2), essentially the strain–rate tensor, are calculated less accurately near edges. Also, we note that our prescription for updating the tensor components based on the strain–rate tensor is ill–adapted to pure shear flows. Recent experiments in which we use the derivatives of the local moment of inertia instead of the strain–rate tensor show that these problems can be avoided. We plan to use this improved technique in the future. In any case, erroneous values of the components of the smoothing tensor lead to less accurate estimates of quantities such as density and the velocity gradient. If h_{zz} is allowed to evolve unrestrained using these more noisy estimates, it can take on

unreasonably small (or large) values. Therefore, it is necessary to restrict h_{zz} to avoid this undesired behavior.

In addition to limiting how small h_{zz} can become, the code also now checks to see how many neighbors a particle has before allowing the volume of the kernel to increase. Otherwise, we found that some particles would have kernels which would grow to unreasonably large values. It should be noted that the particles affected by these restraints on the kernel are primarily particles that have escaped the star. The internal energy of these particles is decreasing rapidly due to adiabatic expansion; thus, the trajectory of these particles is essentially ballistic and is only slightly affected by these kernel problems.

Our calculations use a constant gravitational smoothing length τ for gravitational interactions between gas particles, as is commonly done in N–body simulations. The gravitational force between a gas particle and the black hole (represented by a point mass) is not smoothed, since the gas particles never come close enough to the black hole during the calculation for this to become important. We also employ the modified viscosity term given by equation (2.29). This modified term attempts to take into account the fact that the collapse of the star in the direction perpendicular to the orbital plane is roughly homologous, and, as a result, there should be no shock heating. Unfortunately, owing to the functional form of the artificial viscosity used in the standard SPH method, entropy is increasing unreasonably, leading the star to bounce prematurely. As will be discussed in Section 3.3.2, our modified viscosity term significantly reduces the amount of heating from shocks up to the pancake phase. The improved spatial resolution due to our use of spheroidal kernels, as well as the improved treatment of shock heating through the use of the modified viscosity term, are both important advances in the

modeling of the tidal disruption of stars.

3.2 General Notes Concerning the Simulations

In this work, we will be approximating the internal structure of real stars by using polytropes of the appropriate index. Since we are interested in the tidal disruption of stars in galactic nuclei, we must first decide which kinds of stars will be predominately disrupted. In the solar neighborhood, it is found that the majority of the mass in stars is in the form of M and K dwarfs (Rana 1987). The internal structure of these stars can be represented by a polytrope of index $n = 3/2$. We will assume that the Present Day Mass Function (PDMF) in galactic nuclei is similar to that found in the solar neighborhood. Therefore, the simulations of encounters of an $n = 3/2$ polytrope with a black hole will be the most important. However, in order to give the problem a more general treatment, we will also perform several simulations using an $n = 3$ polytrope, which adequately represents stars of nearly solar mass and greater.

Although the number density of giants is expected to be significantly smaller than that of M and K dwarfs, according to equation (3.1), the tidal radius for a giant is potentially an order of magnitude greater than that of an M dwarf. This means that the disruption of a giant can occur within a greater volume than the case for an M dwarf, so that the mass stripped from giants might be comparable to that from low mass stars. However, when this problem was considered by Lacy *et al.* (1983), in the context of the center of the Milky Way, they found that the disruption of giants is not a major source of material. In producing this result, they estimated that the number density of red giants N_{RG} is $\leq 10^{-3} N_{MS}$, where N_{MS} is the number density of main–sequence stars. In addition, they assumed that

the typical radius of a red giant is $20R_{MS}$. This leads to a disruption rate for red giants which is only a few percent of that for main–sequence stars. The disruption of giants is important for black holes with a mass greater than 10^8 $M_\odot$, as the tidal radius for main–sequence stars for such large black holes is actually smaller than the size of the event horizon. This means that main–sequence stars will simply be swallowed without being disrupted. Giant stars, however, will still be disrupted and can provide fuel for the central AGN. For the purposes of the present work, however, it will be sufficient to consider the disruption of main–sequence stars, represented in our simulations by polytropes.

The units employed for our calculations set 1 $R_\odot$ = 1 $M_\odot$ = G = 1, resulting in the code units given in Table 3.1. In all cases, the star has a mass of 1 $M_\odot$ and a radius of 1 $R_\odot$. The orbit of the star is initially parabolic in all cases. The orbital plane is the x–y plane, so the star is compressed in the z–direction during the pancake phase. Therefore, we have aligned the h_z axis of the spheroidal kernel along the z–axis. The simulations with $n = 3/2$ use 5093 particles, while the $n = 3$ simulations use 2351 particles. The particles are initially placed on a hexagonal lattice, and the spacing of the particles in both cases is identical. The reason that the two cases have different numbers of particles is because in the $n = 3$ case, the particles do not extend as far out spatially as in the $n = 3/2$ case. This is a result of the more centrally concentrated nature of the $n = 3$ polytrope. To have used 5093 particles in the $n = 3$ case would have resulted in the inefficient situation of over half of the particles representing less than 0.4% of the mass of the star. In all cases the kernel of each particle is initially spherical with a radius of 0.1, leading to a typical particle having 40–45 neighbors. We restrict h_{zz} to become no smaller than 0.001, unless otherwise noted. The volume of a particle's kernel is not allowed to increase if the particle has more than 100 neighbors. The constant gravitational

Table 3.1: Units used in these calculations.

Quantity	Code Unit	
Distance	6.960×10^{10}	cm
Mass	2.000×10^{33}	g
Time	1.590×10^{3}	s
Velocity	4.378×10^{7}	cm/s
Density	5.932	g/cm^3
Energy	3.833×10^{48}	ergs

smoothing length τ is set to a value of 0.05, one–half of the starting value of h_{zz}. The only time the separation between particles becomes small compared to τ is during the pancake phase. However, at this point, the internal energy of the gas is considerably larger than the self–gravitational potential of the star, so excessively smoothing the gravitational interaction of the particles should not have a significant effect. Finally, the viscosity coefficients used in the modified viscosity term given by equation (2.29) are $\alpha_1 = 1$ and $\alpha_2 = 2$, which are typical values used in SPH simulations.

We use a third–order Runge–Kutta integrator with adaptive time steps (Fehlberg 1969) to solve the equations of motion and energy (we use internal energy to close our set of equations). We found a high–order integrator necessary because we perform the computation in the frame of the center of mass of the system. Using a second–order method resulted in considerably smaller time steps, and the extra derivative evaluation of the third–order method was compensated for by a larger time step. We also use double–precision variables to represent the position, velocity, and force on a given particle. This was necessary because the internal hydrodynamic forces of the star can be several orders of magnitude smaller than the gravitational force due to the black hole. Since the tidal force is due to

the differences in these large values, it was necessary to be able to represent a large dynamic range accurately in order to follow the hydrodynamics properly.

The energy conservation in these calculations varied depending on the strength of the encounter and the mass of the black hole. But it was typically good to 5% of the binding energy of the star for $M_{bh} = 10^6$ $M_\odot$, with a few cases of the error being greater. For $M_{bh} = 10^4$ $M_\odot$, we found the error was a factor of 5–10 less than for $M_{bh} = 10^6$ $M_\odot$. After considerable investigation into the nature of this energy error, we believe that errors due to the handling of the hydrodynamics are minor. The primary source of error is in the integration of the orbit of the star about the black hole. A small error in the location of the center of mass of the star can lead to a considerable error in the total energy, due to the steep gravitational potential well of the black hole. The energy error was greater in the $M_{bh} = 10^6$ $M_\odot$ case because the potential well was deeper.

Our primary motivation for performing these calculations was to determine how much mass is lost from the star for an encounter with a given β and polytropic index n. In order to determine the fate of the material stripped from the star, we employed the following algorithm, which was inspired by a similar method described by Lai *et al.* (1993). One first assumes that a gas particle can belong to one of three components: the star, the black hole, or free material unbound from both the star and the black hole. Initially, one assumes that all of the gas particles are part of the star component. One then computes a specific energy for each particle relative to the black hole and relative to the star. The form of the specific energy for particle i relative to component k (where k can be either the star component or the black hole component) is

$$\epsilon_{i,k} = u_i + \frac{1}{2} v_{rel,k}^2 - \Omega_{i,k} \ , \tag{3.5}$$

where

$$\vec{v}_{rel,k} = \vec{v}_i - \vec{V}_k \ . \tag{3.6}$$

Here, u_i and $\vec{v}_i$ are the internal energy and velocity of particle i. The velocity $\vec{V}_k$ is the center of mass velocity of component k, and $\Omega_{i,k}$ is the gravitational potential of particle i relative to component k. This means the potential relative to all other particles in the star component must be calculated to determine $\Omega_{i,\star}$. But, for the black hole component, only the potential of the particle relative to the black hole is determined; the other gas particles in the black hole component are ignored. Likewise, the center of mass velocity of the black hole component ignores the gas particles in the black hole component, using only the center of mass velocity of the black hole instead.

Once $\epsilon_{i,k}$ is computed for each particle relative to the star and black hole components, one then reassigns each particle to the appropriate component. If the particle has a negative specific energy relative to the star component, the particle is given to the star component. If the particle is unbound from the star, but bound to the black hole, it becomes part of the black hole component. Lastly, if it is unbound from both the star and the black hole, the particle is then considered part of the unbound component. When all particles have been reassigned, the whole process is iterated again. This includes recalculating $\vec{V}_\star$ and $\Omega_{i,\star}$ for each iteration. When each particle remains in the same component for two consecutive iterations, the procedure has converged for that particular time in the simulation. At the start of the simulation ($t = 0$), all of the material is in the star component. After closest approach, material is stripped from the star so that the amount of material in the unbound and black hole components increases, whereas the amount in the star component decreases. We stop the simulation when the mass in each component

has settled down to a constant value. For weaker encounters ($\beta < 1$), the star has moved to a distance of $\sim 20r_t$ at this time, while for strong encounters with $\beta \simeq 3$ or greater the convergence is much more rapid.

3.3 Results for $n = 3/2$

These models are intended to simulate the mass stripping from a fully convective star, corresponding most closely to main–sequence stars with a mass less than 1 $M_\odot$. A polytrope of solar mass and radius was used for each of the cases presented here. The ratio of specific heats was given a value of $\gamma = 5/3$. The majority of these runs were computed with $M_{bh} = 10^6$ $M_\odot$, which is within an order of magnitude of the suspected central black hole mass in many nearby galaxies (see Kormendy 1993 for a recent review). The tidal work done on the star for a given β should be fairly independent of M_{bh} for all $M_{bh} \gg M_\star$. It was shown by Press & Teukolsky (1977) that the energy pumped into the star is dominated by the quadrupole tide (the $l = 2$ oscillation), and that the magnitude of this mode is dependent only on η and independent of M_{bh} for $M_{bh} \gg M_{star}$. As shown earlier, $\eta = \beta^{-3/2}$, meaning the energy deposited into the star is also only dependent on β, independent of the mass of the black hole. In order to test this hypothesis, we have computed a selected set of the $M_{bh} = 10^6$ $M_\odot$ cases with $M_{bh} = 10^4$ $M_\odot$.

We begin the presentation of our $n = 3/2$ results with an examination of the quantity of material stripped from the star as a function of β, as well as the fallback time of the debris (Section 3.3.1). In Section 3.3.2, the pancake phase and the increase in central density for a given β will be discussed. Finally, in Section 3.3.3, the energy pumped into the star for nondisruptive encounters will be examined and compared to the finite–difference calculations of Khokhlov *et al.* (1993).

Table 3.2: Mass fractions for $n = 3/2$ and $M_{bh} = 10^6$ $M_\odot$ as a function of β.

β	M_{star}	M_{bh}	M_{free}
0.4	1.000	0.000	0.000
0.5	1.000	0.000	0.000
0.6	0.964	0.018	0.017
0.7	0.781	0.111	0.108
0.8	0.503	0.255	0.242
1.0	0.094	0.453	0.453
1.5	0.076	0.459	0.465
2.0	0.000	0.500	0.500
3.0	0.000	0.500	0.500
5.0	0.000	0.500	0.500

3.3.1 Stripped Material

Using the iterative procedure outlined in Section 3.2, we have determined the mass fraction of the star that ends up either bound to the black hole (M_{bh}), bound to the star (M_{star}), or unbound from both the star and the black hole (M_{free}). The mass fractions for the $n = 3/2$ runs are given for $M_{bh} = 10^6$ $M_\odot$ in Table 3.2, and for $M_{bh} = 10^4$ $M_\odot$ in Table 3.3. Both tables are plotted together in Figure 3.2. As expected, since $M_{bh} \gg M_\star$ in both cases, the two tables are in good agreement. The amount of material stripped increases rapidly near $\beta = 0.8$, with only 4% being stripped for $\beta = 0.6$, while over 90% is stripped for $\beta = 1$.

The transition from minimal mass loss to almost complete disruption is shown in Figure 3.3, which displays the density in the orbital plane for several values of β at the time when the star has moved a distance of $7r_t$ from the black hole. The innermost contour is at 80% of the maximum density of the material, and the subsequent contours are a factor of 10 smaller than the previous. There is clearly a

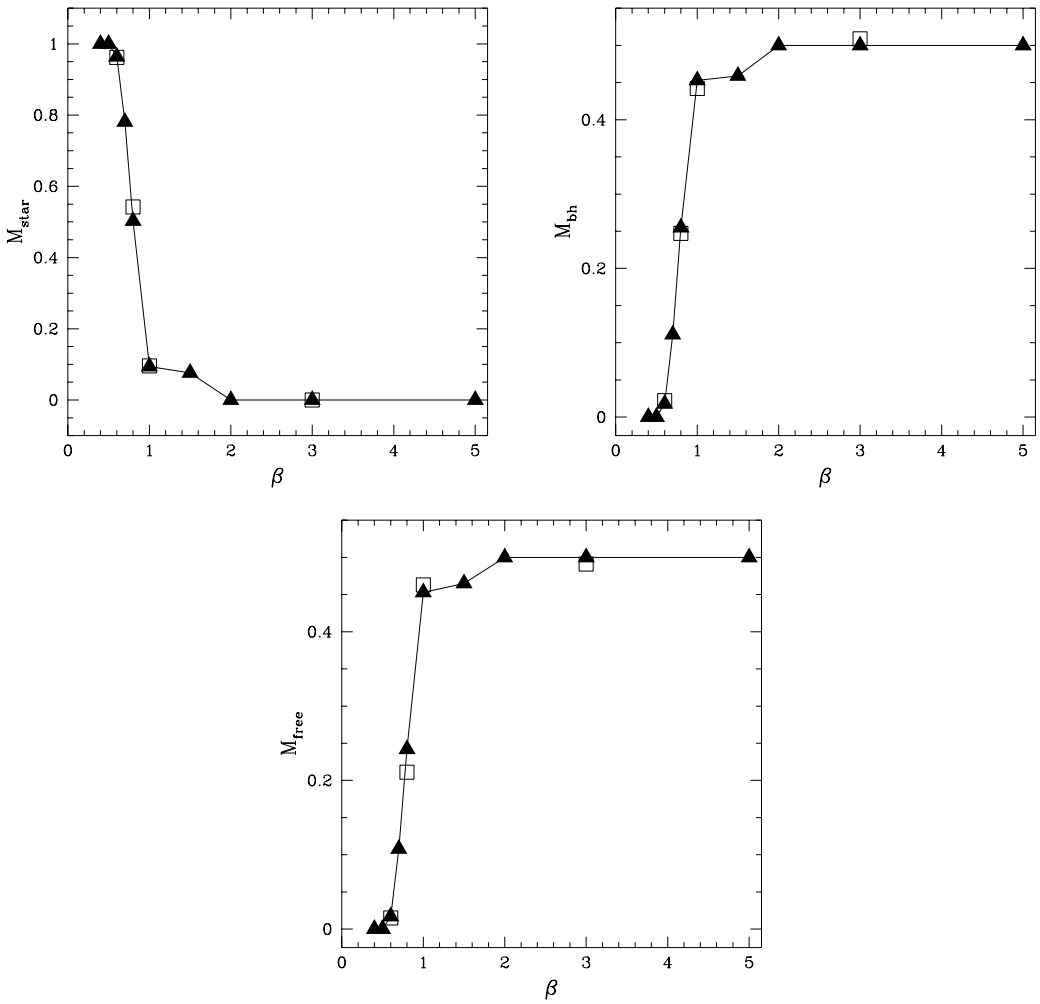

Fig. 3.2.— The stripped mass fractions for an $n = 3/2$ polytrope. The filled triangles and the solid curve are the results for a black hole mass of 10^6 $M_\odot$, and the open squares are the results for 10^4 $M_\odot$.

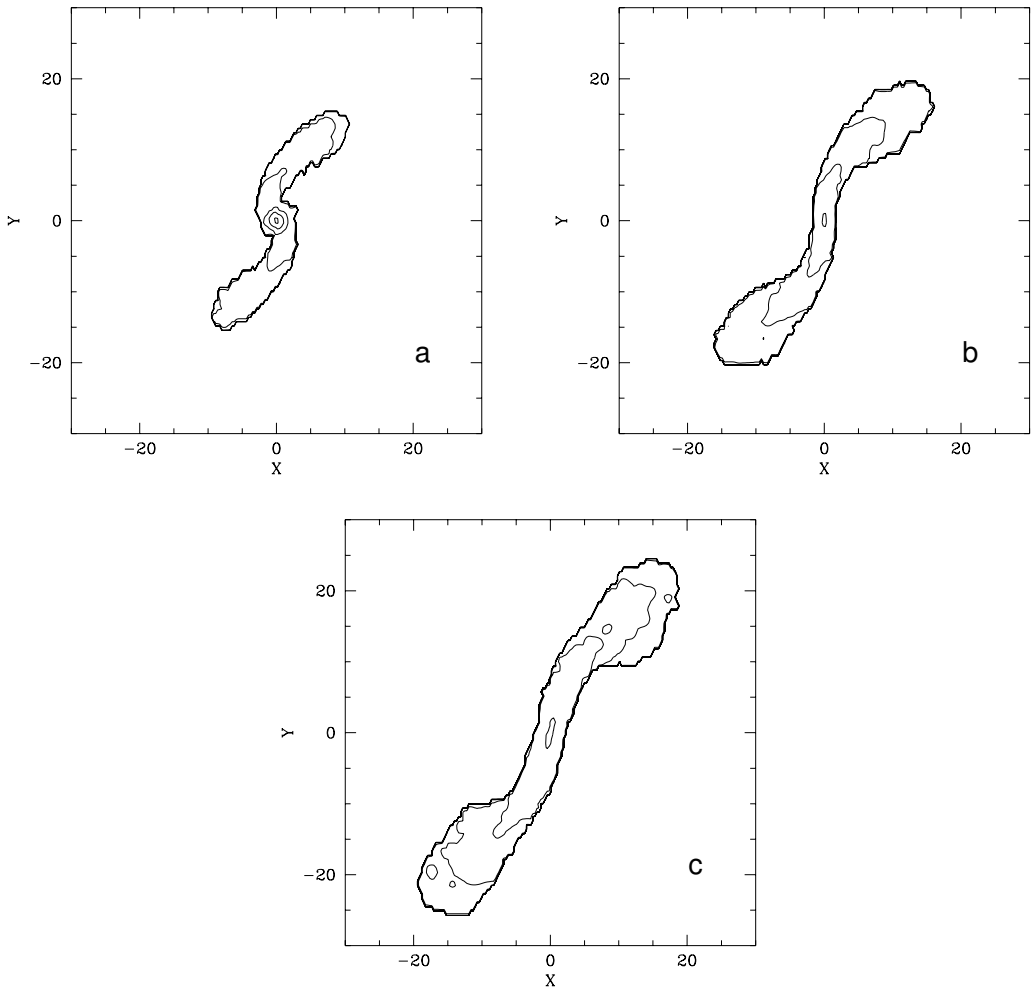

Fig. 3.3.— Density of the star in the orbital plane for several $n = 3/2$, $M_{bh} = 10^6$ $M_\odot$ encounters: (a) $\beta = 0.6$, (b) $\beta = 0.8$, and (c) $\beta = 1$. In each case the star has already made its closest approach to the black hole and has now moved to a distance of $7r_t$. The innermost contour is at 80% of the maximum density, and each subsequent contour is a factor of 10 smaller. The values of the innermost contour for these frames are (a) 0.532, (b) 0.0448, and (c) 0.0130.

Table 3.3: Mass fractions for $n = 3/2$ and $M_{bh} = 10^4$ $M_\odot$ as a function of β.

β	M_{star}	M_{bh}	M_{free}
0.6	0.962	0.022	0.015
0.8	0.542	0.247	0.211
1.0	0.096	0.442	0.463
3.0	0.000	0.509	0.491

remnant of the original star present for the case of $\beta = 0.6$, with only a few percent of the mass of the original star ripped away in the form of two tails. A considerably weaker remnant is still present in the case of $\beta = 0.8$. Finally, for $\beta = 1$, the stellar remnant is almost completely gone and the vast majority of the material extends into two large tails. For a given β, the mass in each tail is roughly equal. One tail contains the material unbound from both the star and the black hole, while the material in the other tail will fall back onto the black hole.

Although the mass stripped for a given β is fairly independent of the black hole mass, the resulting specific energy and period distributions of the material bound to the black hole differs considerably. A good estimate of the expected spread in the specific energy of the gas after disruption is given by (Lacy *et al.* 1982)

$$\Delta\epsilon \simeq \frac{G\ M_{bh}\ R_\star}{R_p^2}\ , \tag{3.7}$$

where R_p is the closest approach of the star to the black hole. Like Evans & Kochanek (1989), we will use the specific energy distribution $dM/d\epsilon$ (measured in units of $M_\odot$ $(\Delta\epsilon)^{-1}$), and the period distribution dM/dP (measured in units of $M_\odot$ yr^{-1}). These distributions are given for selected β in Figure 3.4 for $M_{bh} = 10^6$ $M_\odot$ and Figure 3.5 for $M_{bh} = 10^4$ $M_\odot$. The distributions for $\beta = 1$ and $M_{bh} = 10^6$ $M_\odot$ compare favorably to those given by Evans & Kochanek (1989).

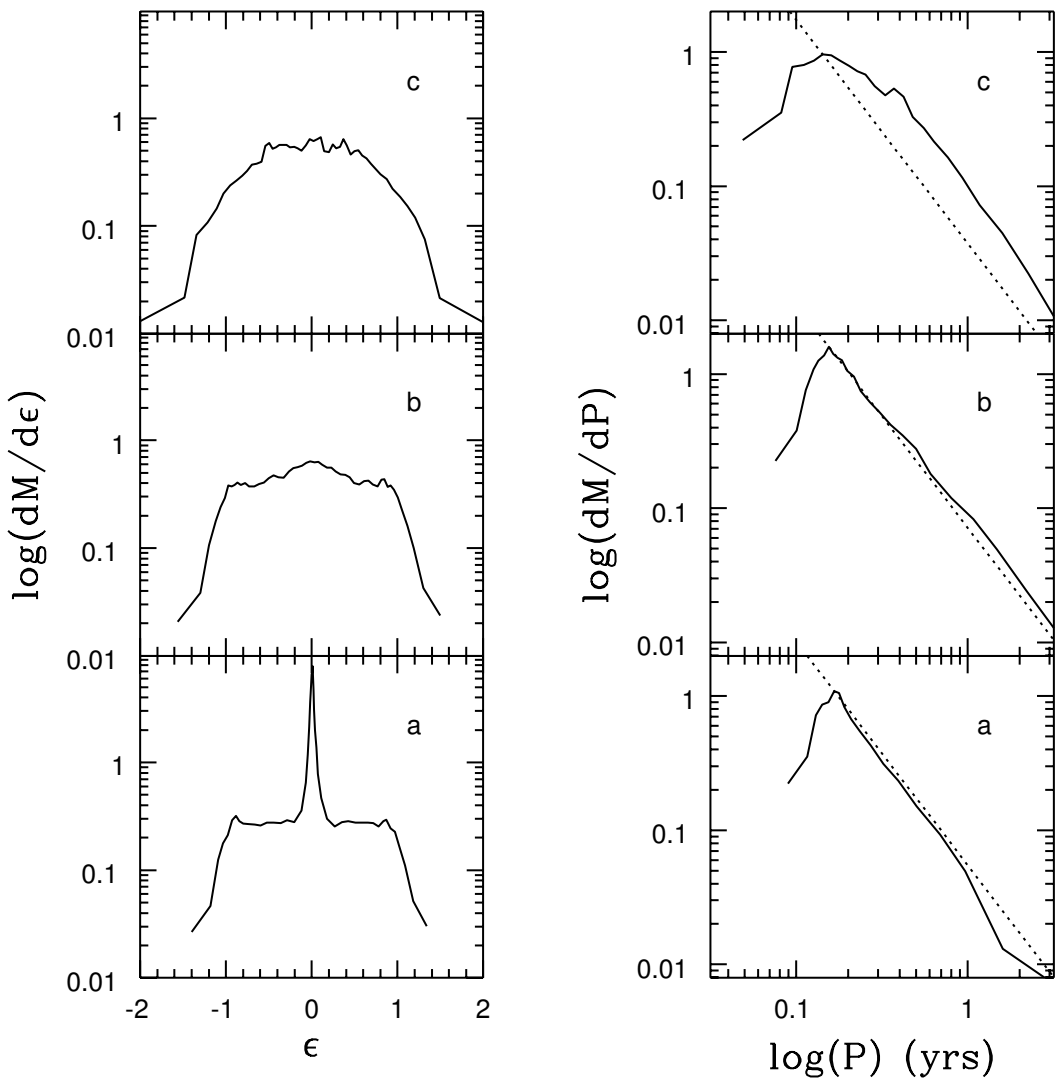

Fig. 3.4.— Energy and period distribution of stripped material for different values of β for a black hole mass of 10^6 $M_\odot$ and polytropic index $n = 3/2$: (a) $\beta = 0.8$, (b) $\beta = 1$, and (c) $\beta = 3$.

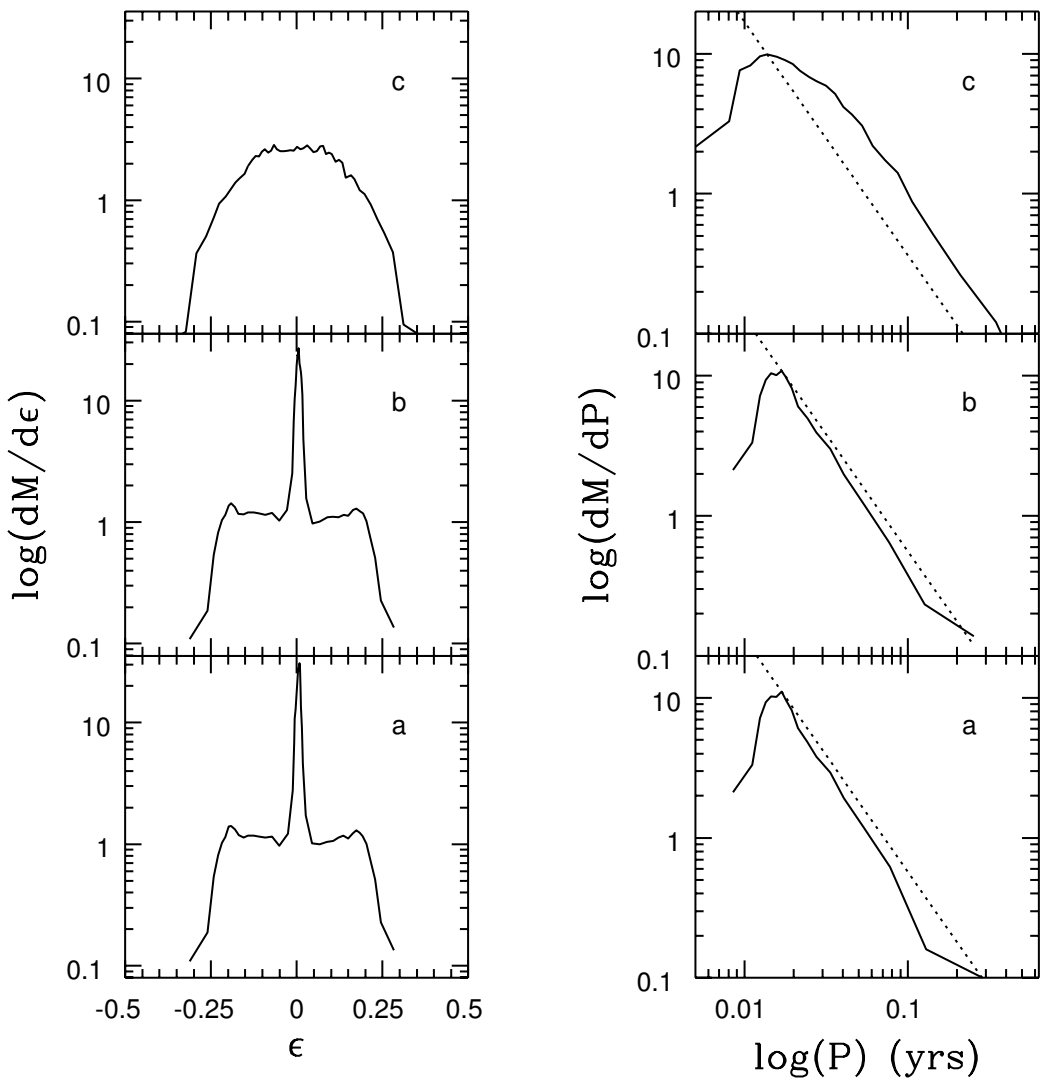

Fig. 3.5.— Energy and period distribution of stripped material for different values of β for a black hole mass of 10^4 $M_\odot$ and polytropic index $n = 3/2$: (a) $\beta = 0.8$, (b) $\beta = 1$, and (c) $\beta = 3$.

The characteristic feature of the specific energy distribution is a broad, flat peak with a width of order $2\Delta\epsilon$. Our simulations show that the width of the peak does not appear to depend strongly upon β. We note that in the cases where the star is not completely disrupted, there is also a sharp inner peak that corresponds to the material in the stellar remnant. Assuming that the specific energy distribution $dM/d\epsilon$ is constant, one can derive a period distribution of (Rees 1988; Phinney 1989; Evans & Kochanek 1989)

$$\frac{dM}{dP} \simeq \frac{1}{3}\,\frac{M_\star}{P_m}\,\left(\frac{P}{P_m}\right)^{-5/3}\,, \tag{3.8}$$

where P_m is the shortest period of the gas bound to the black hole.

Because the true $dM/\Delta\epsilon$ is not a flat curve, the power law dependence of dM/dP will not start at the shortest period of the bound gas in our numerical experiment. Instead, it will start at a period which corresponds to the specific energy where $dM/\Delta\epsilon$ becomes flat. Due to the steep sides of the specific energy distribution curve, the power law dependence of dM/dP starts at approximately its peak value. For the sake of comparison, a $P^{-5/3}$ power law normalized to the peak of dM/dP has been plotted in each of the period distributions presented in Figures 3.4 and 3.5. One finds that for $\beta > 1$, there are discrepancies between the numeric and analytic predictions. This is due to the fact that for larger β, the specific energy distribution has become quite rounded. Even so, the spread in the specific energy of the gas does not vary much for the range of $0.6 \leq \beta \leq 5$. The period at which the peak of dM/dP occurs is also fairly independent of β. This, coupled with the fact that dM/dP is roughly a power law for all β, means one can reasonably assume that for given M_{bh}, the time scale for stripped material to return to the vicinity of the black hole is independent of β over the range of our calculations, $0.6 \leq \beta \leq 5$.

3.3.2 The Pancake Phase

A point that has lead to a number of controversies between numerical models and analytical calculations is the increase in central density and temperature during the pancake phase. Carter & Luminet (1983) first suggested that for extreme encounters ($\beta > 5$), the enhancement in density and temperature is enough to cause significant energy release from nuclear burning. This additional energy could blow the star apart with enough force that very little of the escaping material could be captured by the black hole. In regard to AGNs, this would mean that encounters with a β greater than some threshold value would, contrary to intuition, yield very little material to fuel the black hole. Subsequent numerical work by other researchers using SPH simulations yielded the conclusion that Carter & Luminet had overestimated the magnitude of the enhancement (Bicknell & Gingold 1983; Laguna *et al.* 1993). Carter & Luminet determined that the central density of the star would scale by a factor of β^3 during the pancake phase, whereas Bicknell & Gingold and Laguna et al. reported a factor of order $\beta^{3/2}$. Unfortunately, we are not aware of any numerical simulations based on finite–difference codes of encounters with larger values of β. These would have helped in determining the true scaling law, as both the analytical and the SPH simulations suffer from a number of limitations. The latter ones are reviewed briefly below.

In Chapter 2, we have given a lengthy discussion of the possible reasons for the discrepancy between the findings of Carter & Luminet and the SPH simulations. To summarize, we believe the reasons to be related to the use of spherically–symmetric kernels and a form of artificial viscosity that generates entropy even in homologous contraction. The latter point is interesting. We first note that the component perpendicular to the orbital plane of the gravitational acceleration due to the

black hole at any radius is proportional to the height above the plane. Thus, the compression of the star along this direction will be nearly homologous as long as the pressure gradients inside the star remain small compared to the gravitational pull of the black hole. During homologous contraction, entropy should be conserved. Unfortunately, the standard form of the SPH artificial viscosity is a function of velocity differences on a pairwise basis, which leads to energy dissipation even in homologous collapse, increasing the entropy of the gas. The gas being on a higher adiabat, pressure gradients are stronger at a given density, and the star bounces at lower density, explaining part of the differences found between the numerical SPH simulations and the analytical results of Carter & Luminet.

Another problem with previous SPH simulations has been the use of spherical kernels. During the pancake phase of the star, the spatial resolution along the direction of collapse can become very poor. We have avoided this problem by pioneering the use of spheroidal kernels, which allow significantly better spatial resolution without requiring the use of more particles. In Chapter 2, we have given a full development of our method of spheroidal kernels.

To emphasize the considerable improvement that spheroidal kernels provide over spherical kernels, consider Figure 3.6. This figure shows a time series of the density in a plane perpendicular to the orbital plane, aligned along the longest axis of the distorted star, for the $\beta = 5$ encounter. The x–axis is along the longest axis of the star, while the z–axis is perpendicular to the orbital plane. Note that the plotting scales used for each axis are not the same. At the time of maximum central density, the star has collapsed by a factor of almost 20 in the z–direction. It would be very difficult to model this collapse using spherical kernels, since if one was to shrink the kernels sufficiently for adequate spatial resolution in the

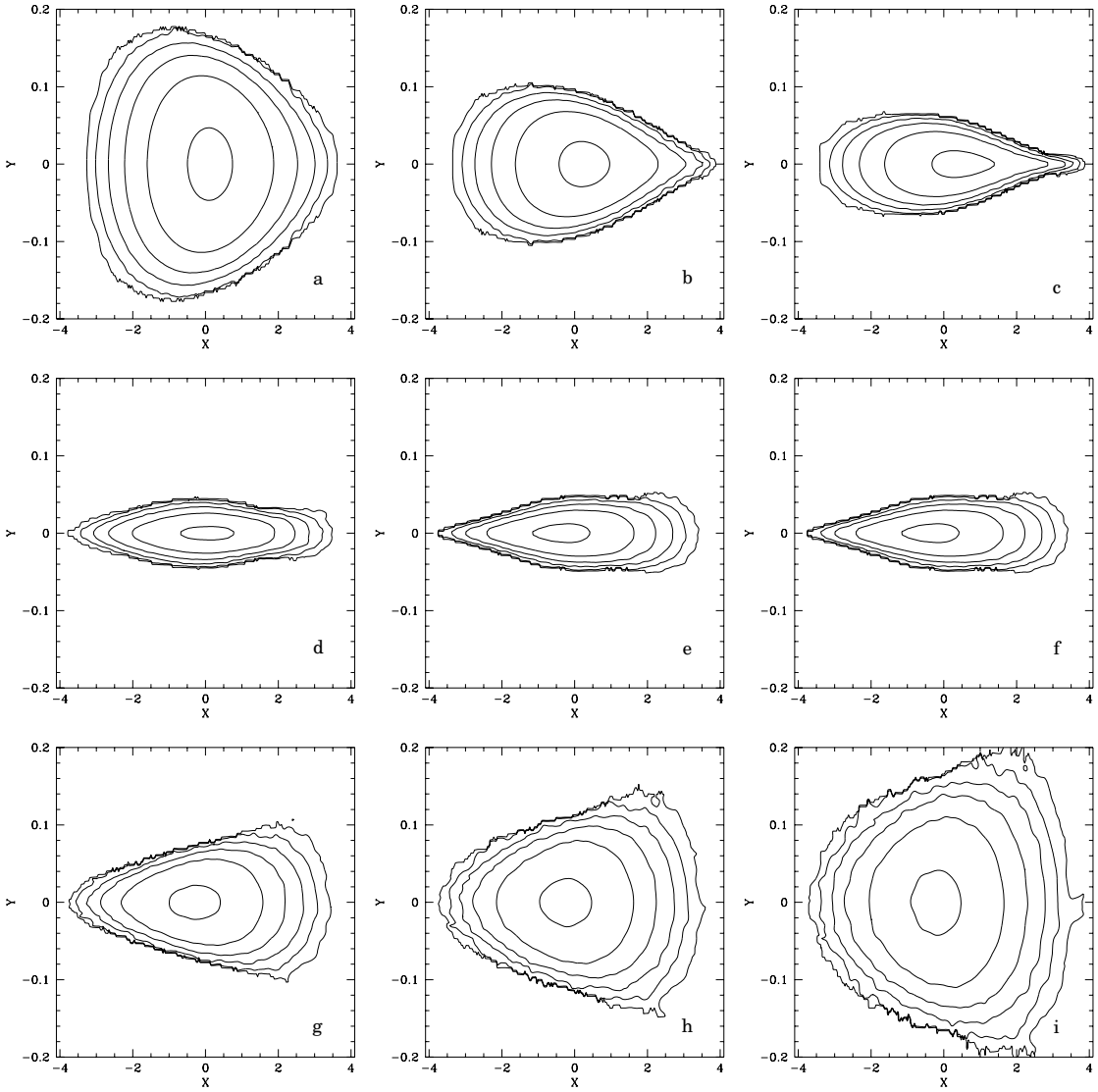

Fig. 3.6.— Time series showing the density in a plane aligned along the longest axis of the star for an $n = 3/2$, $M_{bh} = 10^6$ $M_\odot$, $\beta = 5$ encounter. The collapse of the star is parallel to the z–axis. The time for each frame, relative to the time of maximum central density, are (a) -0.0438122, (b) 0.0246374, (c) -0.0129947, (d) -0.0053219, (e) 0.0000700, (f) 0.0073592, (g) 0.0219012, (h) 0.0324701, and (i) 0.0455705. The innermost contour has a value of (a) 2.43, (b) 3.90, (c) 6.09, (d) 8.37, (e) 9.14, (f) 7.87, (g) 4.27, (h) 2.88, and (i) 1.97. All other contours are smaller than the previous by a factor of 2.

z–direction, particles would not overlap with other particles in the lateral directions with similar values of z. This would mean that the neighbors of a given particle would only be those directly above and below it in the z–direction. With no more sonic contact inside the orbital plane, the problem has been reduced essentially to the calculation of a number of poorly–resolved, one–dimensional problems. With spheroidal kernels, we are able to maintain contact between particles in the plane parallel to the orbital plane until the star has extended itself and formed tails of stripped material. At this point, hydrodynamic forces are negligible because the material has very low density and internal energy.

It is worth pointing out that merely increasing the number of particles but keeping the kernel spherical is not an alternative to the use of spheroidal kernels. First, we note that matching the resolution perpendicular to the orbital plane during the pancake phase of a $\beta = 5$ encounter would require $\sim 3.5 \times 10^5$ spherical particles (Section 2.2.2). However, even if this number is used, the scaling of the spherical kernel will still result in the breakdown of the hydrodynamics parallel to the orbital plane, as particles would be out of sonic contact. This illustrates well the numerical difficulties of these types of simulations which, at first glance, appeared to be well tailored to the SPH technique.

The magnitude of density enhancement for several $M_{bh} = 10^6$ $M_\odot$ models are given in Table 3.4, and shown in Figure 3.7. It should be noted that since our code is based on purely Newtonian mechanics, encounters with $\beta = 10$ in which the star comes within a couple of Schwarzschild radii of the black hole are not meant to represent the dynamics accurately, but were run only for the purpose of determining the density scaling law. The next level of simulation would be to include relativistic effects in our code.

Table 3.4: Magnitude of density enhancement for $n = 3/2$ calculations.

β	ρ_{max}/ρ_0
1.0	1.001
1.5	1.000
2.0	1.182
3.0	2.343
5.0	7.789
10.0	46.892

Another concern in the simulation of very deep encounters, say $\beta = 10$, is again a purely SPH problem. As with all particle methods used in fluid dynamics, it is essential to prevent particles from two colliding streams to penetrate. Pressure gradients and artificial viscosity should prevent such streaming. While this is generally the case, we have observed these problems to increase significantly with increasing β. This can be checked easily by computing how many particles crossed from one side of the orbital plane to the other side during the encounter. While there clearly should be none, we found that in the case of the $\beta = 10$ simulation, 10% of the mass of the star streamed through the orbital plane. Since these problems occur essentially in the outer regions of the star where the typical particle has a smaller number of neighbors, we don't believe the central density enhancement is affected much by this. Fortunately, since the particles which stream are concentrated near the surface of the star, by increasing the number of particles used in the simulation, one should be able to reduce the fraction of the star which streams. We note that the SPH simulations of Laguna *et al.* update the position of particles using a correction term computed from the local mean velocity (Monaghan 1989). While this indeed stops penetration and streaming, it has the disadvantage of no longer conserving total energy when an external force (in our

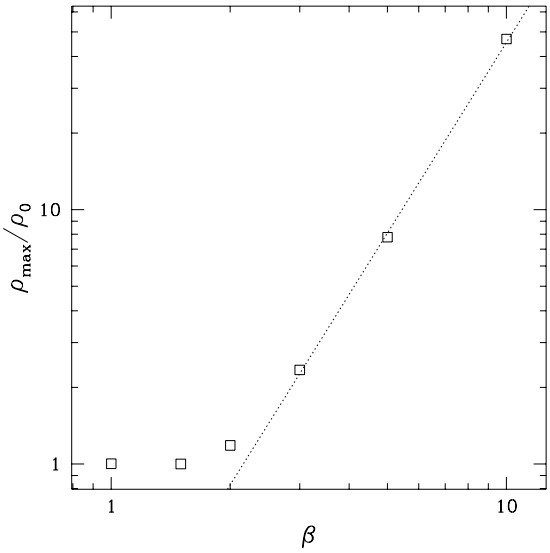

Fig. 3.7.— Central density enhancement as a function of β for $n = 3/2$.

case, the gravitational force of the black hole) is applied; thus, we discard such technique here.

Even with these reservations about our modeling of a $\beta = 10$ encounter, the density enhancement values for $\beta = 3,\ 5,$ and 10 fall nicely along a $\beta^{2.5}$ power law. A more exact fit (shown in Figure 3.7 as a dotted line) gives

$$\frac{\rho_{max}}{\rho_0} = 0.147\ \beta^{2.49}\ . \tag{3.9}$$

Here, ρ_{max} is the maximum density at the center of the star during the entire simulation, and ρ_0 is the initial density at the center of the star. This result is closer to the β^3 power law of Carter & Luminet than previous SPH investigations. One reason for this better agreement is the fact that our modified viscosity term led to very little viscous heating during the collapse of the star. Let us define the entropy S as

$$S = (\gamma - 1) \ln \left\{ \frac{(\gamma - 1)u}{\rho^{(\gamma-1)}} \right\}\ . \tag{3.10}$$

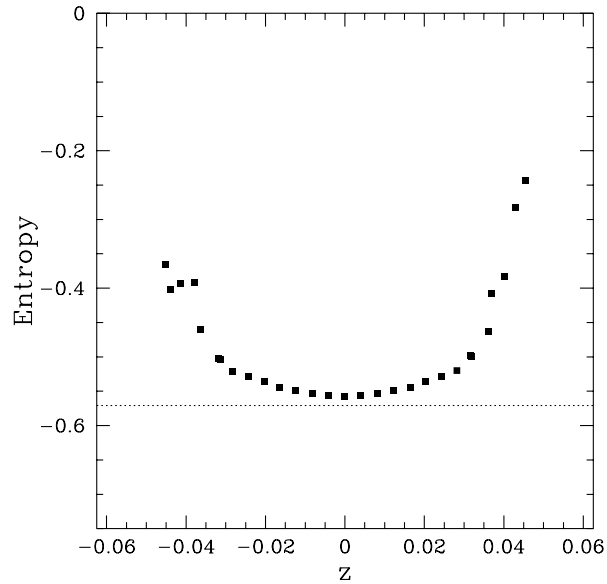

Fig. 3.8.— Entropy shown as a function of height in the collapsing stellar atmosphere in the $\beta = 5$ model with $n = 3/2$ and $M_{bh} = 10^6$ $M_\odot$ models. The curve is at the time of maximum central density.

In Figure 3.8, the entropy of the star is given as a function of height at the time of maximum central density for the $\beta = 5$ model. The values plotted are along a line which passes through the center of mass of the star and is perpendicular to the orbital plane. The dashed line gives the initial (constant) value of entropy throughout the star. The density along the same cut through the star is shown in Figure 3.9. If the star collapses adiabatically, then the entropy should remain constant. The departure of the entropy in the outermost gas from the original value shows this is where shock heating has occurred. The innermost material is halted by the increase in pressure due almost solely to the adiabatic compression of the gas, just as in the models of Carter & Luminet. The shock heating of the outermost material could be the reason we do not observe as much of a density enhancement for a given β as Carter & Luminet.

One of the assumptions of the affine model used by Carter & Luminet is that

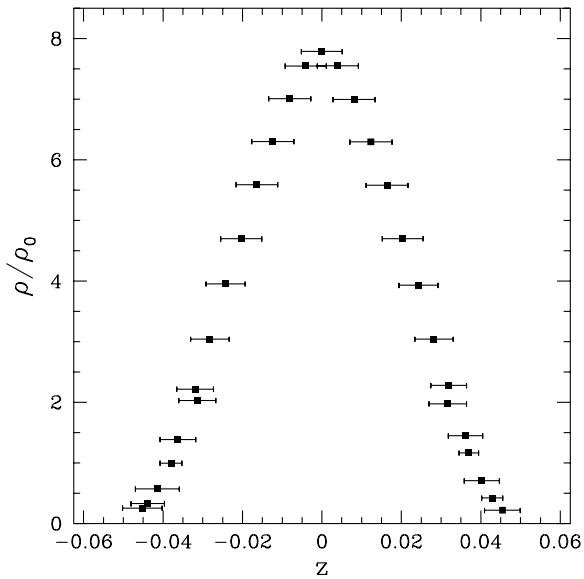

Fig. 3.9.— Density shown as a function of height in the collapsing stellar atmosphere in the $\beta = 5$ model with $n = 3/2$ and $M_{bh} = 10^6$ $M_\odot$ models. The curve is at the time of maximum central density, and is scaled by the initial central density of the star ρ_0. The interval bars show a distance of h_{zz} in each direction.

contours of equal density remain concentric ellipsoids. From Figure 3.6, one can clearly see that this assumption is not true near the time of maximum central density for our $\beta = 5$ encounter. For encounters with $\beta > 5$, the situation becomes even worse. The best way to visualize what these encounters would look like is to imagine pulling a sponge through a very small ring. At the location of the ring, the sponge undergoes maximal compression, and, as one moves away from the ring, the compression decreases. Our departure from the result of Carter & Luminet may be in part due to the breakdown of the affine assumption for these extreme encounters.

Another possible reason for the differences is that in our initial conditions, the gas particles only extend to approximately 86% of the radius of the star to which the model is supposed to correspond. In the initial model, we pack our particles on a hexagonal lattice with a spacing roughly equal to the initial smoothing length

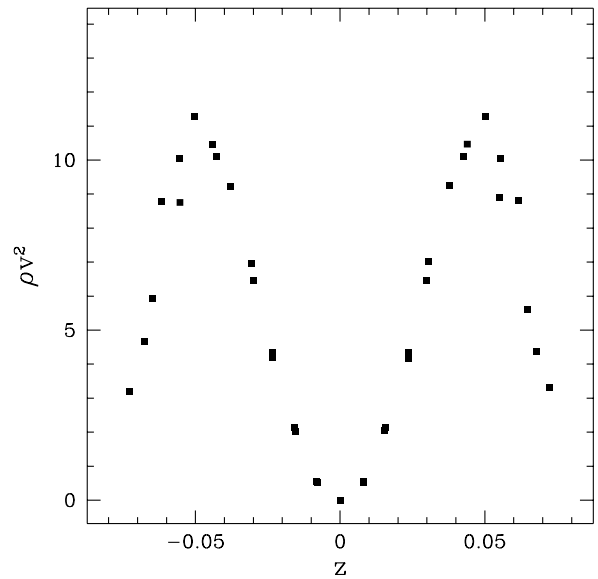

Fig. 3.10.— Ram pressure as a function of height in the collapsing stellar atmosphere for the same $\beta = 5$ model as Figure 3.8. The curve is taken just before the time of maximum central density.

of the particles. For the number of particles used in these simulations (5093), the outermost layer of the hexagon grid is of order 86% of the radius of the actual star. If this gas had actually been present in the simulation, a higher pressure would have been required at the center of the star to halt the collapse of the atmosphere. To assess the importance of the missing outer 14% in radius of the star, we plot in Figure 3.10 the ram pressure ρv^2 just prior to reaching maximum central density in our $\beta = 5$ simulation. We see that the ram pressure reaches a maximum value approximately midway to the surface of the star and falls off rapidly towards the surface. Thus, we believe extending the star to its true radius would lead to a negligible increase in the central density enhancement.

In an attempt to understand the effect of numerics on our solution, a $\beta = 5$ run with 14591 particles was also calculated. The particles now extend to 90% of the desired radius of the star. The increase in the maximum central density, normalized

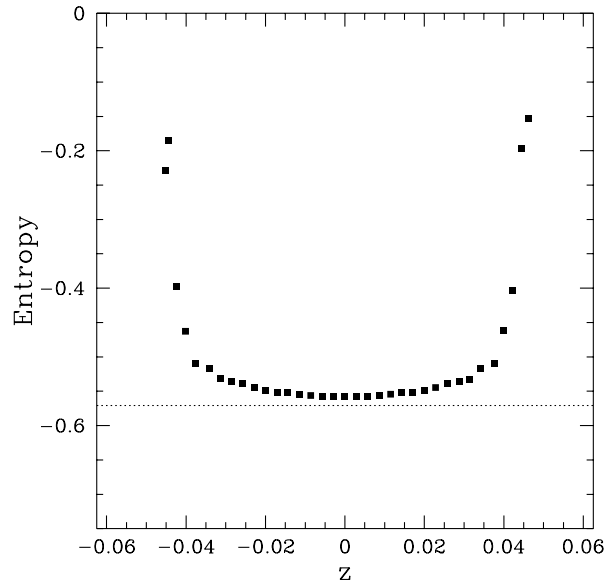

Fig. 3.11.— Similar to Figure 3.8, except that this figure is for a run with 14591 particles instead of 5093.

to the initial center density, was 8.00. This compares favorably to the value of 7.79 from the run with 5093 particles. In Figures 3.11 and 3.12, the run of entropy and density versus z are shown for the calculation with 14591 particles, and should be compared to Figures 3.8 and 3.9, which are for the run with 5093 particles. The principle difference is that the entropy jump near $|z| = 0.04$ is sharper in the case with 14591 particles, most likely due to the improvement in spatial resolution that comes with more particles. Overall, this result shows that the density enhancement for the case of $\beta = 5$ is not significantly more than 8, and that our result is fairly independent of the number of particles used in the calculation.

3.3.3 Tidal Energy Transfer

The emphasis of these calculations has been to model the stripping of material from the star. In the case where material is not stripped from the star, there is

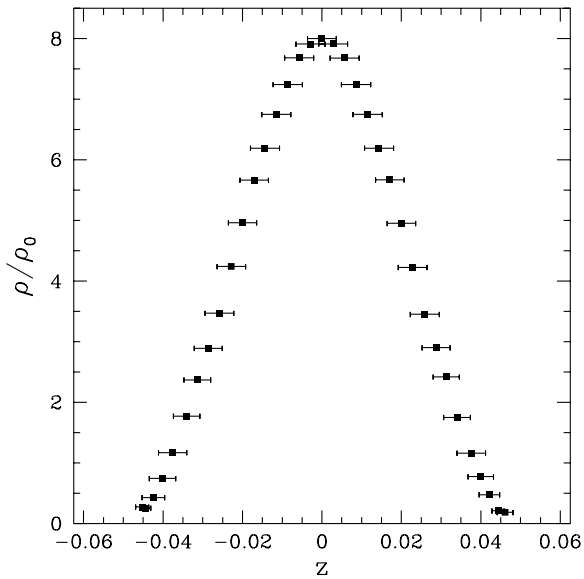

Fig. 3.12.— Similar to Figure 3.9, except that this figure is for a run with 14591 particles instead of 5093.

the possibility that the star will become tidally captured (Fabian *et al.* 1975). The energy required to deform the star reduces the energy of its orbit around the black hole. Since the star was initially in a parabolic orbit, after deformation it will be in an extremely eccentric elliptical orbit with roughly the same closest approach to the black hole. The next encounter with the black hole will possibly further deform the star, reducing the energy of its orbit more. Semi–analytic calculations of the work done on the star have been computed (Press & Teukolsky 1977; Lee & Ostriker 1986). Additionally, three–dimensional hydrodynamic calculations for various polytropic stars using a grid–based code are now available (Khokhlov *et al.* 1993). In Figure 3.13, we compare our values of $T_2(\eta)$ to those given in Khokhlov *et al.* and Lee & Ostriker. The quantity $T_2(\eta)$ is defined (Press & Teukolsky 1977) to be

$$T_2(\eta) = \eta^4 \Delta E \ , \tag{3.11}$$

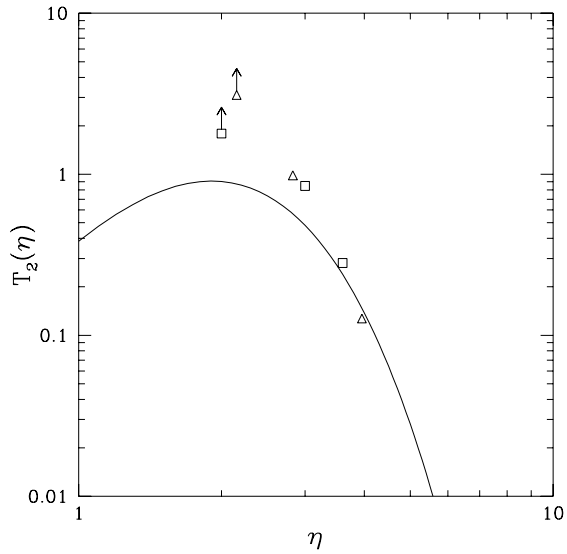

Fig. 3.13.— Energy transfer to the star for $n = 3/2$ models. The open triangles are the results from this work, the open squares are from Khokhlov *et al.* (1993), and the solid curve is from Lee & Ostriker (1986).

where ΔE is the quantity of energy transferred to the star from its orbital energy during the encounter. Our result for $\eta = 3.95$ falls near the result expected from linear theory, and is where the results of Khokhlov *et al.* appear to indicate the departure from linear theory should start. Our value for $\eta = 2.83$ also appears to be consistent with the results of Khokhlov *et al.* The points near $\eta = 2$ are shown as lower limits, since, at the end of the simulation, the value of $T_2(\eta)$ was still increasing. In these cases, a small amount of material was stripped from the star. That both SPH and the grid–based FCT (flux corrected transport) method employed by Khokhlov *et al.* agree so well is reassuring, since the two methods use radically different approaches to solve the equations of hydrodynamics.

The amount of energy pumped into the star in these cases is of order 1% of the binding energy of the star. We found that the error in total energy, however, was about 3% of the binding energy of the star for these cases. The fact that our

results agree so well with Khokhlov *et al.* is further evidence that the error in total energy in our calculations is dominated by errors in the position of the center of mass of the star, as described earlier in this paper. These errors do not appear to significantly affect the modeling of tidal forces acting on the star.

3.4 Results for $n = 3$

In order to examine how mass loss was affected by the internal structure of the star, we also performed a number of simulations in which the star was approximated by an $n = 3$ polytrope. Unlike the $n = 3/2$ model from the previous section, the star in this case does not have constant entropy throughout, since $\gamma \neq (1 + 1/n)$. While the initial structure of the star corresponded to an $n = 3$ polytrope, the evolution was computed assuming a matter–dominated gas for which we set $\gamma = 5/3$. To allow direct comparison with the results of the $n = 3/2$ simulations, we kept the radius and the total mass fixed at solar values. Thus, as shown in Figure 3.14, the central density of the $n = 3$ star is a factor of 8 greater than the central density of the $n = 3/2$ star. The mass inside of a given radius r is plotted in Figure 3.15. The steps in this figure at small R are due to the fact that there are no particles in the region $0 < R < 0.1$, meaning the cumulative mass stays constant over that range. The half–mass radius for the $n = 3/2$ star is at approximately $r = 0.5$, while for the $n = 3$ star, the half–mass radius occurs at $r = 0.27$. These characteristics make our $n = 3$ model more representative of stars of solar mass or greater. But it should be noted that our $n = 3$ model will primarily be used in this preliminary survey of the tidal disruption process to compare with the $n = 3/2$ model in order to probe the dependence of mass loss on the density profile of the star. The next stage will be to use realistic stellar models

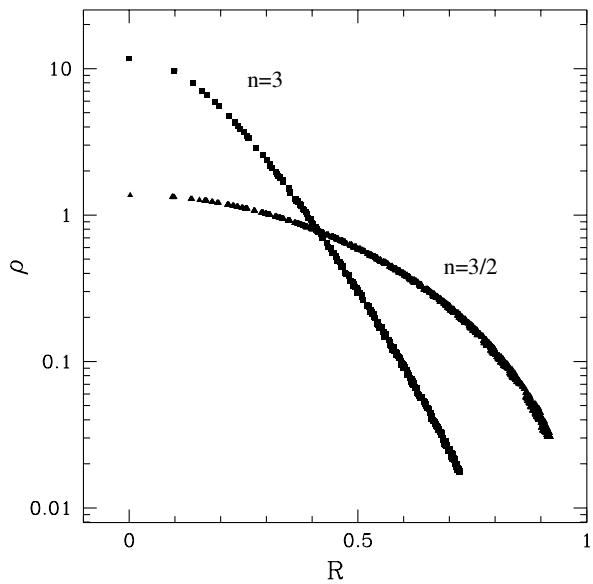

Fig. 3.14.— Comparison of the density profiles of the $n = 3/2$ (triangles) and $n = 3$ (squares) models. Code units are used for both axes of this figure.

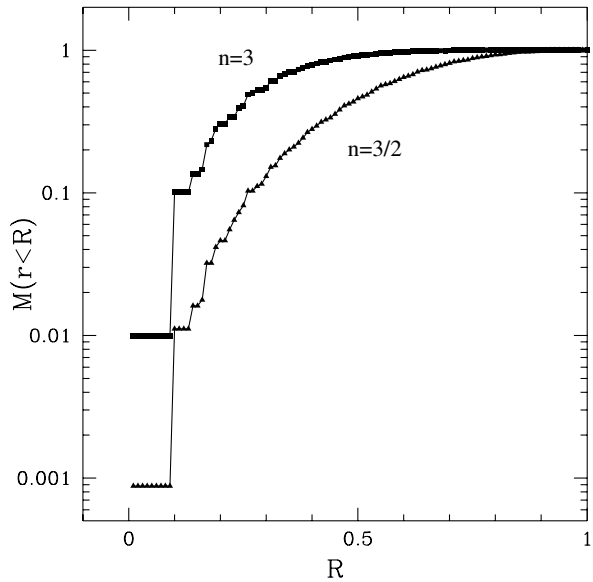

Fig. 3.15.— Comparison of the cumulative mass profiles of the $n = 3/2$ (triangles) and $n = 3$ (squares) models. Code units are used for both axes of this figure.

Table 3.5: Mass fractions for $n = 3$ and $M_{bh} = 10^6$ $M_\odot$ as a function of β.

β	M_{star}	M_{bh}	M_{free}
0.60	1.000	0.000	0.000
0.75	0.998	0.001	0.001
0.90	0.983	0.009	0.008
1.00	0.955	0.023	0.022
1.25	0.807	0.097	0.096
1.50	0.595	0.205	0.200
2.00	0.216	0.379	0.405
3.00	0.000	0.499	0.501
5.00	0.000	0.499	0.501

for these calculations. Because of the overall similarity of the $n = 3$ and $n = 3/2$ results, we will concentrate on only the differences between the two cases. The star undergoes a similar deformation in either case, and, for high enough values of β the star will flatten into a pancake–like shape. The most significant difference is that the binding energy of the $n = 3$ polytrope is larger than the $n = 3/2$ polytrope, so it requires a deeper plunge to completely disrupt the star in the $n = 3$ case. The fractions of the star which goes into the three components introduced above are given in Table 3.5 for a black hole mass of $M_{bh} = 10^6$ $M_\odot$. The values for a black hole mass of 10^4 $M_\odot$ are nearly identical, as in the case for $n = 3/2$, so they are not given. In Figure 3.16, the mass fractions are plotted for both the $n = 3$ and $n = 3/2$ cases. As anticipated, the star must come closer to the black hole in the $n = 3$ case in order for it to be completely disrupted. Another interesting difference between the $n = 3/2$ and $n = 3$ runs is the width of the specific energy distribution of the debris. For a given value of β, the $n = 3$ distribution is wider. The specific energy distribution and period distribution for $\beta = 3$, $n = 3$ is given in Figure

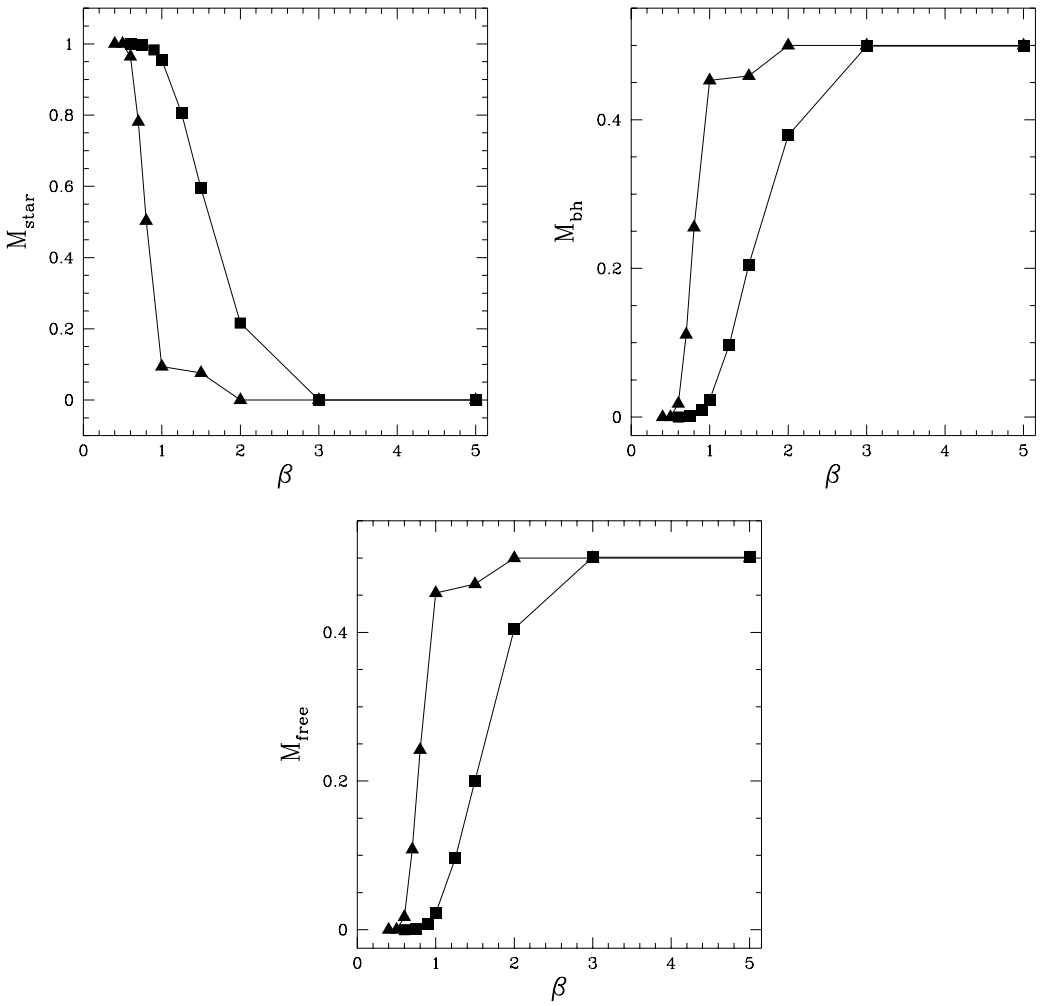

Fig. 3.16.— The stripped mass fractions for both the $n = 3/2$ and $n = 3$ polytropes. The black hole mass in both cases is 10^6 $M_\odot$. The filled triangles are the $n = 3/2$ results, while the filled squares are the results for $n = 3$.

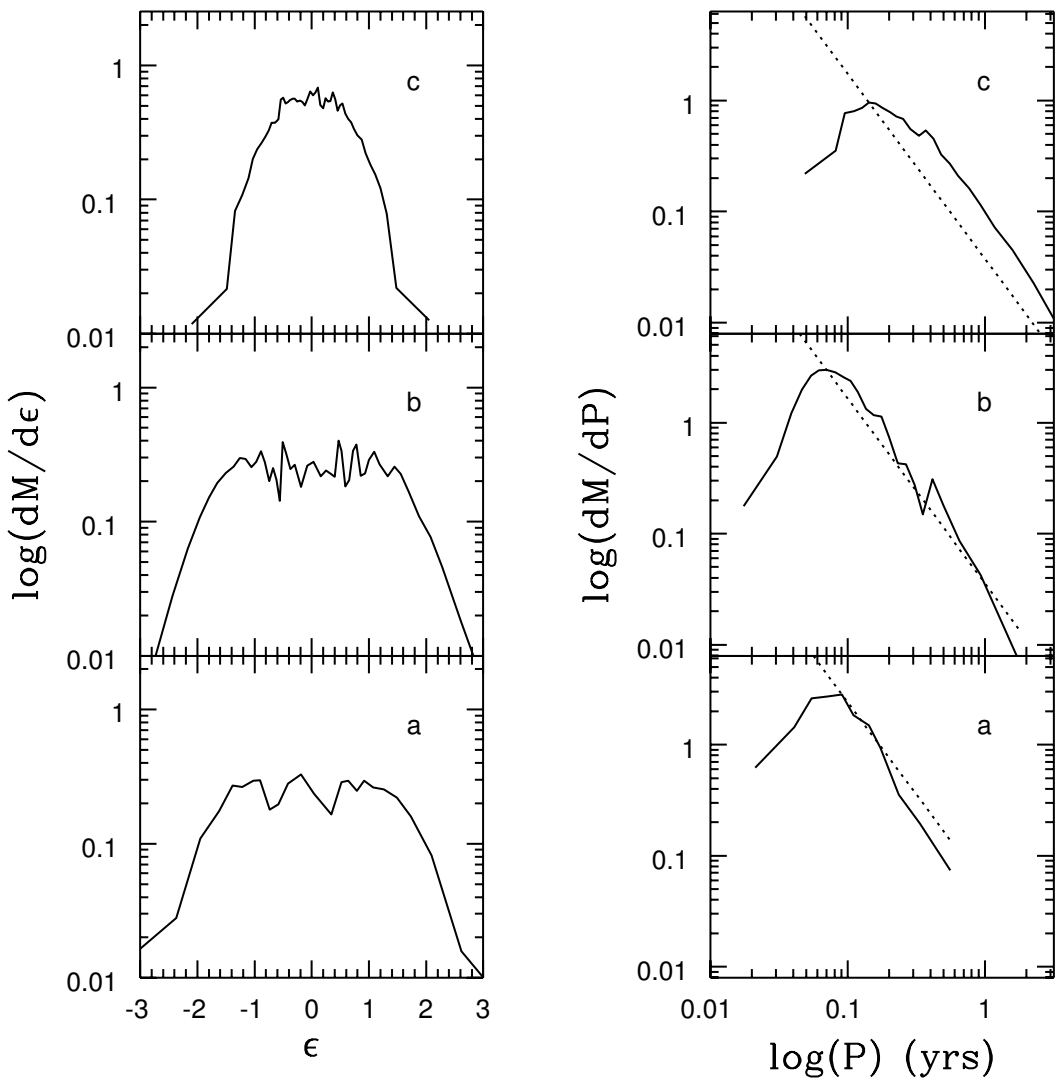

Fig. 3.17.— Energy and period distribution of stripped material for various $\beta = 3$ encounters with a black hole of 10^6 $M_\odot$: a) $n = 3$ and 2351 particles, b) $n = 3$ and 4961 particles, and c) $n = 3/2$ and 5093 particles.

3.17. There are actually two different $\beta = 3$ runs shown, one computed with 2351 particles and the other with 4961 particles. Also plotted is the $\eta = 3$, $n = 3/2$ run originally shown in Figure 3.4. Note that the two $n = 3$ runs agree well, with the 4961 particle run giving better statistics. In addition, the 4961 particle run gives a better treatment of the outer layers of the star. This is evidenced by the extension of the period distribution derived from 4961 particle to longer periods than seen from the 2351 particle run. Another feature to note is that, in the case of $n = 3$, the material returns to the vicinity of the black hole on a time scale that is about half that of the $n = 3/2$ case. However, due to the current uncertainty of what happens to the debris once it returns to the black hole (see Rees 1990 for some possibilities), the difference in time scales for $n = 3/2$ and $n = 3$ may not be that significant in terms of what a tidal disruption event would look like to an observer. Therefore, we believe that the most significant difference between the two models lies in the fact that the $n = 3$ model would require a closer encounter than the $n = 3/2$ model to lose the same amount of mass.

3.5 Conclusions

Our models agree well with earlier numerical simulations, either SPH or finite–difference, for mild encounters with $\beta \sim 1$. For encounters with $\beta \geq 5$, however, we differ significantly with previous SPH calculations that are the only calculations currently available in this regime. We believe that these differences stem from the use of spherical kernels, which do not provide adequate spatial resolution during the strong pancake phases, and by an artificial viscosity term which led to extraneous shock heating, causing the star to bounce at too low a central density. We are able to circumvent these difficulties by using spheroidal

kernels and a modified artificial viscosity.

While our results still do not recover the $\rho/\rho_0 \propto \beta^3$ scaling of Carter & Luminet, we obtain a much steeper dependence of central density increase with closest approach than all previous SPH simulations. We obtain a central density scaling of $\beta^{2.5}$, which is interestingly close to the analytic value. It is not clear if the differences between the two values reside in further limitations of the numerical methods (truncation of the polytrope, Newtonian mechanics even in deep encounters, etc.) or to assumptions behind the analytic model (elliptical density profiles, no shock dissipation, etc.). However, even though there might be still some uncertainty with the outcome of very close encounters, they are infrequent, and their overall importance on the feeding of the black hole is correspondingly reduced.

The main focus of this work has been to derive the amount of mass lost from a star for a given strength encounter with a black hole. We find, as expected, that the amount of mass lost for a given strength encounter (measured by β) is independent of the mass of the black hole over a range of 10^4 to 10^6 $M_\odot$. Also as expected, the more centrally concentrated $n = 3$ polytrope requires a stronger encounter to be completely disrupted than the $n = 3/2$ polytrope. The mass lost as a function of β, presented in Tables 3.2 and 3.5, will allow the improvement of estimates of the rate at which an AGN can be fed by the tidal disruption of stars. This will be the subject of the next chapter.

Chapter 4

THE TIDAL DISRUPTION OF STARS IN GALACTIC NUCLEI

There is kinematic evidence that an $\sim 10^6$ $M_\odot$ black hole exists at the center of the Milky Way (Serabyn & Lacy 1985). Yet, our galactic center does not exhibit any signs of particular activity such as those normally expected from accreting black holes of this size (high energy photons, short time scale luminosity variations, etc). The usual explanation for this lack of activity is to assume the black hole to be starved of fuel. While it is conceptually possible to envision a central region devoid of "free" gas, the tidal disruption of stars entering the black hole's Roche limit after having diffused onto nearly radial orbits is unavoidable and have been computed to occur once every 10^4 years in the case of a 10^6 $M_\odot$ black hole (Cohn 1978). Such encounters necessarily supply the black hole with a significant quantity of gas, which should give rise to detectable activity lasting as long as the accretion process. Our galactic center should therefore experience a period of relatively intense activity, followed by an extended period of quiescence which might be the

dominant state if the accretion of the tidally–captured debris occurs on time scales that are short compared to successive tidal disruptions.

This scenario is not restricted to the Milky Way alone, as the case can be made that most bright galaxies have a central black hole with a mass of 10^6 solar masses or more (Boyle *et al.* 1987; Rees 1990). And yet, again these galaxies do not exhibit any signs of particular activity, earning the label "dead quasars" from Rees (1990). While these galaxies might be starved of "free" gas, they cannot avoid the tidal disruption of stars on nearly radial orbits. Thus, we conclude that these galaxies must be observed currently in the quiescent state between successive disruption, their activity level increasing significantly for a short period of time after each disruption. Since such events are expected to produce an X–ray flare for a time scale of a few months to a year (Rees 1988), their systematic detection in the center of galaxies would provide strong evidence for the existence of massive black holes in most galaxies. A number of observations claiming the detection of such events have been published, and we will review them in Section 4.4.

The study of the feeding of a massive black hole by the tidal disruption of stars requires the understanding of several important physical processes. These include not only the physics of the disruption process itself and the determination of the amount of mass bound to the black hole, but also the determination of the frequency at which such encounters take place, as well as the details of the final accretion by the black hole of the captured debris and the expected observational consequences.

Since until recently numerical simulations of the actual tidal disruption of stars venturing too close to the black hole were not possible, previous investigations (e.g., Duncan & Shapiro 1983; Murphy *et al.* 1991) relied on simple assumptions.

In particular, it has been assumed that a star is disrupted if it passes closer than a distance r_t from the black hole (which we will refer to as the hard–sphere assumption). Once disrupted, the entire mass of the star is accreted by the black hole. In this work, we will define the radius r_t as

$$\begin{aligned} r_t &= \left\{\frac{M_{bh}}{M_\star}\right\}^{1/3} R_\star \\ &= 100\,\mathrm{R}_\odot \left(\frac{M_{bh}}{10^6\ \mathrm{M}_\odot}\right)^{1/3} \left(\frac{\mathrm{M}_\odot}{M_\star}\right)^{1/3} \left(\frac{R_\star}{\mathrm{R}_\odot}\right) , \end{aligned} \tag{4.1}$$

where M_{bh} is the mass of the black hole, and $M_\star$ and $R_\star$ are the stellar mass and radius of the star, respectively. Our definition of r_t is comparable but not exactly identical to the Roche radius. Clearly, the disruption process is more complicated than assumed in the hard–sphere model. For very distant encounters, the star will merely deform and not lose material. For somewhat closer encounters, the star will begin to lose the outer layers of its atmosphere, but the remainder of the star will remain intact. The star will not experience significant mass loss until the energy pumped into the star by tidal forces is comparable to the binding energy of the star. In the limit of very strong encounters, the star will be completely disrupted and half of the debris will be bound to the black hole (Lacy *et al.* 1982). This limit is a result of the process by which the star is disrupted. In a strong encounter, the star is first stretched out into a cigar–like shape. The tidally–induced torque on the star then causes the star to spin–up and disrupt. Two tails of roughly equal mass are thrown out, one bound to the black hole and the other unbound. In order to explore this spectrum of encounters, we seek to compute the amount of mass stripped from a star as a function of its impact parameter b with the black hole. For weak, distant encounters, one can use a linear treatment of the problem to compute how much energy is pumped into the star (Press & Teukolsky 1977). The linear treatment, however, becomes invalid for the stronger encounters where

mass is stripped from the star and numerical simulations become necessary to understand these cases.

Smoothed Particle Hydrodynamics (SPH) is a robust, efficient computational technique that allows three–dimensional problems to be solved on modern–day workstations. In Chapter 2, we described the SPH method we have developed in order to model the tidal disruption of stars. It differs from the traditional SPH method by utilizing spheroidal instead of spherical kernels. In addition, our SPH method employs a specially–tailored artificial viscosity in order to model shock heating during the disruption of the star more accurately than is possible using the traditional SPH method. For simplicity, we have modeled stars as polytropes, although, in principle, it should be possible to use realistic stellar models. In Chapter 3, we have presented a catalog of results for the disruption of solar mass polytropes of indices $n = 3/2$ and $n = 3$ by a 10^6 solar mass black hole. Among the results presented in Chapter 3 is the desired information about the mass lost by the star as a function of its impact parameter b.

In this chapter, we shall estimate the feeding rate of a black hole by the tidal disruption of stars by using both the hard–sphere assumption and the results obtained from our simulations. We shall compare both estimates, which will provide a sense of uncertainty still affecting these rates. However, in order to be able to determine these rates, we need to first define a model for the stellar system in which the black hole is embedded. We shall use a King model, otherwise known as a truncated isothermal sphere, to represent this stellar cluster. Once the stellar cluster model is given, we will employ loss–cone theory (Frank & Rees 1976) to calculate feeding rates for two different assumptions of tidal disruption. After comparing these two estimates, we shall review the expected observables of

a tidally–disrupted star. Finally, we will consider recent claims of observational detections of tidally–disrupted stars in other galaxies.

4.1 Tidal Disruption of Stars in a Truncated Isothermal Sphere

4.1.1 The Stellar Cluster Model

The prevailing model for an Active Galactic Nucleus (AGN) places a massive black hole at its center in the actual nucleus of a galaxy. The black hole has grown to its current size by accreting material originating from several sources. A stellar collision can lead to the ejection of a fair fraction of the total mass of the two stars. Winds from evolved stars will be another source of free gas. Finally, debris stripped from tidally–disrupted stars will also be available to feed the central black hole. The stellar cluster surrounding the black hole is in turn affected by the loss of stars to the black hole. In addition, the orbits of stars which pass in the vicinity of the black hole are modified by the considerable gravitational influence of the black hole. The mutual interaction between a stellar distribution and a massive black hole have been studied extensively (see Shapiro 1985 for a comprehensive review). In summary, the presence of the black hole will cause a high density cusp to form at the center of the cluster. This cusp extends out to a distance of approximately

$$\begin{aligned} r_a &= \frac{GM_{bh}}{\sigma^2} \\ &= 0.43 \left(\frac{M_{bh}}{10^6 \ \mathrm{M}_\odot} \right) \left(\frac{\sigma}{100 \ \mathrm{km \ s^{-1}}} \right)^{-2} \ \mathrm{pc} \ , \end{aligned} \tag{4.2}$$

where M_{bh} is the mass of the black hole and σ^2 is the velocity dispersion of the cluster. Beyond this distance, the influence of the black hole is small, and the distribution function of the stellar orbits is close to that of an isothermal sphere.

Previous studies have shown that a minority of the stars disrupted will come from the central cusp (e.g., Duncan & Shapiro 1983). It is therefore acceptable to model the stellar distribution using a truncated isothermal sphere, also known as a King model (King 1966), and leave the central cusp out of the problem. Having left out a possible source for tidal disruptions, our results should then be viewed as providing a lower limit to the disruption rate. The simplicity of the King model will allow us to concentrate on the impact of using our hydrodynamic results instead of the hard–sphere assumption used in previous work. A future improvement to this work would be to combine a Fokker-Planck code with our hydrodynamic results in order to grow self–consistently a black hole inside of a star cluster up to the present. In this current study, we restrict our focus to the effect of hydrodynamics on the expected fueling rate for the black hole.

The formalism we will use follows that of Binney & Tremaine (1987). The King distribution function (DF) is a truncated isothermal sphere, meaning that there are no stars with an energy greater than a threshold value E_0, with $E_0 < 0$. All stars will have the same mass $M_\star$. The energy per unit mass of a star is given by

$$E = \frac{1}{2}v^2 + \Phi(r) \ . \tag{4.3}$$

The quantity $\Phi(r)$ is the self–potential of the star cluster, and is determined by solving Poisson's equation,

$$\nabla^2\Phi(r) = 4\pi G\rho(r) \ , \tag{4.4}$$

where $\rho(r)$ is the stellar density measured in units of mass per unit volume. A useful change of variables is to choose

$$\begin{aligned} \epsilon &\equiv -E + \Phi_0, \\ \Psi &\equiv -\Phi + \Phi_0. \end{aligned} \tag{4.5}$$

Because it differs from Φ by only the constant Φ_0, the potential $\Psi(r)$ also satisfies the Poisson equation. The outer boundary condition on Ψ is $\Psi(r_o) = 0$, where r_o is the radius at which the stellar density ρ drops to zero. The inner boundary $\Psi(0)$ is traditionally given in units of σ^2, where σ is the one–dimensional velocity dispersion at the center of the cluster. The value of Φ_0 is chosen so that the King DF $f_K = 0$ for $\epsilon \leq 0$. Then the King DF is given by

$$f_K(\epsilon) = \begin{cases} \rho_1 (2\pi\sigma^2)^{-3/2} \left[\exp(\epsilon/\sigma^2) - 1\right], & \epsilon > 0 \ , \\ 0, & \epsilon \leq 0 \ , \end{cases} \tag{4.6}$$

where ρ_1 is related to the central stellar density ρ_0 by a constant factor, and serves as a normalization factor for f_K. Given f_K and Poisson's equation, the mass and radius of the stellar cluster are determined solely by the choice of ρ_0, σ^2, and $\Psi(0)/\sigma^2$. The core radius R_c, inside of which the stellar density is fairly constant, for the cluster can be defined as

$$\begin{aligned} R_c &= \left(\frac{9\sigma^2}{4\pi G M_\star n_0}\right)^{1/2} \\ &= 1.3 \left(\frac{\sigma}{100 \text{ km s}^{-1}}\right) \left(\frac{\mathrm{M}_\odot}{M_\star}\right)^{1/2} \left(\frac{10^6 \text{ pc}^{-3}}{n_0}\right)^{1/2} \text{ pc} \ , \end{aligned} \tag{4.7}$$

where $M_\star$ is the mass of a star and n_0 is the central number density of stars, related to the central mass density ρ_0 by $n_0 = \rho_0/M_\star$.

In this section, the stellar cluster referred to has a core radius R_c of order 1 pc for expected values of $\rho_0 \sim 10^6$ $\mathrm{M}_\odot$ pc^{-3}, $\sigma \sim 100$ km s^{-1}, and $\Psi(0)/\sigma^2 \sim 8$. Within our own galactic nucleus, studies of the dynamics of gas and stars are consistent with a cluster having a core radius of ~ 1 pc (e.g., Haller *et al.* 1995). Otherwise, unfortunately, only in a few nearby galaxies is it even plausible to observe a central cluster. The observation is further complicated by the presence of a central black hole, which will cause the light profile to be steeper than that of just a stellar cluster alone. For a proper understanding, one must fit the observations with a

model including both a black hole and a stellar cluster. For example, a recent *HST* observation of M32 (Lauer *et al.* 1992b) was unable to resolve a central core. However, when the observations were compared to calculations by Young (1980) of the growth of a black hole in an initially isothermal core, it was found that a central black hole of mass 2.8×10^6 $M_\odot$ produced the best fit. In this model, the initial isothermal stellar cluster had a core radius of 3 pc and a central density of 8.4×10^4 $M_\odot$ pc^{-3}. Similar observations of M31 (Lauer *et al.* 1993), M87 (Lauer *et al.* 1992a), and NGC 7457 (Lauer *et al.* 1991) were all consistent with the presence of a compact core at the center of each galaxy. In the case of M31, the situation is even more complicated, as evidence for a double nucleus was found. Presumably, these galaxies are not rare examples that just happen to be near the Milky Way, and dense stellar cores are present in most, if not all, normal galaxies.

4.1.2 Loss–Cone Theory

We will now examine the following problem: given the stellar cluster model from Section 4.1.1, at what rate do stars pass close enough to the black hole to be disrupted? A summary of previous work on this problem can be found in Shapiro (1985). Past studies have found that the the majority of stars which are disrupted by a black hole are not bound to the black hole and are on extremely elongated orbits which take them inside the Roche limit of the black hole (e.g., Duncan & Shapiro 1983). Let each star be described by its specific energy E and specific angular momentum J. For conciseness, however, in this section E will be referred to as the "energy" of the star, and J will be referred to as the "angular momentum" of the star. The term "loss cone" describes the portion of (E, J) phase space from which stars will be disrupted. The loss–cone concept was first applied

to the tidal disruption of stars by Frank & Rees (1976). For stars not bound to the black hole, the loss cone is actually more of a loss column, as pointed out by Cohn & Kulsrud (1978). This is because an unbound star will be disrupted if its angular momentum J is less than a constant value J_{min}, independent of its energy E. As stars are removed from the loss cone by disruptions, new stars are scattered into the loss cone by distant encounters with other stars. Let $j_2(E)$ be the r.m.s. angular momentum transferred, per orbital period, to a star through encounters with other stars. Now if $j_2(E) > J_{min}$, then stars will refill the loss cone at the energy E as fast as it is depleted, in which case the loss cone is said to be full. If $j_2(E) < J_{min}$ then stars slowly diffuse into the loss cone, which is then said to be empty. The transition between a full and an empty loss cone occurs at the energy E_{crit} given by Duncan & Shapiro (1983)

$$\frac{j_2^2(E_{crit})}{J_{min}^2} = \ln\left[\frac{J_{max}(E_{crit})}{J_{min}}\right], \tag{4.8}$$

where $J_{max}(E_{crit})$ is the angular momentum of a star in a circular orbit of energy E_{crit}. Stars with $E < E_{crit}$ have an empty loss cone, while stars with $E > E_{crit}$ have a full loss cone. We will only consider the contribution from the stars with $E > E_{crit}$. To properly handle the stars coming from an empty loss cone requires the numerical solution of the Fokker–Planck equation. Fortunately, the contribution from stars with $E > E_{crit}$ dominate for the black hole masses and stellar cluster parameters which are the focus of this study. However, since we are neglecting the contribution from stars with $E < E_{crit}$, we will tend to underestimate the total disruption rate for the cluster.

We will now, given the King DF, find the rate at which stars of a given impact parameter b pass the black hole. To do so, we will follow the treatment of the loss cone by Shapiro & Marchant (1978). A star of a given energy E will have an

impact parameter b if its angular momentum is given by

$$J^2_{capture}(b) = \{2(E + GM_{bh}/b)\}\, b^2 \;\simeq\; 2GM_{bh}b \;, \tag{4.9}$$

where M_{bh} is the mass of the black hole. The latter approximation is valid because E will be of order $\sigma^2 = 10^{14}$ ergs/gm, while GM_{bh}/b will be of order 10^{19} ergs/gm for a 10^6 $M_\odot$ black hole and $b = 100$ $R_\odot$, the Roche radius for a solar mass star. In other words, the velocity gained by a soon–to–be–disrupted star as it falls into the deep potential well of the black hole is substantially larger than the typical velocity of that same star far from the black hole.

It can be shown (Shapiro & Marchant 1978) that the number of stars $N(E, J)$ with an energy between E and $E + dE$, and an angular momentum between J and $J + dJ$, is given by

$$N(E, J) = 8\pi^2 f_K(E) P(E, J)\; J\; dJ\; dE \;, \tag{4.10}$$

where $f_K(E)$ is the King DF divided by the mass of the star to give a number density instead of a mass density. The quantity $P(E, J)$ is the period of a star with energy E and angular momentum J. For a given value of E and J, there are two turning points in the orbit of the star, r_+ and r_-. We are interested in the latter. In one orbital period $P(E, J)$, all $N(E, J)$ stars will have had time to pass the black hole at a distance of r_- once. Therefore, the rate $F(E, J)$ at which stars of energy E and angular momentum J pass by the radius r_- is just $N(E, J)/P(E, J)$, or

$$F(E, J) = 8\pi^2\, f_K(E)\; J\; dJ\; dE \;. \tag{4.11}$$

Note that $F(E, J)$ has the dimensions of stars per unit time. A star will have an impact parameter less than a given value b_0 if its angular momentum is less than $J_{capture}(b_0)$. Therefore, the rate $F(E, b < b_0)$ at which stars between energies E and

$E + dE$ and an impact parameter less than b_0 pass through pericenter is given by integrating $F(E, J)$ over J from 0 to $J_{capture}$. Since f_K is only a function of E, the resulting integral is trivial and $F(E, b < b_0)$ is given by

$$F(E, b < b_0) = 8\pi^2 G M_{bh} b_0 f_K(E)\ dE\ . \tag{4.12}$$

The quantity we seek is the total encounter rate of stars with an impact parameter less than b_0, which can be achieved by integrating $F(E, b < b_0)$ over E. One integration limit will be $E = \Phi_0$, the energy of a star just bound to the cluster. The other integration limit will be E_{crit}, the energy at which the loss cone goes from full to empty. We will neglect the contribution from where the loss cone is empty because a proper treatment requires the solution of the Fokker–Planck equation. In doing so, we will underestimate the true rate, but, for the cluster parameters we will consider, the loss cone is full throughout the majority of the central cluster, and so this approximation will be adequate. To determine E_{crit}, we must solve equation (4.8). We will make use of the expression for $j_2^2(E)$ given by Duncan & Shapiro (1983). For J_{min}, we use a value of $(2GM_{bh}r_t)^{1/2}$, since, as we will see, for impact parameters larger than r_t, the amount of mass stripped from the star drops quickly. Therefore, the edge of the loss cone, which occurs at an angular momentum where stars are just disrupted, will be at an angular momentum close to J_{min}. Once we know E_{crit}, we can determine the total rate of encounters with an impact parameter less than b_0 by integrating over the applicable range of energy

$$F(b < b_0) = 8\pi^2 G M_{bh} b_0 \int_{\Phi_0}^{E_{crit}} f_K(E)\ dE\ . \tag{4.13}$$

The differential encounter rate is given by dF/db_0. This turns out to be constant, and will be called θ_0

$$\theta_0 = 8\pi^2 G M_{bh} \int_{\Phi_0}^{E_{crit}} f_K(E)\ dE\ . \tag{4.14}$$

The dimensions of θ_0 merit some explanation. The quantity $F(b)$ is the rate at which encounters with an impact parameter of b or less occur. The derivative of $F(b)$ is the constant quantity θ_0. The rate at which stars pass between a distance of b and $b + db$ is given by $\theta_0\ db$, and θ_0 has the dimensions of stars per unit time per unit length.

4.1.3 Including the Hydrodynamic Details of Tidal Disruption

We must now turn to our SPH results in order to convert from the differential encounter rate θ_0 to the differential mass stripping rate. Consider a star which encounters the black hole with an impact parameter b. Let $S(b)$ be the fraction of the mass stripped from the star that will end up bound to the black hole. The function $S(b)$ has been derived from our SPH simulations of an $n = 3/2$ polytrope with a mass of 1 $M_\odot$ and a radius of 1 $R_\odot$. These results are shown in Figure 4.1. An $n = 3/2$ polytrope has a density profile similar to that of low mass ($M \sim 0.4$ $M_\odot$ or less) stars which dominate the present day mass function (PDMF) of the solar neighborhood (Rana 1987). By using the $n = 3/2$ polytrope results, we are assuming that the PDMF of the stellar cluster surrounding the black hole is similar to that of the solar neighborhood. This assumption will suffice for the current calculation, as we want to keep our stellar cluster model simple in order to more easily judge the affect of using our SPH derived $S(b)$ instead of the hard–sphere assumption used in previous work. For the sake of comparison with the SPH derived $S(b)$ in Figure 4.1, the hard–sphere assumption can be stated mathematically as

$$S_{HS}(b) = \begin{cases} 1, & b \leq r_t \ , \\ 0, & b > r_t \ . \end{cases} \tag{4.15}$$

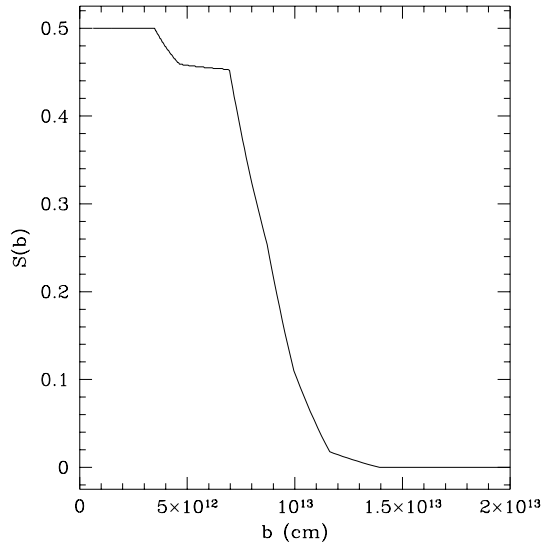

Fig. 4.1.— Fraction of star which is stripped and bound to the black hole after an encounter with an impact parameter of b. This figure is for the case of a 1 $M_\odot$ polytrope of index $n = 3/2$. For reference, the tidal radius r_t for this polytrope is 6.96×10^{12} cm.

We are now ready to combine the differential encounter rate θ_0 with the stripped mass fraction function $S(b)$ in order to determine the differential stripping rate $\zeta(b)$

$$\zeta(b) = m_\star \, \theta_0 \, S(b) \ , \tag{4.16}$$

where $m_\star$ is the mass of the star. For the purpose of this calculation, we will be using $m_\star = 1$ $M_\odot$ in order to directly compare to the results of Duncan & Shapiro (1983). The differential stripping rate $\zeta(b)$ gives the mass per unit time stripped from stars with impact parameters between b and $b + db$. The total stripping rate for the cluster F is given by integrating $\zeta(b)$ over b. In practice we will choose the upper limit of $b = 1.5 \times 10^{13}$ cm as the maximum impact parameter, as our SPH results show this is where mass stripping stops. The lower limit for b requires more careful consideration. If b is less than the Schwarzschild radius of the black hole, then the star will simply be swallowed by the black hole. Therefore, the

Schwarzschild radius sets an absolute lower limit. There is another consideration, however. Early work on the tidal disruption of stars by Carter & Luminet (1982) brought up the possibility that the star will be so strongly deformed by the tidal forces of the black hole that enhanced nuclear burning in the star could cause an explosion. The energy of the explosion might allow most of the material from the star to escape from the black hole. Although our SPH calculations in Chapter 3 did not directly address this prediction of Carter & Luminet, our work supports their finding that the central density of the star increases significantly for close encounters. However, for a solar mass star and a 10^6 $M_\odot$ black hole, the difference between the Schwarzschild radius and the impact parameter where the compression of the star becomes significant is only of order a factor of 2. These close encounters are so rare that changing the lower integration limit to take into account the effect predicted by Carter & Luminet will hardly affect the total stripping rate for the cluster. Therefore, we will use the Schwarzschild radius as the lower integration limit.

We are now ready to consider an example using a galactic nucleus with typical parameters. We will choose $\Psi(0) = 8\sigma^2$, $n_0 = 10^6$ stars/pc^3, $\sigma = 200$ km/s, $m_\star = 1$ $M_\odot$, and $M_{bh} = 10^6$ $M_\odot$. The value of $\Psi(0)$ is chosen to be the same as that used by Duncan & Shapiro (1983) in their study of the evolution of a massive black hole at the center of a King cluster. The cluster will have a core radius of $R_c = 2.6$ pc. The cumulative mass function for the stellar cluster will be called $M(r)$ and is plotted in Figure 4.2. The stellar mass density $\rho(r)$ is shown in Figure 4.3. Using equation 4.14, we find that the differential encounter rate has a value of

$$\boxed{\theta_0 = 8.4 \times 10^{-25} \text{ stars/sec/cm}} \,. \tag{4.17}$$

To make this number more tractable, consider that the number of stars passing per

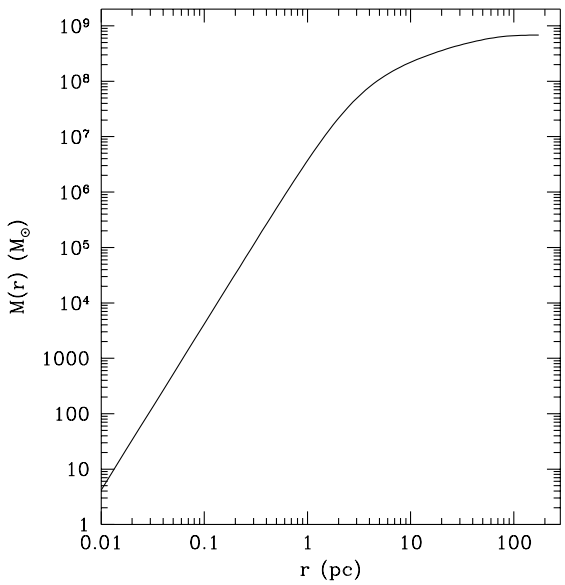

Fig. 4.2.— Total mass inside of a given radius r for the stellar cluster model presented in the text.

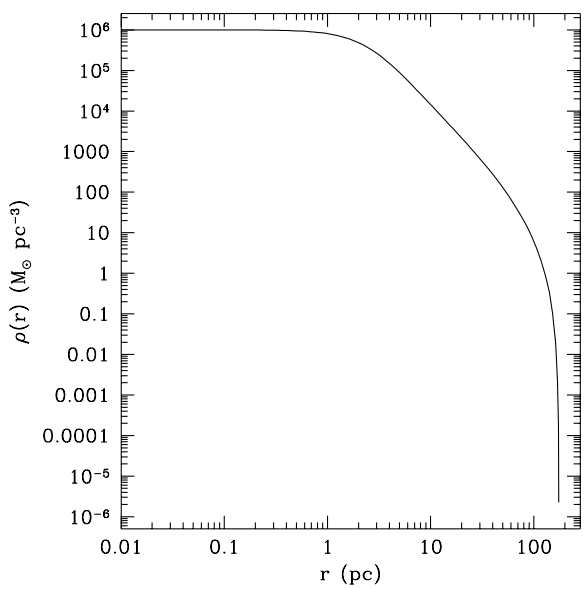

Fig. 4.3.— Density profile $\rho(r)$ for the stellar cluster model presented in the text.

second within the Roche radius r_t of the black hole is $r_t\theta_0$. For a 1 $M_\odot$ star with $r_t = 100R_\odot$, this translates into one disruptive encounter with the black hole every 5400 years. By combining this value of θ_0 with the SPH derived stripped mass fraction function $S(b)$, we find the differential stripping rate $\zeta(b)$, given in Figure 4.4. The cumulative stripping rate, shown in Figure 4.5, is given by integrating $\zeta(b)$, and represents the rate at which material is stripped from stars on orbits with an impact parameter less than or equal to a given value of b.

It was mentioned above that deep encounters may possibly lead to the explosion of the star, causing all of the stellar material to escape from the black hole. This is only important for stars with an impact parameter of $b \sim 5 \times 10^{11}$ cm or less. As can be seen in Figure 4.5, the contribution to the total stripping rate by stars on these orbits is less than 5%. Therefore, our decision to simply use the Schwarzschild radius as our inner boundary has only a small effect on the total stripping rate.

The cumulative stripping rate levels off around an impact parameter of $b = 10^{13}$ cm because beyond that distance a star does not lose mass, as shown by the plot of $S(b)$ in Figure 4.1. The total rate at which mass is stripped from stars by the black hole is

$$\boxed{F = 1.1 \times 10^{-4}\ M_\odot\ yr^{-1}}\ . \tag{4.18}$$

We will now compare our result to that of previous work by Duncan & Shapiro (1983), who used the hard–sphere assumption. They considered a model using an isothermal sphere for the star cluster. All stars were assumed to have a mass of 1 $M_\odot$, as in our calculation above. In addition, they assumed that the loss cone was full at all energies. The expression they derived for the total stripping rate is

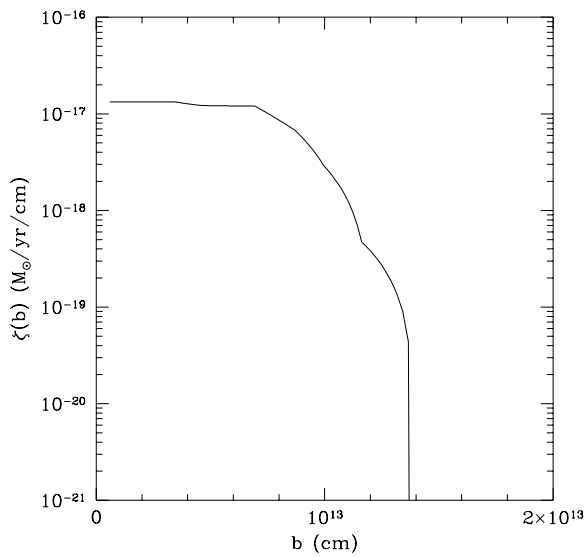

Fig. 4.4.— Differential mass stripping rate $\zeta(b)$.

given by

$$F_{full} = 0.31\ v_{350}^5\ M_8^{4/3}\ N_8^{-2}\ \mathrm{M}_\odot\ \mathrm{yr}^{-1}\ . \tag{4.19}$$

Here, v_{350} is the one–dimensional velocity dispersion σ expressed in units of 350 km/sec, M_8 is the mass of the black hole in units of 10^8 $\mathrm{M}_\odot$, and $N_8 = 2.19 n_0 R_c^3/10^8$.

For the present calculation $v_{350} = 0.57$, $M_8 = 0.01$, and $N_8 = 0.38$. These give a total stripping rate of $F_{full} = 2.8 \times 10^{-4}$ $\mathrm{M}_\odot$ yr^{-1}, somewhat larger than our result of 1.1×10^{-4} $\mathrm{M}_\odot$ yr^{-1}. To make our calculation closer to that of Duncan & Shapiro, we can take our stellar cluster model and use the hard–sphere assumption instead of our SPH derived $S(b)$. Doing so, we find a total stripping rate of 1.8×10^{-4} $\mathrm{M}_\odot$ yr^{-1}. Our estimate is still lower than that of Duncan & Shapiro, most likely because they assumed that the loss cone was full at all energies. In our calculation, we have restricted our sum to only those energies where the loss cone is full. If we remove this restriction and integrate over all energies, we find a total stripping rate of 2.4×10^{-4} $\mathrm{M}_\odot$ yr^{-1}. The remaining discrepancy can be explained

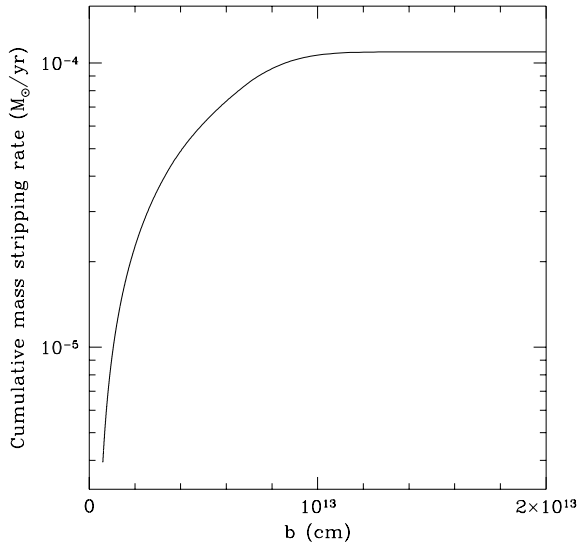

Fig. 4.5.— Cumulative mass stripping rate. Note that the majority of stripped mass comes from stars which pass inside of the Roche radius $r_t = 6.96 \times 10^{12}$ cm.

by our use of a King Model, which is of finite extent, and their use of an isothermal sphere, which extends to infinity.

The surprising conclusion which can be made from this example is that using our hydrodynamic results reduces the rate at which material is stripped by a factor of two, compared to estimates that use the hard–sphere assumption. This result can be easily understood if one considers the stripped mass fraction function $S(b)$ in Figure 4.1. The tidal radius for the polytrope used in the SPH calculation was $r_t = 6.96 \times 10^{12}$ cm. For encounters with an impact parameter of r_t or less, Figure 4.1 shows that the star loses one–half of its material to the black hole, and, for larger impact parameters, the amount of material lost drops to zero rapidly. The hard–sphere assumption states that the entire star is accreted for impact parameters less than r_t, and that no material is accreted for larger impact parameters. Therefore, the hard–sphere assumption is essentially correct if one modifies it to state that one–half of the star is accreted for impact parameters of

r_t or less. This conclusion is a result of the fact that the amount of mass stripped from the star (in this case an $n = 3/2$ polytrope) is a sensitive function of the impact parameter b for b near r_t. Although we have only considered one set of values for a galactic nucleus here, this finding should be universal for any stellar cluster since it does not depend on the cluster characteristics, just the details of the hydrodynamics of the disruption process.

4.2 Overall Role of Tidally–Disrupted Stars as a Fuel Source

We now have an estimate of the rate at which a black hole can be fed by the tidal disruption of stars. It is interesting to compare this rate to that from other sources of gas for the black hole. The two main possible other sources of gas which have been considered in the literature are stellar collisions and stellar winds. Duncan & Shapiro (1983) included stellar collisions in their Fokker–Planck simulations of the growth of a black hole in a galactic nucleus. The following expression was given for the rate at which material is freed through stellar collisions in an isothermal sphere of solar mass stars

$$F_{coll} = 2.4 \times 10^{-3} \, \frac{v_{350}^5 \, (v_{350}^2 + 0.77)}{N_8} \, \mathrm{M}_\odot \, \mathrm{yr}^{-1} \ , \tag{4.20}$$

where the definition of the quantities are the same as for equation (4.19). Using the values from our example in the previous section gives $F_{coll} = 4.2 \times 10^{-4}$ $\mathrm{M}_\odot$ yr^{-1}, about a factor of two greater than the fueling rate due to the tidal disruption of stars given by equation (4.19). This estimate ignores the presence of a massive black hole, which will cause the stellar velocity dispersion and density to increase towards the center of the cluster. The net effect will be to increase the collisional rate above that predicted by equation (4.20). As the mass of the black hole

increases, so does the enhancement to the collision rate. However, for a 10^6 $M_\odot$ black hole, this effect is not strong, and the factor–of–two difference between the tidal disruption and stellar collision rates should not require much modification.

Another series of Fokker–Planck calculations including stellar collisions have been performed by Murphy *et al.* (1991). These calculations also included mass loss due to stellar evolution and used a multimass Fokker–Planck code versus the single mass Fokker–Planck code employed by Duncan & Shapiro. For initial central stellar densities of a few times 10^7 $M_\odot$ pc^{-3}, they found that stellar collisions are the dominant source of material. In these clusters, the present day black hole mass was of order 10^9 $M_\odot$. For lower black hole masses and stellar densities, they found that stellar evolution was the dominant source of fuel. In one of their models, they chose $\rho_0 = 7 \times 10^5$ $M_\odot$ pc^{-3}, which led to a present–day black hole mass of 3.5×10^6 $M_\odot$ pc^{-3}. These values are close to the parameters we used in the previous section to calculate the fueling rate from the tidal disruption of stars. For this simulation, Murphy *et al.* found that stellar evolution produced material at a rate about a factor of ten greater than the tidal disruption of stars. In addition, material from stellar collisions was produced at about one–tenth the rate due to the tidal disruption of stars. This is in stark contrast to the rate given by equation (4.20) from the work of Duncan & Shapiro, which predicted that stellar collisions would provide material at about twice the rate as the tidal disruption of stars.

A major uncertainty in both the work of Duncan & Shapiro and Murphy *et al.* are the stellar collisional cross sections. Much like the hard–sphere assumption these works use to treat the tidal disruption of stars, assumptions had to be made concerning the cross section for two stars to collide. Hydrodynamic simulations of the collision of two stars now exist (e.g., Benz & Hills 1987), and

new Fokker–Planck simulations are needed to properly model the rate at which stellar collisions provide material. Another consideration is that the liberation of material by stellar evolution and stellar collisions occurs throughout the cluster. The migration of this gas down to the black hole is not a given, and the predicted fueling rates from these two sources must be viewed as upper limits. For example, mass loss from a star due to a stellar wind may send material in all directions. Only a fraction of this material will actually move on orbits which lead to being accreted by the black hole. On the other hand, the tidal disruption of a star deposits all of the liberated material within 100 Schwarzschild radii or less, meaning it is almost certain that all of this material will become part of an accretion disk. Again, more detailed calculations are required to fully understand the role of each fuel source in the feeding of the central black hole.

Finally, a major focus of this work is to consider the utility of the tidal disruption of stars in order to detect quiescent black holes in the nuclei of galaxies. Even if the tidal disruption of stars does not provide as large a time–averaged fueling rate as collisions or stellar evolution, when a star does disrupt, it provides material at a rate of order 1 $M_\odot$ yr^{-1} to the central black hole for a period of order one year. In contrast, stellar evolution provides material at the fairly steady rate of 10^{-4}–10^{-5} $M_\odot$ yr^{-1} for the case considered above from Murphy *et al.* Stellar collisions should provide material in bursts somewhat like the tidal disruption of stars, but it is unclear at what rate the debris from a stellar collision will be accreted by the black hole. It would seem that this would depend strongly upon the magnitudes and orientations of the velocities of the two stars colliding. Given these considerations, although it appears that tidal disruptions are not the main source of fuel by which a black hole grows to its present day mass, these events are highly suited for our purpose of detecting black holes in dead AGN.

4.3 Observational Consequences of a Tidal Disruption Event

Using our SPH simulations, we have now determined how much mass is stripped from a star which passes a black hole with a given impact parameter. Unfortunately, the disruption event is unlikely to be observed by astronomers since it takes place on the time scale of hours. Furthermore, the debris of the star cools so rapidly as it expands that it would be nearly impossible to detect such an event in the dense star field present at the center of a galaxy. It appears that the only practical way to detect a disruption event in a galactic nucleus is to wait for the stripped material to be accreted by the black hole (Rees 1988).

It is currently impossible to follow computationally the debris of the disruption event all the way to the point at which it is accreted by the black hole. Several authors, however, have speculated on what we should expect to happen (Rees 1988; Evans & Kochanek 1989; Cannizzo *et al.* 1990; Syer & Clark 1992; Kochanek 1993; Rees 1994). We will now summarize the main findings of these works. The material stripped from the star initially follows a distribution of Keplerian orbits about the black hole, as the material has cooled to the point that hydrodynamic forces are not significant and the gravitational field of the black hole dominates. The fraction of the debris bound to the black hole will follow highly elliptical orbits, with the most tightly bound material having an orbital period of (Rees 1988)

$$P_{min} \simeq 0.03 M_6^{1/2} \text{ yr} , \tag{4.21}$$

where M_6 is the mass of the black hole in units of 10^6 $\mathrm{M}_\odot$. Rees (1988) has predicted that the rate at which mass returns to pericenter as a function of time is given by

$$\dot{M} \simeq 25\, M_6^{-1/2} (t/P_{min})^{-5/3} \text{ M}_\odot \text{ yr}^{-1} . \tag{4.22}$$

Earlier SPH calculations by Evans & Kochanek (1989) and Laguna *et al.* (1993), as well as our own SPH calculations (for example, see Figure 3.4), have confirmed this expression with only minor modifications. Due to the wide range of orbital periods present, the debris will stretch out into a long, thin streamer of gas . At this stage, the debris would not strongly radiate, as it consists of very cold gas.

Several factors could cause the gas to become visible. Rees (1988) mentions that the closest approach of the debris upon return is approximately the same as the impact parameter of the star from which the debris originated. For a 10^6 $M_\odot$ black hole and a solar–type star passing at a distance of r_t, this corresponds to a distance of approximately 20 Schwarzschild radii. Relativistic orbital precession is non–negligible at this distance, so, after a few orbits, the most tightly bound debris will collide with material on longer period orbits (Rees 1988). The resulting shock would raise the temperature of the gas to a temperature of 10^5 K or greater. The debris is then thought to form an accretion disk, which could possibly be elliptical (Syer & Clark 1992). It is believed that the material will be accreted by the black hole at the rate given by equation (4.22), as long as this rate is less than (Rees 1988)

$$\dot{M}_{crit} = 0.02\, \epsilon_{0.1}^{-1}\, M_6 \text{ M}_\odot \text{ yr}^{-1} \ , \tag{4.23}$$

where $\epsilon_{0.1}$ is the efficiency of the disk at radiating the rest mass of infalling debris, in units of 10%. This limit corresponds to the disk luminosity being equal to the Eddington luminosity L_E

$$L_E = 1.1 \times 10^{44}\, M_6 \text{ ergs s}^{-1} \ . \tag{4.24}$$

If $L > L_E$, then material will be falling in faster than the black hole can swallow it, raising the possibility that a small fraction of the debris will be accreted with sufficient energy to eject the remaining debris (Rees 1988). An alternative

possibility is that the radiative efficiency ϵ of the disk will drop so that all of the debris can be accreted at a luminosity close to L_E. The difference is that in the first possibility, there would be a brief flare followed by no emission, while in the second possibility, the disk would radiate at a luminosity near the Eddington luminosity until the infall rate dropped sufficiently for the black hole to accept the debris with normal radiative efficiency. The luminosity would then decline following equation (4.22). Only a detailed calculation will be able to resolve between these two possibilities. Another complication arises if the black hole has a Kerr metric (Rees 1988). In that case, if the orbital axis of the debris is not aligned with the black hole's spin axis, the Lense–Thirring effect will cause the orbital axis of the debris to precess. In that case, the time scale for the stream to intersect itself could be considerable lengthened, and clearly this could affect the formation of an accretion disk. However, like previous authors, we will proceed assuming that we can ignore this complication, as a detailed calculation will be necessary to do otherwise.

In this work, we are primarily interested in black holes with a mass of order 10^6 $M_\odot$. Assuming a radiative efficiency ϵ with the canonical value of 0.1, the accretion rate corresponding to L_E is 0.02 $M_\odot$ yr^{-1}. Our SPH calculations of the tidal disruption of an $n = 3/2$ polytrope show that the mass return rate exceeds this limit for about one year, independent of the impact parameter of the star which was disrupted. We also find that the peak rate at which mass returns is also fairly independent of the impact parameter. If we now assume that all of the material will be accreted (the second possibility mentioned in the previous paragraph), the signature of a tidally–disrupted star will be a flare of nearly constant luminosity L_E for a period of approximately one year. Afterwards, the accretion rate will be less than the critical value determined by the Eddington luminosity. If one assumes that ϵ remains constant, then the luminosity will have the same temporal behavior

as the mass accretion rate given by equation (4.22) until the mass accretion rate becomes so low that ϵ starts to decrease. The possibility of detecting a massive black hole in this manner was first recognized by Rees (1988).

Very little is currently understood concerning the energy spectrum of the flare, as it depends upon the details of the accretion flow near the black hole. Some general comments are possible, however. When the stream of material first intersects itself, the resulting shock could heat material to $\sim 10^7$ K (Rees 1988). This is because the two parts of the stream which intersect could collide with velocities which are relativistic. Later, after the material has formed an accretion disk, the effective black–body temperature of the radiation will be $\sim 10^5$ K for a 10^6 $M_\odot$ black hole. Therefore, the energy spectrum should be dominated by extreme ultraviolet and soft X–ray photons.

It should be possible to detect X–ray flares from tidally–disrupted stars using a large survey like the *ROSAT All Sky Survey* (RASS) (Sembay & West 1993). Sembay & West have estimated that if most bright galaxies ($M_B < -20$) contain a massive black hole, at least several hundred if not several thousand flares could have been detected by the RASS. Another way to look at this estimate is as follows: because the time scale for the disruption of a star in a galactic nucleus is of order 10^3–10^4 years and the peak of the flare lasts of order 1 year, one would expect at least 1 out of every 10^4 galaxies to be in the flare state. Sembay & West assumed that one–half of the star was accreted by the black hole if the star passed within r_t. Our SPH results confirm this assumption to be reasonable. In addition, Sembay & West assumed that the debris would be accreted at near the Eddington luminosity for a period equal to the length of the RASS, six months. This assumption is uncertain until detailed calculations are available concerning the accretion of the

stripped debris. It would seem that this assumption would give an upper limit on the number of detectable events, as the truth might be that the debris accretes at a super–Eddington rate for only a short period, during which the remaining debris is blown away instead of accreted. In either case, in order to detect any flares, it will be necessary to compare the RASS observations to observations from another epoch, such as the *Einstein* IPC database. Confirmation of the predicted number of flare events would be strong evidence that most normal galaxies go through an AGN phase during their lifetime. Likewise, the failure to detect many events would probably indicate that AGN activity is the exception, not the rule, in the life of a galaxy.

4.4 Current Observational Evidence for Tidally–Disrupted Stars

4.4.1 The X–ray Outburst of IC 3599

The most likely method of detecting the tidal disruption of a star is from the associated X–ray flare, which lasts of order one year (Rees 1994). Such an event may have already been observed during *ROSAT* observations of the Seyfert galaxy IC 3599 (Grupe *et al.* 1995). They measured 4.9 counts per second in a December 1990 observation from the RASS. Following pointed observations with *ROSAT* gave 0.064 counts per second in December 1991, 0.043 counts per second in June 1992, and 0.023 counts per second in June 1993. This corresponds to a decrease in luminosity by over a factor of 100 in a few years. Grupe *et al.* claim that it is unlikely that this variation in luminosity is due to a temporary absorbing screen. The observations seem instead to suggest that the feeding rate of the black hole made an abrupt change.

Grupe *et al.* are able to set limits on the mass of the central black hole using the following procedure. If one assumes that the peak X–ray luminosity observed from IC 3599 is less than or equal to the Eddington luminosity, the mass M_{bh} of the central black hole must be

$$M_{bh} > 0.4 \times 10^6 \ \mathrm{M}_\odot \ . \tag{4.25}$$

One can also set an upper limit on the mass of the black hole using the ~ 500 km/s line widths of [FeX]λ6375 and [FeVII]$\lambda\lambda$5721, 6086. If one assumes that the width of these lines is larger than the Keplerian velocity at a distance of R, the mass of the black hole must be

$$M_{bh} < 33\,(R/1 \ \mathrm{pc}) \times 10^6 \ \mathrm{M}_\odot \ . \tag{4.26}$$

This limit should be met with caution, as the exact choice of R is not strongly constrained. Note that the range of masses proposed by Grupe *et al.* is centered near a mass of 10^6 $\mathrm{M}_\odot$. Finally, it can be shown (e.g., Blandford & Rees 1992) that a black hole mass near 10^6–10^7 $\mathrm{M}_\odot$ is consistent with the observed thermal spectrum having a temperature of $kT \sim 60$–100 eV. Consider that the majority of the luminosity from the disk comes from the innermost region, say from $r < 10R_g$ (Shakura & Sunyaev 1973), where R_g is the Schwarzschild radius given by

$$R_g = \frac{2GM_{bh}}{c^2} \tag{4.27}$$

$$= 3 \left(\frac{M_{bh}}{10^6 \ \mathrm{M}_\odot} \right) \times 10^{11} \ \mathrm{cm} \ . \tag{4.28}$$

For the sake of this calculation, we will assume that the disk can be approximated as a spherical black body with a radius of $R_{bb} = 10R_g$. The luminosity of this black body will be

$$L_{bb} = 4\pi \, \sigma \, R_{bb}^2 \, T_{bb}^4 \ , \tag{4.29}$$

where T_{bb} is the temperature of the black body. Substituting a value of $10R_g$ for R_{bb}, and using equation (4.28) to eliminate R_g, we find that

$$L_{bb} = 6.4 \times 10^{19}\, M_6\, T_{bb}^4 \text{ ergs s}^{-1} \ . \tag{4.30}$$

If we now divide both sides by the Eddington luminosity L_E, given by equation 4.24, and solve for T_{bb}, we find that the effective temperature of the disk is given by

$$\begin{aligned} T_{bb} &= 1.1 \times 10^6\, M_6^{-1/4} \left(\frac{L_{bb}}{L_E}\right)^{1/4} \text{K} \\ &\simeq 100\, M_6^{-1/4} \left(\frac{L_{bb}}{L_E}\right)^{1/4} \text{eV} \ . \end{aligned} \tag{4.31}$$

Therefore, if we assume that the luminosity of the flare is less than L_E, we require that the mass of the black hole to be of order 10^7 $M_\odot$ or less to be consistent with the observed thermal spectrum temperature of 60–100 eV.

As mentioned above, Grupe *et al.* proposed that the X–ray luminosity varied in response to a change in the accretion rate. One explanation offered for why the accretion rate varied over this period was an instability in the accretion disk. Although this scenario appears to work if one tweaks the disk parameters, we would like to explore the second explanation offered by Grupe *et al.* – the accretion of material from a tidally–disrupted star. Let us now see if the temporal behavior of the outburst is consistent with this hypothesis. As discussed in the previous section, if the rate at which the tidally–stripped material returns to the black hole exceeds the rate allowed by the Eddington luminosity, one possibility is that the disk will adjust itself to allow the material to be accreted with an efficiency so that its luminosity is approximately L_E. The luminosity of the disk would stay near L_E until the rate at which material returns to the black hole drops below the Eddington limit. Following Rees (1988), we seek to find the duration P_{edd} of this constant portion of the light curve. The temporal behavior of the accretion

rate is given by equation (4.22). We simply need to find how long the rate given by equation (4.22) is greater than the Eddington rate given by equation (4.23). Performing this calculation gives

$$P_{edd} \simeq 2.16\, \epsilon_{0.1}^{0.6}\, M_6^{-0.4} \text{ yr} . \tag{4.32}$$

The reader will now find it instructive to consult Figure 4.6 during the following discussion. This figure plots $\dot{M}$ and L versus time. The star is first disrupted at $t = 0$, and then the first material begins to return to the black hole at the time $t \simeq P_{min}$, where P_{min} is given by equation (4.21). From this time on we will assume that the tidally–stripped material is accreted by the black hole at the rate it returns from its elliptical orbits. This means the accretion rate of the black hole will follow equation (4.22). For a black hole mass of 10^8 $M_\odot$ or less, there will be a period where the accretion rate exceeds the Eddington rate. In that case, there will be a period of length P_{edd} over which the light curve is constant, as shown in in Figure 4.6. We have assumed that the disk is able to adjust itself so $\epsilon \dot{M} c^2$ is less than or equal to L_E, as discussed in the previous section.

Let us now assume that the December 1990 observation corresponds to the end of period of constant luminosity, i.e., $t = P_{min} + P_{edd}$. From this time onwards, we assume that $L \propto \dot{M}$, since the accretion rate will now be less than the Eddington rate. The next observation occurs in December 1991 and is a factor of 76.5 lower than the December 1990 measurement. The luminosity after December 1991 does not change significantly compared to this initial drop. Since IC 3599 is a Seyfert galaxy, there may be steady X–ray emission, and we should not expect the X–ray luminosity to drop to zero when all of the tidally–stripped debris has been accreted. Let us therefore concentrate on the initial drop in X–ray luminosity between December 1990 and December 1991. Because $L \propto \dot{M}$, and $\dot{M}$ follows equation

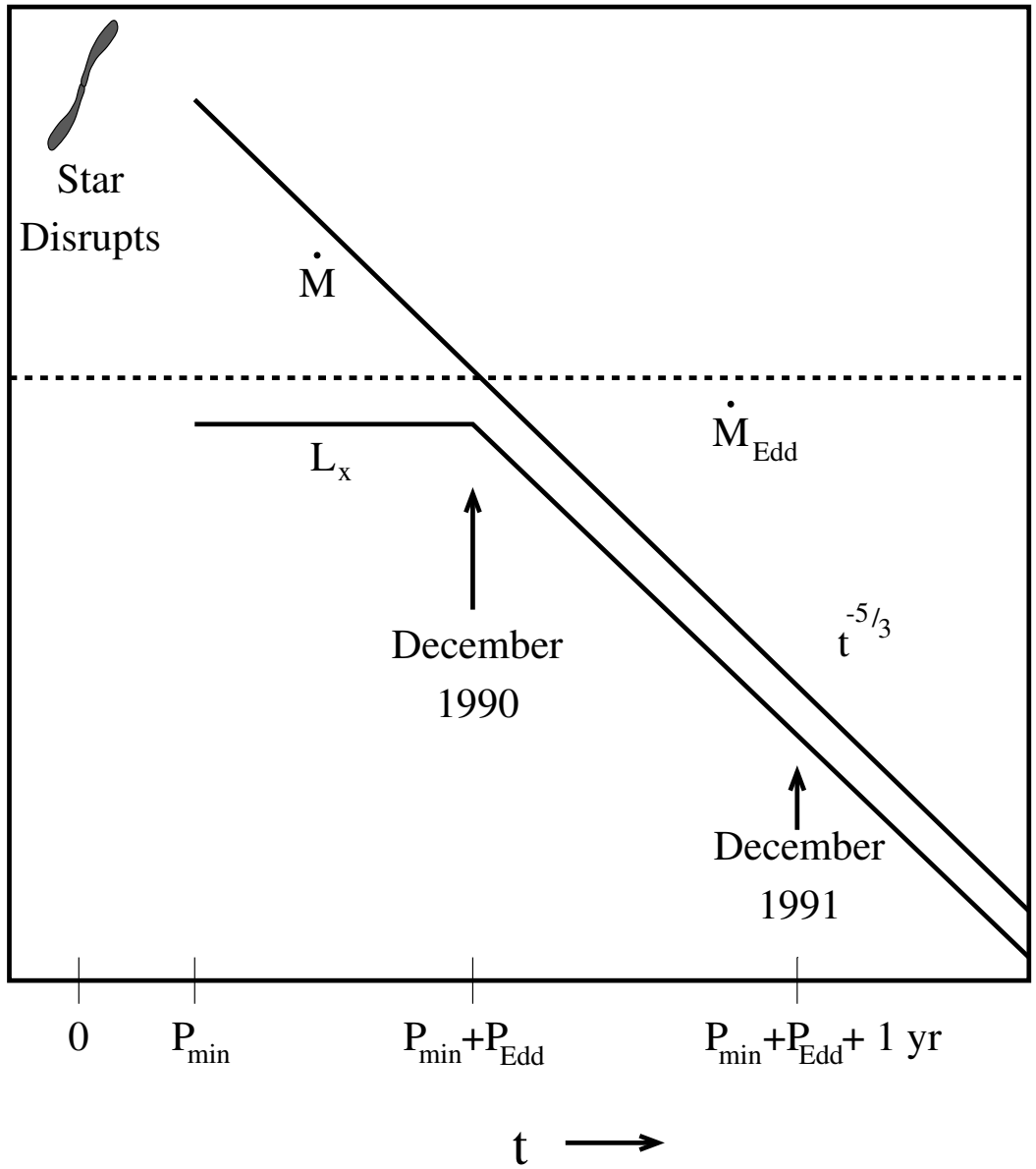

Fig. 4.6.— Proposed scenario for the IC 3599 outburst. At $t = 0$ a star is disrupted by the massive black hole. The material stripped from the star begins accreting around $t \simeq P_{min}$. At this time, the accretion rate $\dot{M}$ is greater than that allowed by the Eddington rate $\dot{M}_{Edd}$. The accretion disk adjusts itself so that it accepts all the incoming material with a lower efficiency, and the luminosity L_x will be constant and have a value near L_{Edd}. When $\dot{M} < \dot{M}_{Edd}$, the luminosity is assumed to be proportional to $\dot{M}$, which will follow equation (4.22) at all times after $t = P_{min}$. It will be assumed that the December 1990 *ROSAT* observation occurred at the end of the constant portion of the light curve. For full details, consult the discussion in the main text.

(4.22), we can write the following relationship between the luminosity on December 1990 and December 1991

$$\frac{L(1990)}{L(1991)} = 76.5 = \left\{ \frac{P_{min} + P_{edd} + 1 \text{ yr}}{P_{min} + P_{edd}} \right\}^{5/3} . \tag{4.33}$$

This can be simplified to the relationship

$$P_{min} + P_{edd} = 0.08 \text{ yr} . \tag{4.34}$$

It turns out there is no physical solution for the mass of the black hole, when equations (4.21) and (4.32) are substituted for P_{min} and P_{edd}. What this means is that if this X–ray burst is due to the accretion of tidally–stripped debris, then the accretion mechanism does not work as we assumed. It is not possible to have such a strong decrease in the X–ray luminosity in such a short time. These conclusions are based on the assumption that all material is still accreted when the accretion rate is super–Eddington. Another possibility mentioned in the previous section is that some material is accreted at the super–Eddington rate, but radiates sufficient energy to liberate the remaining material from the black hole. In this case, one would expect a brief period of strong X–ray emission followed by an abrupt drop. At this time, it is impossible to choose whether either scenario is correct. It will probably require sophisticated modeling of the accretion process in order to understand this problem fully.

In conclusion, the observations of IC 3599 are within the realm of what we might expect from the accretion of a tidally–disrupted star, but this statement only belies our lack of understanding of how the material is accreted once stripped from the star. Let's review some other possibilities forwarded by Grupe *et al.* It is unlikely that a change of a factor of 100 in luminosity is due to change in the optical depth to the X–ray source. Grupe *et al.* also discount the possibility that

this outburst is due to a single supernova, which would be too faint to explain the observed luminosity. The final option considered is a short–term increase in the accretion rate due to instabilities in the accretion disk. This appears to work if the proper parameters are chosen, but it is not clear that these parameter values are reasonable. Therefore, while it is conceivable that the X–ray flare observed from IC 3599 was due to the tidal disruption of a star, this is by no means the only plausible explanation.

4.4.2 Balmer Line Variability in NGC 1097

There is a class of AGN known as low–ionization nuclear emission–line regions, or LINERs (Heckman 1980). As their name suggests, narrow low–ionization emission lines (e.g., Hα, [OI]λ6300, and [O II]λ3727) are the dominant spectroscopic feature of these objects. There has been some debate to date about whether the emission lines are excited by shocks or photoionization. Recently, Eracleous *et al.* (1995a, hereafter ELB) have proposed a new photoionization model for LINERs which was motivated by the results of an ultraviolet (UV) snapshot survey of 26 LINERs using *HST* by Maoz *et al.* (1995). If photoionization is the excitation mechanism, it is expected that a compact nuclear UV source should be present in each object. Instead, only 5 of the 26 LINERs observed had such a nuclear region. One obvious interpretation is that 80% of the objects had material which obscures the central UV source. Another possibility is that the excitation mechanism is one that does not require a central UV source, such as shocks. However, ELB take a different stance on the *HST* observations in saying that they represent a population powered by a central UV source that is only active 20% of the time. They propose that, normally, the central black hole is starving for

material. When a star is tidally disrupted, the black hole becomes a UV source and photoionizes the surrounding medium. The black hole is expected to be a significant UV source for only several decades. Using a photoionization model, ELB find that when the UV flux from the black hole drops, the high–ionization lines such as [OIII]λ5007 are found to also drop as the atoms recombine. However, low–ionization lines are found to persist until the next expected tidal disruption of a star. In order for the duty cycle to be 20%, they require a black hole mass of order 10^7 $M_\odot$. Considering that one–third of all spiral galaxies are observed to be LINERs (Ho *et al.* 1995), if this model is correct, then we are witnessing the results of the tidal disruption of stars all around us.

To support their model, ELB point out the recent outburst of the LINER NGC 1097 (Storchi–Bergmann *et al.* 1993). In this outburst, the spectrum of NGC 1097 underwent a change from a LINER spectrum to that of a Seyfert 1 galaxy with the appearance of broad, double–peaked Balmer lines and a featureless continuum in the optical. Further observations revealed that the broad Hα profile varied with time. Eracleous *et al.* (1995b) have modeled this variation as the precession of an elliptical ring around a 10^6 $M_\odot$ black hole. The ring is believed to have formed from the debris of a tidally–disrupted star. If that is the case, then we are witnessing the start of the active cycle of this LINER. In a few decades, the featureless continuum will have faded, and, soon afterwards, the high–ionization lines will have disappeared.

The duty cycle hypothesis of ELB suggests a new way to search for tidal disruption events. Using NGC 1097 as an example of what such an event would look like, we expect the broad Balmer lines to persist for at least several years. Depending on the mass of the central black hole as well as the central star cluster

parameters, we expect a star to be disrupted every 10^2–10^4 years. If the duty cycle hypothesis is correct, an observing program that checked several hundred LINER galaxies every few years would catch many in an outburst stage like NGC 1097 exhibited. Since LINER galaxies include nearby, bright galaxies, this program would not require deep exposures of each object. It might even be possible to use a multi–object fiber spectrograph to sample large numbers of galaxies at once in a galaxy cluster.

4.5 Conclusions

There is now mounting evidence that massive black holes exist in the cores of some nearby galaxies. Dynamical evidence exists for the presence of a massive black hole not only in our own Galaxy, but in several nearby galaxies as well. Currently, the only reasonable explanation for the source of power of AGNs relies heavily upon the existence of a massive black hole in the central engine. What is of greater uncertainty is how common it is for a galaxy to form a central black hole. Studies of the evolution of the quasar luminosity function suggest either (a) that most galaxies went through a short AGN phase and should have a $\sim 10^7$ $M_\odot$ black hole, or (b) that only a few galaxies went through a long AGN phase and possess a 10^9–10^{10} $M_\odot$ black hole (Boyle *et al.*). Of course, as it is with most things, the truth is probably somewhere between these two extremes.

If we were able to detect the presence of a massive black hole in a galaxy not currently in the AGN phase, it would be possible to determine how many galaxies have a massive black hole. For nearby galaxies, it is possible to use dynamical evidence to detect the gravitational influence of a black hole on stars. Unfortunately, this technique is impractical for the large majority of galaxies due

to the high spatial resolution that would be required. However, it is still possible to detect the presence of a black hole by the destructive influence it would have on stars that stray too close. The disruption of a star would feed of order 1 $M_\odot$ of material into the previously dormant black hole, resulting in an X–ray outburst at near the Eddington luminosity L_E (given by equation 4.24) for a period of order one year. Looking for such outbursts in otherwise quiescent galaxy nuclei offers an effective, if not the only, way to detect massive black holes in the cores of these galaxies.

To estimate how often outbursts will occur in a given galaxy requires knowledge of the disruption process. Previous estimates have assumed that if a star passed closer than a threshold distance, it was disrupted and completely accreted (the hard–sphere assumption). Only recently has it become possible to numerically calculate the details of the disruption process. Using a series of SPH calculations, we have mapped out the dependence of the mass lost by a star as a function of its closest approach to the black hole. We find that if we use these SPH results instead of the hard–sphere assumption used in previous calculations, we have slightly more disruption events, but the total mass accreted is approximately half that which would be expected using the hard–sphere assumption. These conclusions come about for two reasons. One is because the SPH results show that a star will lose some material for a larger impact parameter than the threshold distance used for the hard–sphere assumption. This results in more disruption events. Secondly, the reason the SPH results yield half the total mass that the hard–sphere results do is because the star can only lose at most one–half of its mass to the black hole. The hard–sphere assumption says that all of the star is accreted. Since the distance at which the SPH simulations show that the star is completely disrupted is comparable to the threshold distance used in the hard–sphere calculations, the

result is one–half as much total accreted material in the SPH case.

These preliminary results indicated that past estimates of the disruption rate for a given galaxy are reasonable, since our results do not significantly change the number of disruption events expected. However, previous work concerning the growth of a massive black hole from a small seed black hole may need to be re–examined, as they have overestimated the total amount of mass that could be accreted by a factor of two. New simulations using a Fokker–Planck code which incorporate our SPH results to grow a massive black hole from a seed hole need to be done. Work by Murphy *et al.* (1991) indicates, however, that tidal disruptions are only important for the growth of smaller black holes ($\sim 10^6$ $M_\odot$). Larger black holes ($\sim 10^8$ $M_\odot$) depend on debris from stellar collisions for the majority of their mass. Given these considerations, the factor–of–two difference our results introduce seem to indicate that past studies captured the essential elements of the disruption process by using the hard–sphere assumption. However, using our SPH results, future studies will be able to include more accurately the tidal disruption process when modeling the evolution of a massive black hole in a galactic nucleus.

Chapter 5

CONCLUSIONS AND FUTURE WORK

The possibility exists that a large fraction of present day galaxies harbor a massive black hole. This is suggested by studies of the contribution to the X–ray background from Active Galactic Nuclei (AGN), as well as studies of the density and luminosity evolution of AGN. On a more local scale, evidence exists for the presence of a massive black hole in many nearby galaxies. Kinematic studies of gas and stars in the central parsecs of our own Galaxy suggest the presence of an $\sim 10^6$ $M_\odot$ black hole at its core. Photometric and kinematic studies for several nearby galaxies, such as M31 and M32, also suggest these galaxies possess a massive, central black hole. Unfortunately, it is not possible to detect a $\sim 10^6$ $M_\odot$ black hole by these methods except in only the nearest of galaxies. This is because the black hole influences a region of order 1 pc at the center of a galaxy, and at the distance of the Virgo cluster (20 Mpc), the area of influence subtends 0.01 arcseconds. A different signature that will allow the unambiguous identification of

galaxies harboring massive black holes is therefore needed.

If most galaxies have a massive black hole, it is expected that most are not in the AGN phase, in order to be consistent with the present day AGN luminosity function. Instead, for reasons which are not presently clear, the black hole is mostly starved for material and does not exhibit the traditional features of an AGN central engine. Occasionally, perhaps once every 10^3–10^4 years, a star will be disrupted by the central black hole. This event will dump of order 1 $M_\odot$ of material onto the black hole on a time scale of one year. Suddenly, the black hole will flare into activity in what was previously an unexceptional galactic nucleus. The flare is expected to be mostly observable in the extreme ultraviolet and soft X–rays. One all–sky survey in this energy range has been completed (*ROSAT All Sky Survey*). Eventually, another survey will be performed, and, by searching for transient events, evidence for the existence of massive black holes in most galaxies could be found.

An interpretation of the results of such an endeavor requires the modeling of a stellar cluster in the vicinity of a massive black hole. With such a model, it is possible to predict how often stars will come close enough to the black hole to be disrupted. Once a star has disrupted, it is desirable to know the observable consequences. This requires hydrodynamic simulations of the disruption of the star, as well as the fallback of the stripped debris to the black hole. In this work, we have considered the disruption of a star using a new Smoothed Particle Hydrodynamics (SPH) method based on spheroidal kernels (Chapter 2). We found that the traditional SPH method using spherical kernels proved to be inadequate for the extreme conditions present during deep plunges by a star into the gravitational field of the black hole. In addition, we found that the traditional way in which

SPH treats viscous heating leads to incorrect results. Our new method amends this problem by incorporating a viscous heating term designed to give more accurate results, and we found it to perform as expected. With the simulations presented in Chapter 3, we have derived cross sections for the stripping of mass from polytropes of index $n = 3/2$ and $n = 3$. The $n = 3/2$ polytrope has an internal structure resembling low mass, fully convective M dwarfs. These stars form the majority of the mass in stars in the solar neighborhood, and therefore, are likely to be the most common type of star to be disrupted. Stars of nearly solar mass or greater can be represented by a polytrope of index $n = 3$. We have computed encounters for polytropes of two indices in order to map out the behavior of all stellar types. As expected, the more centrally concentrated $n = 3$ model requires a deeper plunge before it is completely disrupted, as compared to the $n = 3/2$ model. An unanticipated result was that the time scale for the material stripped from the star to fallback to the black hole is fairly independent of the impact parameter of the star. This suggests that there may be a *unique temporal signature* of a flare resulting from the tidal disruption of a star. However, to confirm this, it will be necessary to hydrodynamically model the accretion of the debris onto the black hole. This problem not only involves the tricky subject of an accretion disk; it must also deal with how a stream of material interacts with itself to form a disk in the first place, a process which involves general relativistic effects. It is possible that super–Eddington accretion rates may exist, which will only further complicate the problem. Adding the possibility of a Kerr black hole, and the problem becomes even more obfuscated. These problems must be solved, however, in order to understand the signature of the accretion of material from a tidally disrupted star.

Once the details of the tidal disruption process are understood, it is necessary to combine this knowledge with a model of a stellar cluster around a black hole in

order to predict the rate at which flares will occur. A simple comparison of the rate at which gas is stripped from stars in the case of the hard–sphere assumption and our SPH results (Chapter 4) revealed that previous work predicted the correct rate of flares, but overestimated the rate at which mass is stripped by roughly a factor of two. This result can be partially understood by considering that the hard–sphere assumption states that the entire star is accreted by the black hole if it was disrupted, whereas hydrodynamic calculations show that at most one–half of the star can be accreted. The simple estimate in Chapter 4 can be further improved in several ways. The estimate presented here assumed that the cluster was a steady–state King model, and that the black hole mass did not change. In a real system, the black hole mass and the dynamics of the cluster would evolve together. Initially, a small seed black hole will form, and this object will grow as it accretes mass freed from stars through processes such as stellar collisions and mass loss prompted by stellar evolution and the tidal disruption of stars. One method to properly follow the evolution of the black hole and the stellar cluster requires the solution of the Fokker–Planck equation. Previous studies using the Fokker–Planck have used crude and inadequate treatment of tidal disruptions and stellar collisions. It would be a good time to revisit these issues making use of the large number of numerical simulations that have been carried out.

Sufficient hydrodynamical studies of the tidal interaction of a star with a black hole (e.g., this work, Diener *et al.* 1995; Khokhlov 1993), as well as the collision of two stars (e.g., Benz & Hills 1987), have been done to suggest what the next generation of Fokker–Planck codes should look like. In addition to a more accurate treatment of the tidal disruption of stars by using our results from Chapter 3, this new code should also incorporate numerical results on the tidal capture of stars by the black hole as well. These objects will possibly require several passes close

to the black hole before they lose material. If the time between interactions with the black hole is too long, however, the star may be scattered to a different orbit by interactions with other stars. This is why it would be interesting to include this process in a Fokker–Planck code. Likewise, stellar collisions should be treated using the results of numerical simulations. To date, stellar collisions have been treated using the analysis of Spitzer & Saslaw (1966). Compared to numerical calculations by Benz & Hills, for example, this earlier treatment neglects mass loss from collisions at less than the escape velocity of the colliding stars. Also, the treatment by Spitzer and Saslaw provides no information on the energy and momentum distribution of the debris, which can be used to predict how long it would take for the the material to be accreted by the black hole. Finally, a Fokker-Planck code should incorporate a multimass spectrum of stars. The only work so far to do this is Murphy *et al.* (1991). Not only is a multimass model required to include interesting physics such as mass segregation, but also one would like to consistently model tidal disruptions and stellar collisions using a realistic mass spectrum.

A goal for Fokker–Planck simulations of the growth of a black hole in a stellar cluster is to try to explain why the AGN phase in most galaxies appears to only last several times 10^7 years, yielding a central black hole mass of 10^6–10^7 $M_\odot$. With a Fokker–Planck simulation, it is possible to follow the luminosity of the AGN as a function of time, as one can calculate the rate at which mass is freed from stars by various processes. With a concrete theoretical understanding of the evolution of an AGN central engine, combined with observational limits set by X–ray all–sky surveys on the fraction of galaxies which show flares resulting from the tidal disruption of stars, it should be possible to make considerable progress towards understanding the most powerful objects in the universe.

REFERENCES

Benz, W., & Hills, J. G. 1987, ApJ, 323, 614.

Bicknell, G. V., & Gingold, R. A. 1983, ApJ, 273, 749.

Binney, J., & Tremaine, S. 1987, *Galactic Dynamics*, (Princeton:Princeton University Press), pp. 232–239.

Blandford, R. D., & Rees, M. J. 1992, *AIP Conference Proceedings 254, Testing the AGN Paradigm*, ed. S. S. Holt, S. G. Neff, & C. M. Urry (New York:AIP), p. 3.

Boyle, B. J., Fong, R., Shanks, T., & Peterson, B. A. 1987, MNRAS, 227, 717.

Cannizzo, J. K., Lee, H. M., & Goodman, J. 1990, ApJ, 351, 38.

Carter, B., & Luminet, J.–P. 1982, *Nature*, 296, 211.

Carter, B., & Luminet, J.–P. 1983, A&A, 121, 97.

Carter, B., & Luminet, J.–P. 1986, ApJ, 61, 219.

Cohn, H., & Kulsrun, R. M. 1978, ApJ, 226, 1087.

Diener, P., Kosovichev, A. G., Kotok, E. V., Novikov, I. D., & Pethick, C. J. 1995, MNRAS, 275, 498.

Duncan, M. J. & Shapiro, S. L. 1983, ApJ, 265, 565.

Eracleous, M., Livio, M., & Binette, L. 1995, ApJ, 445, 1 (1995a)(ELB).

Eracleous, M., Livio, M., Halpern, J. P., & Storchi–Bergmann, T. 1995, ApJ, 438, 610 (1995b).

Evans, C. R., & Kochanek, C. S. 1989, ApJ, 346, L13.

Fabian, A. C., Pringle, J. E., & Rees, M. J. 1975, MNRAS, 172, 15P.

Fehlberg, E. 1969, *NASA TR 315*.

Frank, J., & Rees, M. J. 1976, MNRAS, 176, 633.

Gingold, R. A., & Monaghan, J. J. 1977, MNRAS, 181, 375.

Grupe, D., Beuermann, K., Mannheim, K., Bade, N., Thomas, H.–C., de Martino, D., & Schwope, A. 1995, A&A, 299, 5.

Haller, J. W., Rieke, M. J., Rieke, G. H., Tamblyn, P., Close, L., & Melia, F. 1995, ApJ, to be published.

Heckman, T. M. 1980, A&A, 87, 152.

Hernquist, L., & Katz, N. 1989, ApJS, 70, 419.

Hills, J. G. 1975, Nature, 254, 295.

Ho, L. C., Filippenko, A. V., & Sargent, W. L. 1994, *IAU Symposium 159, Multi–Wavelength Continuum Emission of AGN*, ed T.J.–L. Courvoisier & A. Blecha (Dordrecht:Kluwer), p. 275.

Khokhlov, A., Novikov, I. D., & Pethick, C. J. 1993, ApJ, 418, 163.

King, I. R. 1966, AJ, 71, 64.

Kochanek, C. S. 1994, ApJ, 422, 508.

Kormendy, J. 1993, *AIP Conference Proceedings 254, Testing The AGN Paradigm*, ed. S. S. Holt, S. G. Neff, & C. M. Urry (New York:AIP), p. 23.

Lacy, J. H., Townes, C. H., & Hollenbach, D. J. 1982, ApJ, 262, 120.

Laguna, P., Miller, W. A., Zurek, W. H., & Davies, M. B. 1993, ApJ, 410, L83.

Lai, D., Rasio, F. A., & Shapiro, S. 1993, ApJ, 412, 593.

Lauer, T. R., Faber, S. M., Holtzman, J. A., Baum, W. A., Currie, D. G., Ewald, S. P., Groth, E. J., Hester, J. J., Kelsall, T., Kristian, J., Light, R. M., Lynds, C. R., O'Neil, E. J. J., Shaya, E. J., & Westphal, J. A. 1991, ApJ, 369, L41.

Lauer, T. R., Faber, S. M., Lynds, C. R., Baum, W. A.,Ewald, S. P., Groth, E. J., Hester, J. J., Holtzman, J. A., Kristian,J., Light, R. M., O'Neil, E. J. J., Schneider, D. P., Shaya, E. J.,& Westphal, J. A. 1992, AJ, 103, 703 (1992a).

Lauer, T. R., Faber, S. M., Currie, D. G., Ewald, S. P., Groth, E. J., Hester, J. J., Holtzman, J. A., Light, R. M., O'Neil, E. J. J., Shaya, E. J., & Westphal, J. A. 1992, AJ, 104, 552 (1992b).

Lauer, T. R., Faber, S. M., Groth, E. J., Shaya, E. J., Campbell, B., Code, A., Currie, D. G., Baum, W. A., Ewald, S. P., Hester, J. J., Holtzman, J. A., Kristian, J., Light, R. M., Lynds, C. R., O'Neil, E. J. J., Westphal, J. A. 1993, AJ, 106, 1436.

Lee, H. M., & Ostriker, J. P. 1986, ApJ, 310, 176.

Lightman, A., & Shapiro, S. 1977, ApJ, 211, 244.

Luminet, J.–P., & Marck, J. A. 1985, MNRAS, 212, 56.

Lucy, L. B. 1977, AJ, 82, 1013

Maoz, D., Filippenko, A. V., Ho, L. C., Rix, H.–W., Bahcal, J. N., Schneider, D. P., & Macchetto, F. D. 1995, ApJ, 440, 91.

Monaghan, J. J. 1989, J. Comp. Phys. 82, 1

Monaghan, J. J. 1992, ARA&A30, 543

Murphy, B. W., Cohn, H. N., & Durisen, R. H. 1991, ApJ, 370, 60.

Phinney, E. S. 1989, *IAU Symposium 136, The Galactic Center*, ed. M. Morris (Dordrecht:Kluwer), p. 543.

Press, W. H., & Teukolsky, S. A. 1977, ApJ, 213, 183.

Rana, N. C. 1987, A&A, 184, 104.

Rees, M. J. 1988, *Nature*, 333, 523.

Rees, M. J. 1990, *Science*, 240, 87.

Rees, M. J. 1994, *IAU Symposium 159, Multi–Wavelength Continuum Emission of AGN*, ed T.J.–L. Courvoisier & A. Blecha (Dordrecht:Kluwer), p. 239.

Sembay, S., & West, R. G. 1993, MNRAS, 262, 141.

Serabyn, E., & Lacy, J. H. 1985, ApJ, 293, 445.

Shakura, N. I., & Sunyaev, R. A. 1973, A&A, 24, 337.

Shapiro, S. L. & Marchant, A. B. 1978, ApJ, 225, 603.

Shapiro, S. L. 1985, *IAU Symposium 113, Dynamics of Star Clusters*, ed J. Goodman & P. Hut (Dordrecht:Reidel), p. 373.

Spitzer, L., & Saslaw, W. 1966, ApJ, 143, 400.

Storchi–Bergmann, T., Baldwin, J. A., & Wilson, A. S. 1993, ApJ, 410, L11.

Syer, D., & Clarke, C. J. 1992, MNRAS, 255, 92.

Young, P. J. 1980, ApJ, 242, 1232.